



저작자표시-비영리-변경금지 2.0 대한민국

이용자는 아래의 조건을 따르는 경우에 한하여 자유롭게

- 이 저작물을 복제, 배포, 전송, 전시, 공연 및 방송할 수 있습니다.

다음과 같은 조건을 따라야 합니다:



저작자표시. 귀하는 원저작자를 표시하여야 합니다.



비영리. 귀하는 이 저작물을 영리 목적으로 이용할 수 없습니다.



변경금지. 귀하는 이 저작물을 개작, 변형 또는 가공할 수 없습니다.

- 귀하는, 이 저작물의 재이용이나 배포의 경우, 이 저작물에 적용된 이용허락조건을 명확하게 나타내어야 합니다.
- 저작권자로부터 별도의 허가를 받으면 이러한 조건들은 적용되지 않습니다.

저작권법에 따른 이용자의 권리는 위의 내용에 의하여 영향을 받지 않습니다.

이것은 [이용허락규약\(Legal Code\)](#)을 이해하기 쉽게 요약한 것입니다.

[Disclaimer](#)

공학박사 학위논문

**A Study on Change in Textures of
Extruded Mg-Zn-Al Alloys with
Extrusion Temperatures and
Alloying Elements**

압출온도 및 합금원소에 따른 Mg-Zn-Al 합금
압출재의 집합조직 변화에 관한 연구

2017년 2월

서울대학교 대학원

재료공학부

최 정 우

A Study on Change in Textures of Extruded Mg-Zn-Al Alloys with Extrusion Temperatures and Alloying Elements

지도교수 신 광 선

이 논문을 공학박사 학위논문으로 제출함

2017년 1월

서울대학교 대학원

재료공학부

최 정 우

최정우의 박사 학위논문을 인준함

2017년 1월

위 원 장 한 홍 남 (인)

부위원장 신 광 선 (인)

위 원 김 낙 준 (인)

위 원 김 도 향 (인)

위 원 이 경 훈 (인)

Abstract

A Study on Change in Textures of Extruded Mg-Zn-Al Alloys with Extrusion Temperatures and Alloying Elements

Jung Woo Choi

School of Materials Science and Engineering

The Graduate School

Seoul National University

Recent years, to lower the fuel consumptions and CO₂ emissions of the vehicles, magnesium alloys have been widely used for the cast automotive parts such as steering wheel, seat frame and cylinder head cover because of their high specific strength and good castability. However, to increase the weight reduction effect significantly, Mg alloys should be applied for the large volume parts such as inner or outer body panels for doors or trunk usually made by steel or aluminum sheets. To be successfully applied for these parts, materials should have a good combination of strength and formability.

Generally, most of the commercial wrought Mg-Zn-Al alloys show the basal textures. The basal texture represents the specific texture whose basal poles are aligned nearly parallel to the normal direction of the extruded or rolled planes. Among many types of the basal textures, the one whose two peaks in the basal pole figure are split into the positive and negative extrusion directions or rolling directions from the normal direction is called the

double peak (type) basal texture. It is well-known that low ductility of the wrought Mg alloys at room temperature is originated from their strong basal textures because most of their deformation at room temperature is accommodated by the basal slip. Therefore, many researchers have focused on developing the methods to broaden or weaken the basal textures to increase the activity of the basal slip. Increasing the split angle between the two peaks in the double peak basal texture is one way to broaden the basal texture.

Many research groups have focused on developing the Mg alloys containing rare earth elements because of their dramatic texture weakening effect. Several researchers have already reported that the texture weakening effect of the RE elements might be originated from the change in stacking fault energy or solute drag effect activated when they were in solid solution state. However, most of the rare earth elements in the solid solution state transform into precipitates by reacting with Al or Zn which are used most widely as the effective solid solution strengthening elements. Therefore, it is hard to design a high strength Mg-RE alloy whose texture is still weak enough when large amount of Al or Zn is added to increase its strength. Consequently, to achieve the good combination of strength and formability, researches focused on the texture control of the high Zn or Al-containing Mg alloys are necessary.

In this study, effects of the extrusion temperature and alloying elements on the textures of the extruded Mg-Zn-Al alloys were investigated. And their mechanisms were systematically studied by the two-step PSC tests.

With increase in Zn and Al contents, spread of the basal poles toward the ED (ED spread) and tilt angle corresponding to the peak in the double peak basal texture (DP texture) increased with decrease in grain size. And with

increase in extrusion temperature, single peak basal texture (SP texture) was developed and ED spread decreased. In the ZA11 alloys, $\{10\text{-}10\}\langle 1\text{-}210\rangle$ texture strengthened with increase in temperature. However, in the ZA61 and ZA63 alloys, $\langle 0001\rangle//\text{ED}$ texture was developed at high temperature and strengthened with increase in temperature. And the intensity of $\langle 0001\rangle//\text{ED}$ texture increased with increase in Al content. With addition of Ca or Ce on pure Mg, intensity of the DP texture weakened and ED spread and tilt angle corresponding to the peak in the DP texture increased. And with addition of Ca on ZA alloys, DP texture with weak intensity was developed and $\{11\text{-}20\}\langle 1\text{-}100\rangle$ texture was developed. With increase in Ca content in Z6 or ZA61 alloys, intensity of the $\{11\text{-}20\}\langle 1\text{-}100\rangle$ texture increased instead of decrease in intensity of the DP texture.

In the two-step PSC (PSC at room temperature as a first step and PSC at high temperature as a second step), DP texture was developed with the partially DRXed fine microstructure developed by the NRX at low temperature. And SP texture was developed with the fully DRXed coarse microstructure by the NRX and grain growth at mid temperature. At high temperature, DP and $\{11\text{-}20\}\langle 1\text{-}100\rangle$ texture was developed with large grains occurred by the ordinary DRX. With increase in Zn content, spread of the basal poles toward the longitudinal direction (LD spread) and tilt angle corresponding to the peak in DP texture developed at low and high temperature increased. And with increase in Zn content, intensity of the $\{11\text{-}20\}\langle 1\text{-}100\rangle$ texture increased. In the one-step PSC at 0.4000/sec, $\langle 0001\rangle//\text{LD}$ texture occurred and strengthened with increase in temperature and it was maximized at 380°C in the ZA63 alloy. Intensity of the $\langle 0001\rangle//\text{LD}$ texture increased with decrease in solidus temperature of the ZA alloys. And in the two-step PSC

(ROT, PSC at room temperature as a first step and 90°-rotation of specimen on CD and PSC at high temperature as a second step), intensity of the <0001>//LD texture increased with decrease in solidus temperature of the ZA alloys.

These phenomena were explained in the view point of the grain size and solidus temperature based on the theories about the grain-size dependant compatibility deformation and thermal activation of the cross-slip.

Keywords: Magnesium alloy, Texture, Extrusion, Plane strain compression, Temperature, Zinc, Aluminum, Calcium

Student Number: 2005-23420

Contents

Chapter 1 Introduction	1
1.1 Research objectives.....	1
1.2 Theoretical deformation texture.....	4
1.3 Recrystallization texture	8
1.4 Experimental observation of $\langle c+a \rangle$ dislocation	22
1.5 Approach to activate non-basal slip.....	33
1.5.1 Decreasing CRSS of non-basal slip	35
1.5.2 Increasing CRSS of basal slip.....	41
1.5.3 Grain-size dependant compatibility deformation.....	48
1.6 Summary on texture development mechanisms.....	53
1.6.1 Mechanisms for double peak basal texture	53
1.6.2 Mechanisms for rare-earth texture	54
Chapter 2 Experimental procedures	56
2.1 Fabrication of extruded plate	56
2.1.1 Extrusion process	56
2.1.2 Alloy and extrusion condition.....	57
2.2 Plane strain compression test.....	62
2.2.1 Plane strain compression process.....	62
2.2.2 Alloy and plane strain compression condition.....	63
2.3 Characterization of microstructure and texture.....	68

2.3.1	Microstructure.....	68
2.3.2	Texture	68
Chapter 3	Results	72
3.1	Effects of Zn and Al on double peak basal textures.....	72
3.2	Effects of extrusion temperature on textures	80
3.3	Effects of Ca on textures	91
3.4	Summary	101
Chapter 4	Discussions	105
4.1	Two-step PSC of extruded plate.....	105
4.1.1	Two-step PSC (CA // TD)	107
4.1.2	Two-step PSC (CA // ED)	112
4.1.3	Texture development process.....	115
4.1.4	Effect of initial grain size on texture.....	125
4.2	Two-step PSC of cast specimen	130
4.2.1	Two-step PSC.....	132
4.2.2	Two-step PSC (ROT).....	142
4.2.3	Effect of Ca on texture	150
4.3	Summary	153
Chapter 5	Conclusions	163

Bibliography	167
초 록	175

List of Tables

Table 2.1	Extruded alloys (extrusion name) and their extrusion conditions....	58
-----------	---	----

List of Figures

Figure 1.1	Effect of texture on mechanical property; basal pole intensity distribution (from ND to ED or TD), tensile flow curve (TA // ED or TD) and activity.....	3
Figure 1.2	Theoretical deformation textures developed during PSC with different CRSS ratios (basal $\langle a \rangle$: prismatic $\langle a \rangle$: pyramidal II $\langle c+a \rangle$: tensile twin) (from random texture); (1) 1:9:9:9, (2) 9:9:9:1, (3) 9:1:9:9, (4) 9:9:1:9, (5) 1:2: x :1 and (6) 1:2: x :5.....	5
Figure 1.3	Theoretical deformation textures developed during PSC with different CRSS ratios (from single peak basal texture); (1) 9:1:9:9 and (2) 1:1: x :1.....	6
Figure 1.4	Evolutions of Relative activities for theoretical deformation textures during PSC.....	7
Figure 1.5	DRX mechanisms and map for pure Mg deformed at temperatures ranging from 293 to 773 K; (1) CDRX, (2) DDRX, (3) TDRX and (4) Map.....	12
Figure 1.6	Difference in textures between parent and DRXed grains of Mg-6Gd-1Zn-0.2Zr (wt.%) alloy rolled at 500°C.....	13
Figure 1.7	Difference in textures between parent and DRXed grains of extruded pure Mg and Mg-Y (0.23, 0.84, 2.71wt.%) alloy rods PSCed at various temperatures with 0.001/s.....	14
Figure 1.8	Difference in textures between parent and DRXed grains of cast AZ31 and Mg-1.3Gd alloys PSCed at 400°C with various strain rates to a true strain of 0.7.....	16
Figure 1.9	Change in textures of hot rolled Mg-1Li (wt.%) and AZ31 alloy	

	sheets during grain growth annealing at 400°C..	17
Figure 1.10	Change in texture (IPF of ED) of warm extruded AZ31 alloy rod during grain growth annealing at 400°C; (1) SRX texture change and (2) consumption process of parent grains by SRXed grains.. ...	18
Figure 1.11	Change in texture of warm rolled AZ31 alloy sheet during grain growth annealing at 400°C; (1) SRX texture change and (2) relationship between grain size and {0001}<11-20> texture at initial stage.....	19
Figure 1.12	SBNeD recrystallization texture of Mg-1Zn-0.5Ca (wt.%) alloy rolled at 400°C after annealing process at 400°C.....	20
Figure 1.13	SBNeD recrystallization textures of Mg-1Zn-1Ce-0.6Zr and Mg-1Zn-1Gd-0.6Zr (wt.%) alloys rolled at 400°C after annealing process at various temperatures for 1hour..	21
Figure 1.14	Observation of <c+a> dislocations in pure Mg single crystal compressed along c-axis at room temperature.....	24
Figure 1.15	Observation of <c+a> dislocations in pure Mg single crystal compressed along c-axis at various temperatures with 0.01/min.; temperature dependency of CRSS of pyramidal II <c+a> slip.....	25
Figure 1.16	Observation of <c+a> dislocations in Mg-7Li (at.%) single crystal tensioned along [11-20] direction at various temperatures with 0.0001/s; temperature dependency of yield stress...	26
Figure 1.17	Observation of <c+a> dislocations in AZ31 alloy tensioned at room temperature to 2%; (initial material) AZ31 sheet with fine recrystallized grains (9 μm) and double peak basal texture.....	27
Figure 1.18	Observation of <c+a> dislocations in Mg-4.5Al-1Zn (wt.%) alloy compressed along c-axis at room temperature to 2~4%; (initial	

	material) Mg-4.5Al-Zn sheet rolled at 420°C with fine recrystallized grains (10 μm) and sharp basal texture..	28
Figure 1.19	Observation of $\langle c+a \rangle$ dislocations in Mg-4.5Al-1Zn (wt.%) alloy rolled at 180°C to 2~3%; (initial material) Mg-4.5Al-Zn sheet rolled at 420°C with fine recrystallized grains (10 μm) and sharp basal texture.....	29
Figure 1.20	Observation of $\langle c+a \rangle$ dislocations in AZ31 alloy BP-ECAPed at 200°C; (1) split of basal peak, (2) simulation by activation of $\langle c+a \rangle$ slip and (3) existence of $\langle c+a \rangle$ dislocations.....	30
Figure 1.21	Observation of $\langle c+a \rangle$ dislocations in Mg-15Li (at.%) alloy compressed along c-axis at room temperature to 1~3%; (initial material) cast Mg-15Li compressed at R.T. to 20% and annealed at 475°C for 1h with sharp basal texture.....	31
Figure 1.22	Observation of $\langle c+a \rangle$ dislocations in Mg-3Y (wt.%) alloy cold-rolled to 3%; (initial material) Mg-3Y sheet rolled at 500°C to 50% and annealed at 500°C for 15min. with uniform recrystallized grains (35 μm).....	32
Figure 1.23	Approach to activate non-basal slip; (1) decreasing CRSS of non-basal slip, (2) increasing CRSS of basal slip, (3) increasing flow stress and (4) increasing additional internal stress.....	34
Figure 1.24	Theoretical effects of alloying element on SFE of pyramidal II $\langle c+a \rangle$; unstable SFE of basal $\langle a \rangle$ or pyramidal II $\langle c+a \rangle$ and their ratio.....	37
Figure 1.25	Thermal activation of cross-slip..	38
Figure 1.26	Temperature (homologous T) dependencies of CRSS (ratio).....	39
Figure 1.27	Effects of alloying elements on solidus (homologous) temperature;	

	(1) Mg-X and (2) ZA alloys.....	40
Figure 1.28	Effects of increment or decrement on theoretical CRSS ratio; (1) increment in both and (2) decrement in only non-basal slip.....	43
Figure 1.29	Effects of alloying elements (Zn, Al, Ca and Y) on theoretical CRSS; (1) basal slip and (2) athermal stress of prismatic slip.....	44
Figure 1.30	Effects of alloying elements (Al and Y) on theoretical CRSS (ratio)..	45
Figure 1.31	Effects of Zn content on CRSS ratio; (1) CRSS of basal slip, (2) athermal stress of prismatic slip and (3) ratio.....	46
Figure 1.32	Effects of Zn content and grain size on CRSS ratio at room temperature; (1) CRSS of basal slip, (2) CRSS of prismatic slip and (3) ratio.....	47
Figure 1.33	Schematic drawing on compatibility deformation.....	50
Figure 1.34	Activation of hard slip mode near grain boundary; (1) AZ31 alloy after tension, (2) Ti bicrystal after compression and (3) schematic drawing on grain boundary hardening.	51
Figure 1.35	DRX behaviors with deformation condition; (1) NRX, (2) Ordinary DRX and (3) DRX mechanism map.	52
Figure 1.36	Summary on mechanisms for development of double peak basal texture..	53
Figure 1.37	Summary on mechanisms for development of rare-earth texture....	55
Figure 2.1	Extrusion process.....	56
Figure 2.2	Designation for specimen of extruded plate..	57
Figure 2.3	Extrusion conditions (extrusion pressure and speed).....	61
Figure 2.4	Plane strain compression process..	62
Figure 2.5	Designation for PSCed specimen..	64

Figure 2.6	Flow stress during two-step PSC of extruded plate; (1) first step PSC and (2) second step PSC.....	65
Figure 2.7	Flow stress during two-step PSC of cast specimen; (1) first step PSC and (2) second step PSC.....	67
Figure 2.8	Configurations of microstructures and pole figures for extruded plates and PSCed specimens.....	70
Figure 2.9	Designation of texture components in extruded plates and PSCed specimens; (1) SP texture, (2) DP texture, (3) TD (CD) texture and (4) ED (LD) texture.....	70
Figure 2.10	Texture specimens for extrusion remainder.....	71
Figure 3.1	Microstructures and textures of ZA alloys extruded at 230 or 260°C; (1) 30×3t-sectional and (2) 15×6t-sectional extrusions....	75
Figure 3.2	Microstructure and texture evolutions during extrusions of ZA alloys at 230 or 260°C; (1) ZA11-260, (2) ZA13-230 and (3) ZA61-260.....	76
Figure 3.3	SRX textures of extruded ZAx1 alloys after air-cooling or annealing at 400°C.....	77
Figure 3.4	Theoretical deformation textures developed during PSC with different CRSS ratio; (initial texture) SP texture, (1) 1:1:5:1, (2) 1:1:3:1, (3) 1:1:2:1 and (4) 1:1:1:1.....	78
Figure 3.5	Distributions of basal pole intensities (with tilt angle from ND to ED) of ZA alloys extruded at 230 or 260°C.....	79
Figure 3.6	Microstructures and textures of ZA alloys extruded at different temperatures; (1) ZA11, (2) ZA61 and (3) ZA63 alloys.....	82
Figure 3.7	Microstructure and texture evolutions of ZA11 alloys during extrusions at 260 or 400°C; (1) ZA11-260, (2) ZA11-400 and (3)	

	ZA11-260-6t..	83
Figure 3.8	SRX textures of ZA11-400 after air-cooling or annealing at 400°C..	84
Figure 3.9	Microstructure and texture evolutions of ZA61 alloys during extrusions at 260 or 400°C; (1) ZA61-260 and (2) ZA61-400..	85
Figure 3.10	Microstructure and texture evolutions of ZA63 alloys during extrusions at different temperatures; (1) 300, (2) 340 and (3) 400°C..	86
Figure 3.11	Microstructure and texture evolutions of ZA6x alloys during extrusions; (1) ZA63-340, (2) ZA61-400 and (3) ZA63-400..	87
Figure 3.12	Theoretical deformation textures developed during PSC with different CRSS ratio; (initial texture) ZA11-400 (Die 2), (1) 1:1:9:9, (2) 5:1:9:9, (3) 9:1:9:9 and (4) 9:1:5:9.....	88
Figure 3.13	Theoretical deformation textures developed during PSC with different CRSS ratio; (initial texture) random texture, (1) 1:2:5:5, (2) 1:2:3:5 and (3) 1:2:1:5.....	89
Figure 3.14	Distributions of basal pole intensities (with tilt angle from ND to ED or TD) of ZA alloys (ZA11, ZA61 and ZA63) extruded at different temperatures.....	90
Figure 3.15	Microstructures and textures of extruded Ca-containing Mg or ZA alloys; (1) comparison between Ca and Ce effects and (2) effects of Zn and Ca contents..	93
Figure 3.16	Microstructures and textures of extruded Ca-containing ZA61 alloys; (1) ZA61Ca1 alloys extruded at different temperatures and (2) effects of Zn, Al and Ca contents.....	94
Figure 3.17	Microstructure and texture evolutions of Ca-containing Mg alloys during extrusions; (1) Mg-0.6Ca-450, (2) Mg-7Y-1Zr-400 and (3)	

	Mg-0.2Ce-400.....	95
Figure 3.18	SRX textures of Ce0.2-400 (Mg-0.2Ce alloy extruded at 400°C) after air-cooling or annealing at 400°C.....	96
Figure 3.19	Microstructure and texture evolutions of Ca-containing ZA alloys during extrusions at 340°C; (1) ZA11Ca1, (2) ZA61Ca1 and (3) ZA61Ca2 alloy.....	97
Figure 3.20	Microstructure and texture evolutions of ZA61Ca1 alloys during extrusions at different temperatures; (1) 260, (2) 340 and (3) 400°C... ..	98
Figure 3.21	Theoretical deformation textures developed during PSC with different CRSS ratio; (initial texture) Z1Ce0.2-400 (Die 2), (1) 1:9:9:9, (2) 9:1:9:9, (3) 9:1:5:9 and (4) 9:1:5:1... ..	99
Figure 3.22	Distributions of basal pole intensities (with tilt angle from ND to ED or TD) of extruded Ca-containing ZA alloys; (1) Ce or Ca solubility (phase diagrams) and (2) basal pole intensities.. ..	100
Figure 3.23	Summary; analysis on (1) DP texture based on grain size and (2) ED texture based on solidus temperature.. ..	104
Figure 4.1	Microstructures and textures of extruded ZA _x 1 alloys before second step PSC in two-step PSC; (1) initial state and (2) after first step.....	106
Figure 4.2	Microstructures and textures of extruded ZA _x 1 alloys after second step PSC at different temperatures (200 ~ 550°C) with initial strain rate of 0.0002 or 0.0400/sec in two-step PSC (CA//TD).. ..	109
Figure 4.3	Microstructures and textures of extruded ZA _x 1 alloys after second step PSC at different temperatures (200 ~ 550°C) in two-step PSC (CA//ED).....	113

Figure 4.4	Microstructure and texture evolutions of extruded ZA61 alloys during second step PSC at different temperatures (200 ~ 450°C) in two-step PSC (CA // TD).....	117
Figure 4.5	Texture evolution of extruded ZA61 alloy during second step PSC at 400°C in two-step PSC (CA // ED).....	119
Figure 4.6	Microstructure and texture evolutions of ZA x 1 alloys during second step PSC above 400°C in two-step PSC (CA // TD).....	120
Figure 4.7	Microstructure and texture evolutions of extruded ZA x 1 alloys during second step PSC at 400°C in two-step PSC (CA // ED)....	121
Figure 4.8	Theoretical deformation textures developed during PSC with different CRSS ratio; (initial texture) SP texture of ZA61-260-6t-TD/ND-RT/0.1-260/0.12, (1) 1:1:1:1, (2) 1:1:2:1 and (3) 1:1:5:1.	122
Figure 4.9	Theoretical deformation textures developed during PSC with different CRSS ratio; (initial texture) texture of ZA61-260-6t-ED/ND-RT/0.1-400/0.05, (1) 1:1:1:1, (2) 1:1:2:1 and (3) 1:1:5:1.	123
Figure 4.10	Theoretical deformation textures developed during PSC with CRSS ratio of 9:1:1:1; (initial texture) DP + CD texture of ZA61-260-6t-ED/ND-RT/0.1-400/0.40.....	124
Figure 4.11	Microstructures and textures of annealed ZA61 alloys after second step PSC at different temperatures (260 ~ 450°C) with initial strain rate of 0.0002 or 0.0400/sec in two-step PSC (CA // TD).....	127
Figure 4.12	Microstructures and textures of annealed ZA61 alloys after second step PSC at different temperatures (260 ~ 450°C) in two-step PSC (CA // ED).....	129
Figure 4.13	Microstructures and textures of cast ZA alloys before second step PSC in two-step PSC; (1) initial state and (2) after first step..	131

Figure 4.14	Microstructures and textures of cast ZA alloys after second step PSC at different temperatures (300 ~ 500°C) in two-step PSC; (1) ZA63, (2) ZA19 and (3) ZA31 alloys.....	135
Figure 4.15	Microstructure and texture evolutions of cast ZA63 alloys during second step PSC at 300 or 320°C in two-step PSC.....	137
Figure 4.16	Microstructure and texture evolutions of cast ZA63 alloys during second step PSC at 450°C with different strain rates in two-step PSC; (1) 0.0002/sec, (2) 0.4000/sec and (3) different strain rates..	138
Figure 4.17	Microstructures and textures of cast ZA63 alloys after second step PSC at 320 or 400°C with different strain rates in two-step PSC; (1) two-step PSC at 230 ~ 310°C, (2) 320°C, (3) 400°C and (4) flow stress..	139
Figure 4.18	Texture of cast ZA63 alloy after second step PSC at 260°C with 0.0002/sec in two-step PSC.	140
Figure 4.19	Texture of cast ZA63 alloy after second step PSC at 320°C with 0.0800/sec in two-step PSC.	141
Figure 4.20	Microstructures and textures of cast ZA63 alloys after PSC at different temperatures (300 ~ 450°C); (1) one-step PSC with 0.0002/sec, (2) one-step PSC with 0.4000/sec and (3) two-step PSC (ROT).....	144
Figure 4.21	Microstructures and textures of cast ZA63 alloys after one-step PSC at 400 or 450°C with different strain rates (0.0002 ~ 0.4000/sec); (1) evolution at 400°C with 0.4000/sec, (2) 400°C and (3) 450°C.....	146
Figure 4.22	Texture evolution of cast ZA63 alloy during one-step PSC at 400°C with 0.4000/sec.....	147

Figure 4.23	Microstructures and textures of cast ZA alloys after second step PSC at different temperatures (300 ~ 450°C) in two-step PSC (ROT); (1) ZA63, (2) ZA61 and (3) ZA19 alloys..	148
Figure 4.24	Microstructures and textures of cast ZA61Ca1 alloys after second step PSC at different temperatures (260 ~ 400°C) in two-step PSC; (1) ZA61, (2) ZA61Ca1 and (3) ZA31 alloys.....	151
Figure 4.25	Summary; comparison between effects of (1) Zn content and (2) initial grain size on DP texture (two-step PSC (CA // TD)) developed at low temperature.....	158
Figure 4.26	Summary; analysis on effects of Zn content on DP texture (two-step PSC (CA // TD) or (CA // ED)) developed at high temperature based on effects of Zn content on solidus temperature.....	159
Figure 4.27	Summary; analysis on grain size and critical temperatures ($T_{DP, low}$ and $T_{DP, high}$) based on solidus temperature.....	160
Figure 4.28	Summary; analysis on intensity of CD and LD Textures based on (1) solidus temperature and (2) grain size..	161
Figure 4.29	Summary; flow chart for texture development..	162

Chapter 1 Introduction

1.1 Research Objectives

Figure 1.1 shows the effects of texture on mechanical properties in the extruded Mg-Zn-Al alloys of this study [1,2]. It shows the relative activity evolutions during the tensile deformation derived from the flow stress simulations. As shown in figure 1.1, spread of the basal poles toward the extrusion direction (ED spread) increased instead of decrease in spread of the basal poles toward the transverse direction (TD spread) with increase in Zn content. And the grain size decreased with increase in Zn content. In the tensile flow curves along ED (TA // ED), with increase in Zn content, yield stress decreased because of easier activation of the basal slip at lower stress caused by increase in ED spread, even though grain size strengthening effect. On the contrary, in the tensile flow curves along TD (TA // TD), yield stress increased with increase in Zn content because of harder activation of the basal slip at higher stress caused by decrease in TD spread. Moreover, with increase in Zn content, uniform elongation toward ED increased because of higher activity of the basal slip caused by increase in ED spread in addition to uniform elongation increment by grain refinement. In the ZA61 alloy, uniform elongation toward ED was larger than one toward TD. However, in the ZA11 alloy, uniform elongation toward TD was larger than one toward TD because of higher activity of the basal slip in tensile deformation toward TD caused by larger spread toward TD than ED. Like this example, initial texture has a decisive effect on mechanical property. Therefore, to enhance the

mechanical property, researches on texture development mechanism is necessary.

Relatively clear results on relationship between texture and mechanical property have been reported, on the contrary, researches on texture development mechanisms have been progressed case-by-case. Therefore, many possible mechanisms were proposed.

In this study, to control the texture of the Mg alloys, effects of the extrusion temperature and alloying elements on textures of the extruded Mg-Zn-Al alloys were investigated. And their mechanisms were systematically studied using the various ZA alloys extruded or casted by the two-step PSC tests. And PSC results were analyzed in the viewpoint of grain size and solidus temperature.

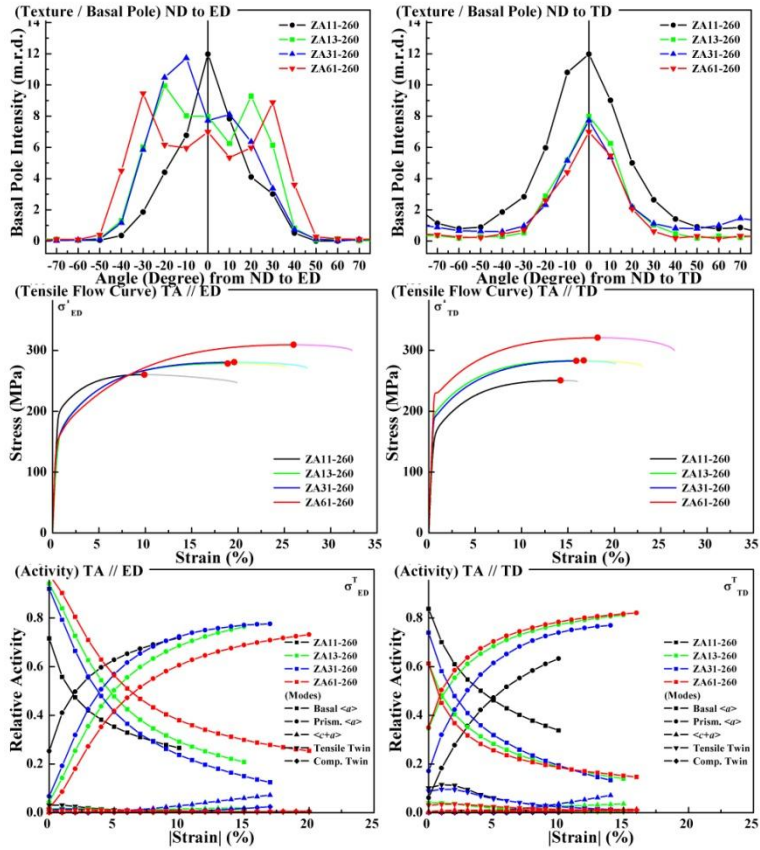
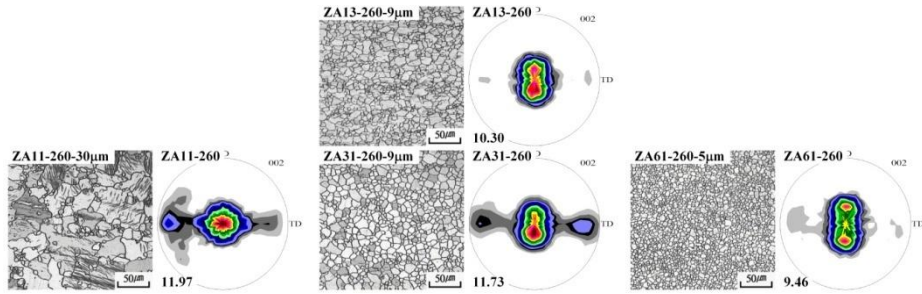


Figure 1.1 Effect of texture on mechanical property; basal pole intensity distribution (from ND to ED or TD), tensile flow curve (TA // ED or TD) and relative activities derived from the flow stress simulations.

1.2 Theoretical deformation texture

Figure 1.2 shows the changes in theoretical deformation textures developed from the random texture during the PSC (plain strain compression) with the relative CRSS (critical resolved shear stress) ratios (basal $\langle a \rangle$ slip : prismatic $\langle a \rangle$: pyramidal II $\langle c+a \rangle$: tensile twin) of the deformation modes. And Figure 1.3 shows the theoretical deformation textures developed from the SP texture (single peak basal texture) during the PSC. Evolutions of the relative activities during their deformations were shown in Figure 1.4. Results are represented as follows [3-7];

(Case 1 - basal $\langle a \rangle$ slip-dominated deformation) spread of the basal poles toward the LD (longitudinal direction) became narrower and finally strong SP texture was developed.

(Case 2 - prismatic $\langle a \rangle$ slip-dominated deformation) texture component whose basal poles were parallel to the CD (constraint direction) and two among six prismatic poles were parallel to the LD was developed. Compared with the basal slip-dominated deformation, overall texture intensity was low.

(Case 3 - pyramidal II $\langle c+a \rangle$ slip-dominated deformation) texture component whose basal poles were parallel to the LD (LD texture) was developed.

(Case 4 - basal and $\langle c+a \rangle$ slip-combined deformation) DP texture (double peak basal texture) was developed. And the tilt angle corresponding to the peak in DP increased with increase in activity of the pyramidal II $\langle c+a \rangle$ slip.

(Case 5 - basal and $\langle c+a \rangle$ slip-combined deformation without twin) LD texture was developed with DP texture. Intensity of the LD texture increased with increase in activity of the pyramidal II $\langle c+a \rangle$ slip.

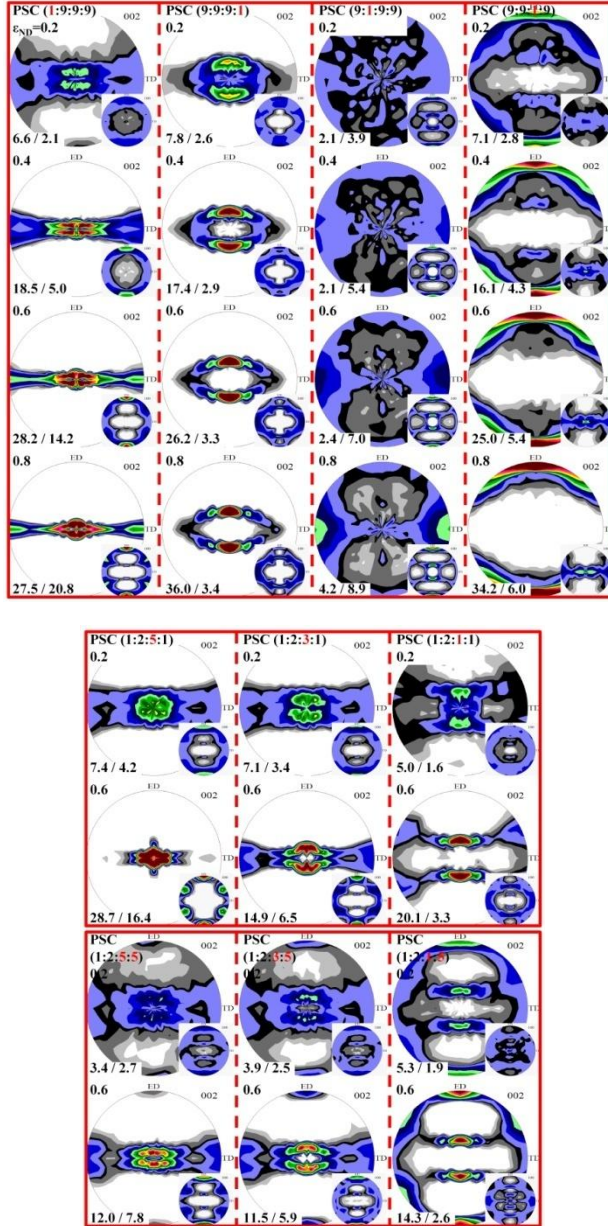


Figure 1.2 Theoretical deformation textures developed during PSC with different CRSS ratios (basal $\langle a \rangle$: prismatic $\langle a \rangle$: pyramidal II $\langle c+a \rangle$: tensile twin) (from random texture); (1) 1:9:9:9, (2) 9:9:9:1, (3) 9:1:9:9, (4) 9:9:1:9, (5) 1:2: x :1 and (6) 1:2: x :5.

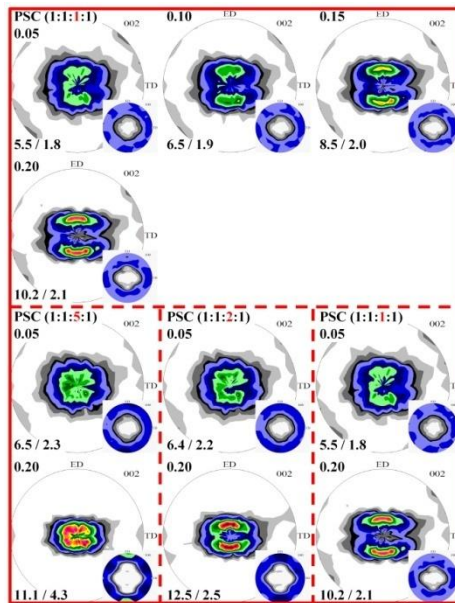
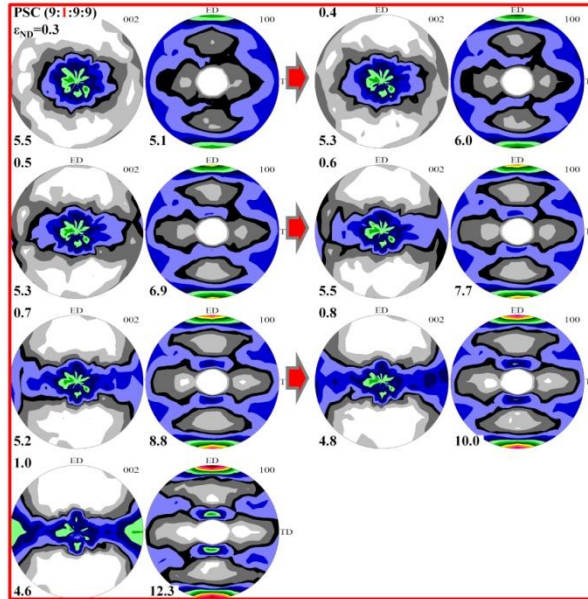


Figure 1.3 Theoretical deformation textures developed during PSC with different CRSS ratios (from single peak basal texture); (1) 9:1:9:9 and (2) 1:1: x :1.

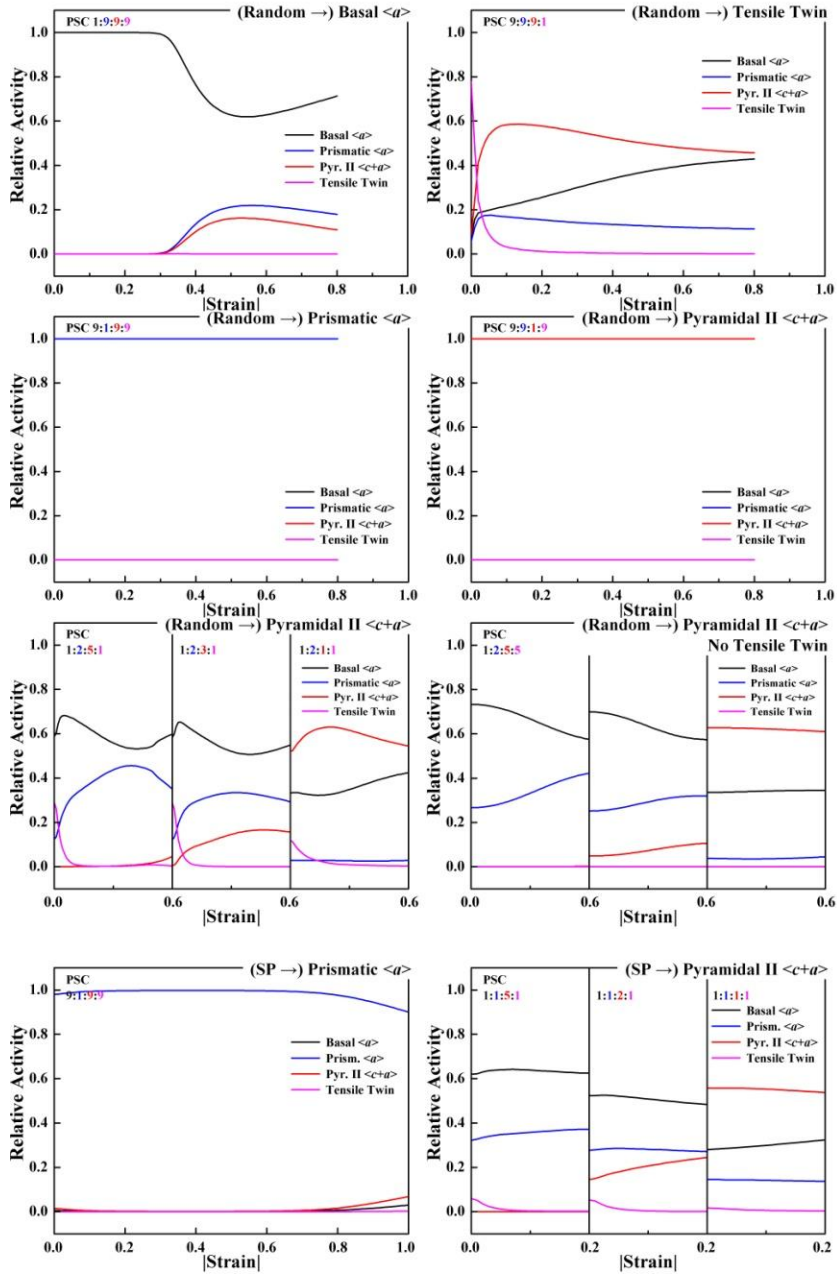


Figure 1.4 Evolutions of Relative activities for theoretical deformation textures during PSC.

1.3 Recrystallization texture

In magnesium alloys, three DRX (dynamic recrystallization) mechanisms are now understood to be operative as follows [8];

1. Continuous DRX (CDRX): This mechanism includes the formation of three dimensional arrays of deformation low-angle boundaries (LABs) followed by their gradual transformation into high-angle boundaries (HABs) upon straining. New grains are formed progressively within deformed original grains from the continuous increase in misorientation across deformation-induced boundaries.

2. Discontinuous DRX (DDRX): This mechanism involves the development of HABs via the nucleation and growth of new grains. Nuclei evolve on original grain boundaries due to their bulging caused by the difference in dislocation density between neighboring grains. The local migration of grain boundaries lead to the formation of nuclei, which then grow out and consume a deformed matrix, resulting in decrease in dislocation density.

3. Twin DRX (TDRX): This mechanism is associated with twinning, in which twinning leads to the formation of coarse lamellae surrounded by special grain boundaries. There are at least three processes by which this can occur: Mutual intersection of primary twins, the occurrence of secondary twinning within the coarse lamellae, the subdivision of coarse twin lamellae by deformation-induced LABs, the transformation of LABs into conventional HABs with further straining.

Repetitive cycling of either CDRX or DDRX can potentially develop necklace-type structure. These DRX mechanisms were mapped by Sitdikov *et al.* [9,10] in the temperature versus strain diagram shown in Figure 1.5.

However, regardless of which DRX mechanism CDRX or DDRX, the sharp texture induced by the deformation process sustains through the recrystallization process in the conventional Mg alloys like AZ31 alloy [9]. It is usually observed that the recrystallization of Mg alloys is not accompanied with an obvious change of texture, in contrast to fcc materials, where the recrystallization texture is usually very different from the deformation texture [6]. This is because the DRXed grains adopt orientations broadly centered around the orientation of the parent deformed grains as shown in Figure 1.6 ~ 1.8 [12-15]. Although DRX does nucleate grains with broader basal texture, these DRXed grains are deformed during continued processing. Once they are deformed, their textures are rotated back into a basal orientation [11]. Nonetheless, some texture changes occur even in the conventional Mg alloys during the annealing process (SRX, static recrystallization) performed after deformation process (DRX) as follows [16-21];

(SRX texture)

1. Overall texture intensity can decrease because texture distribution of the DRXed grains is relatively broader than that of the parent grains [11]. However, annealing of the fully DRXed materials can result in the increase in intensity of the basal texture as shown in Figure 1.9 and Figure 1.11 [16,19].
2. (Change in c-axis alignment) double peaks in the basal poles can be replaced by the single peak as shown in Figure 1.9 [16].
3. (Change in a-axis alignment) $\{0001\}\langle 11-20 \rangle$ texture becomes pronounced instead the pre-existing $\{0001\}\langle 10-10 \rangle$ deformation texture weakens as shown in Figure 1.10 and 1.11 [17-21].

These phenomena were also observed in the extruded Mg-Zn-Al alloys of this study.

However, recently, texture weakening phenomena of the severely deformed

Mg sheets after annealing process have been reported for the rare-earth (RE)-containing Mg sheets [23-26] or high temperature-rolled [27,28] or high speed-rolled Mg-Zn-Al sheets [29-31]. To understand these impacts of DRX mechanisms on recrystallization textures, it is better to classify them based on their nucleation sites as follows [23];

1. Grain boundary nucleation (RDRX, Rotational DRX): Locally activated non-basal slip or kink in grain mantle region near the grain boundaries accommodates a significant amount of plastic strain and produces a lattice rotation, leading to nucleation of new fine grains which have tilted basal planes near the original grain boundaries by the migration of sub-grain boundaries formed by the geometrically necessary dislocations [22].

2. Particle-stimulated nucleation (PSN): While high density of fine particles can pin boundaries and retard recrystallization, coherent large particles can act as nucleation sites. And the PSN provides randomly oriented nuclei. However, its contributions to the recrystallized microstructure and texture are relatively small because of the small fraction of PSNed grains unless they grow severely. Moreover, PSN does not give rise to well-defined orientations but provides overall texture weakening and texture scatter.

3. Deformation twin nucleation (DTN): Deformation twins, especially compression twin and double twin, can act as nucleation sites for recrystallization. Because compression and double twin rotate the matrix into a favorable orientation to basal slip and act as obstructers for dislocation, higher stored energy can be build up within the twins than the surrounding matrix.

Moreover, they have a potential to modify the recrystallization texture owing to the fact that the different twin variants of primary and secondary twinning induces various crystallographic rotations even though usually TDRXed grains adopt similar orientations to the parent twins.

4. Shear band nucleation (SBN): Shear bands, which occur in the form of non-crystallographic band-like deformation regions of highly concentrated plastic flow, are one of the most frequently observed microstructural features in plastically strained ductile metallic materials. They are characterized by massive collective dislocation or twinning activity in a narrow deformation zone while the abutting matrix undergoes comparably low plastic flow [72]. The high stored energy in the shear bands makes them ideal sites for recrystallization. In magnesium, although SBNe grains are thought to have similar orientations to the matrix within the shear band, parent shear banding regions consisted of compressive and double twins have different textures whose basal planes are aligned parallel to the shear band plane with the abutting matrix [11]. Moreover, because twinning-related shear bands are generally very heterogeneous and have large internal orientation spreads, SBNe grains can have a wide spectrum of orientations [23]. Recently, SBNe recrystallization textures have received particular attention in Mg-RE and Mg-Zn-RE alloys because of their weak and broad textures developed after annealing process as shown in Figure 1.12 and Figure 1.13 [23-26].

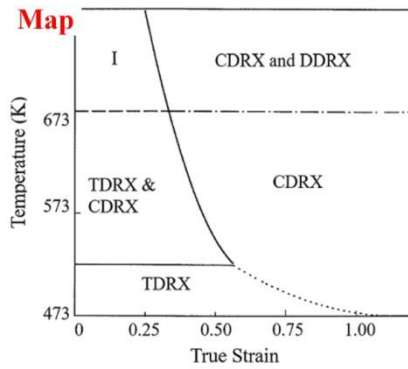
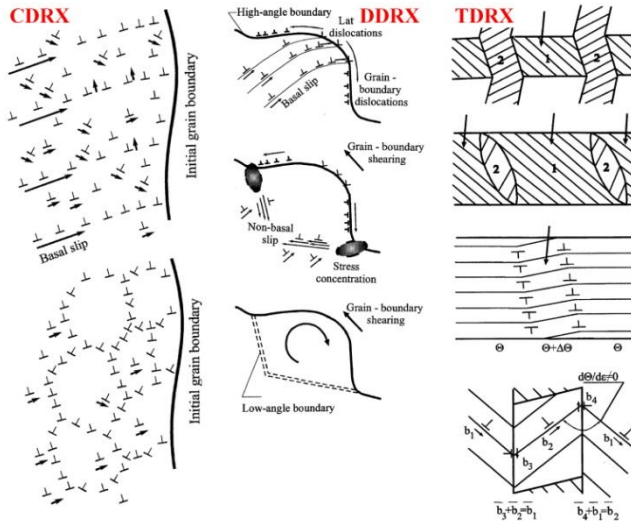


Figure 1.5 DRX mechanisms and map for pure Mg deformed at temperatures ranging from 293 to 773 K [9,10]; (1) CDRX, (2) DDRX, (3) TDRX and (4) Map.

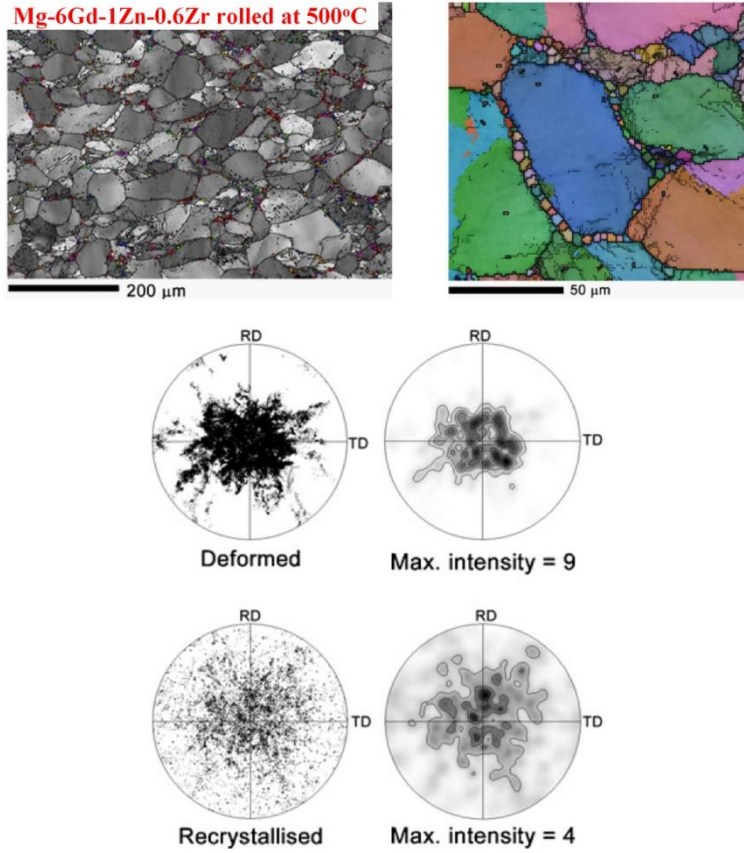


Figure 1.6 Difference in textures between parent and DRXed grains of Mg-6Gd-1Zn-0.2Zr (wt.%) alloy rolled at 500°C [12].

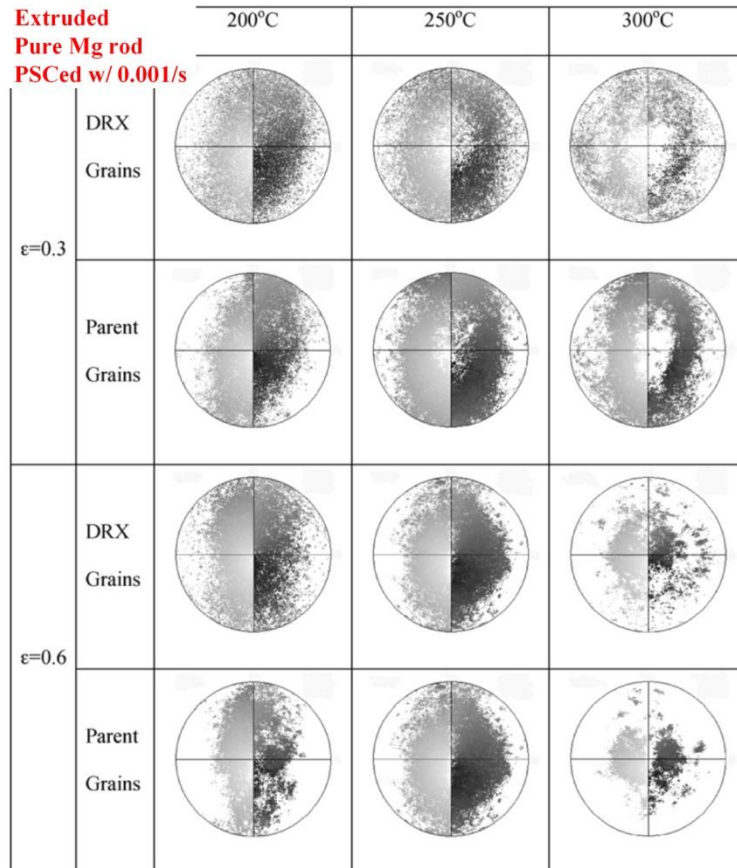
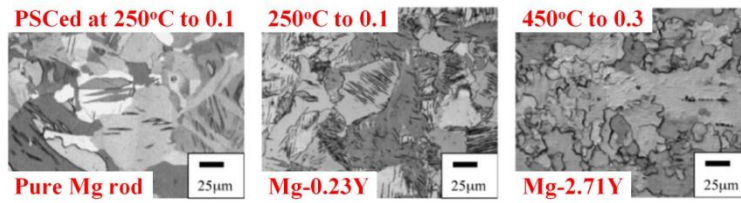


Figure 1.7 Difference in textures between parent and DRXed grains of extruded pure Mg and Mg-Y (0.23, 0.84, 2.71wt.%) alloy rods PSCed at various temperatures with 0.001/s [13].

		$\epsilon=0.3$		$\epsilon=0.6$	
		ξ X Grains	Parent Grains	DRX Grains	Parent Grains
Extruded Mg-Y rod PSCed w/ 0.001/s	Mg 0.23wt%Y 250°C				
	Mg 0.23wt%Y 300°C				
	Mg 0.84wt%Y 400°C				
	Mg 2.71wt%Y 450°C				

Figure 1.7 Continued [13].

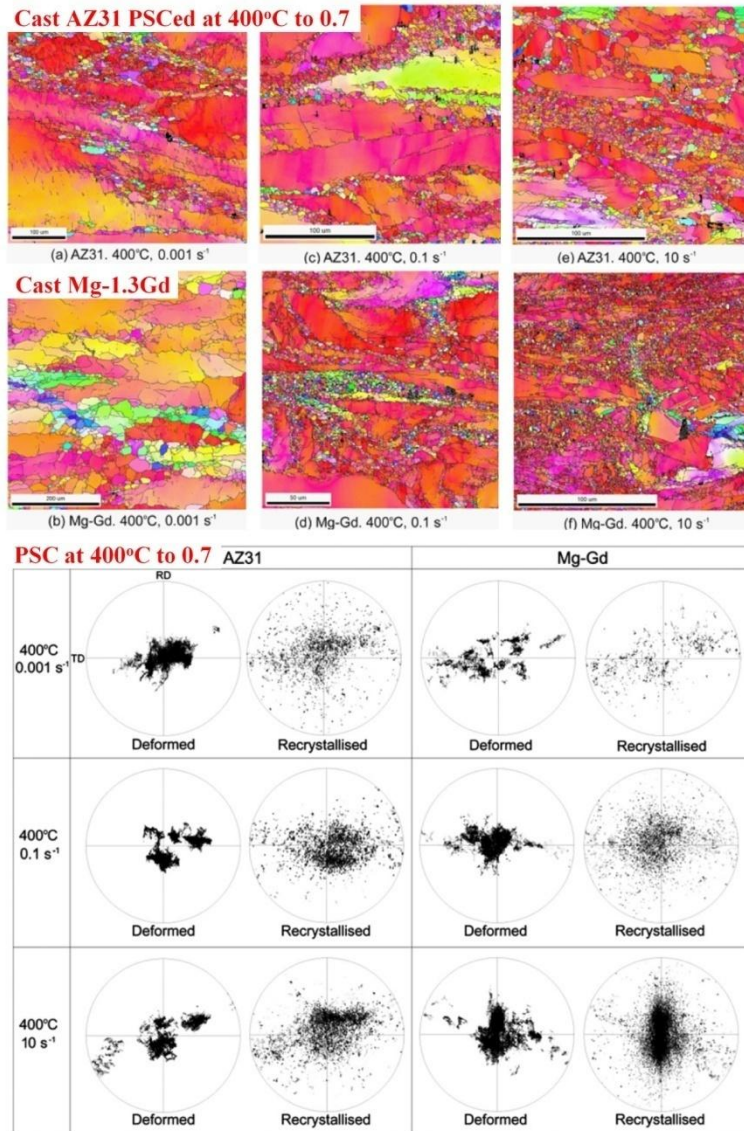


Figure 1.8 Difference in textures between parent and DRXed grains of cast AZ31 and Mg-1.3Gd alloys PSCed at 400°C with various strain rates to a true strain of 0.7 [14,15].

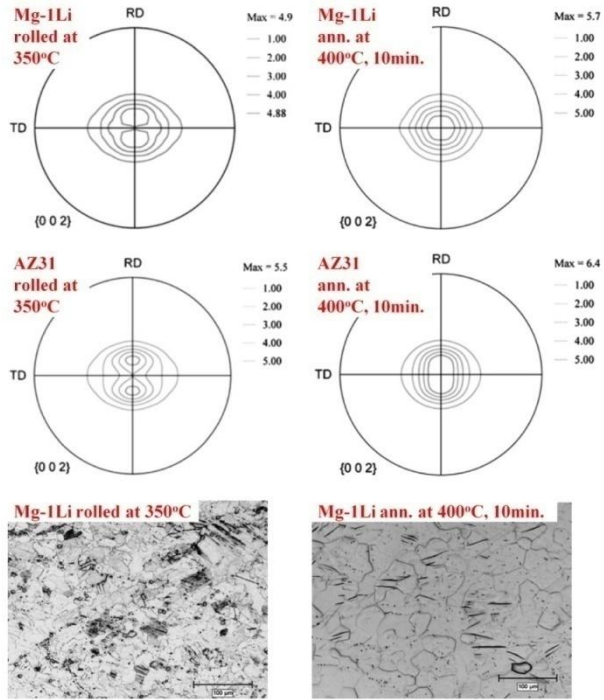


Figure 1.9 Change in textures of hot rolled Mg-1Li (wt.%) and AZ31 alloy sheets during grain growth annealing at 400°C [16].

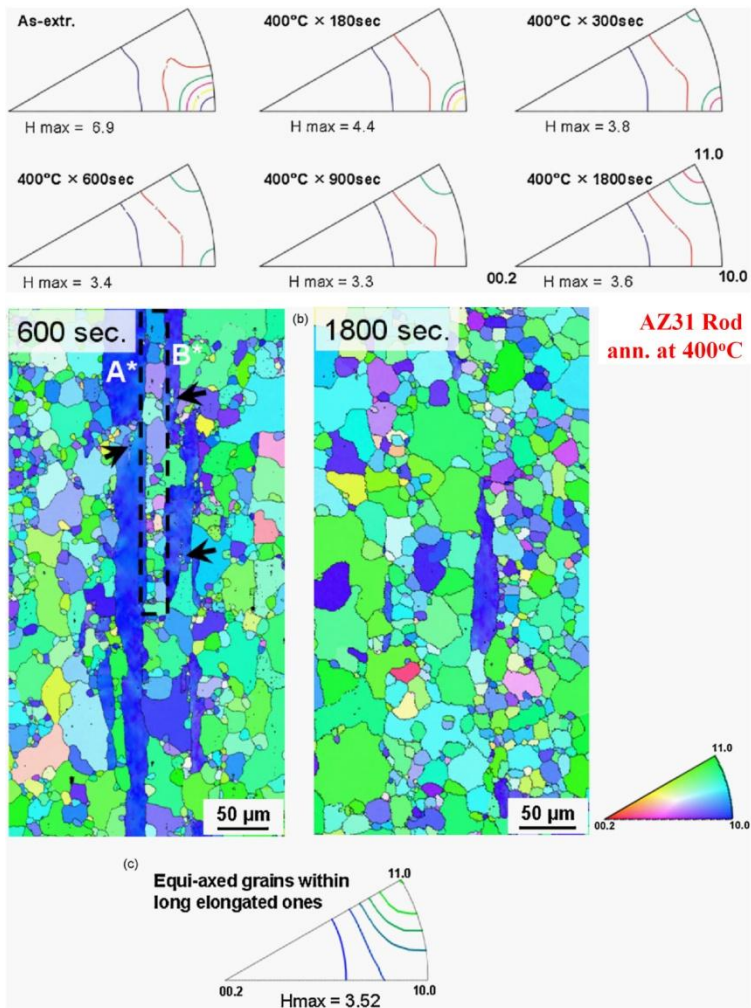


Figure 1.10 Change in texture (IPF of ED) of warm extruded AZ31 alloy rod during grain growth annealing at 400°C [17]; (1) SRX texture change and (2) consumption process of parent grains by SRXed grains.

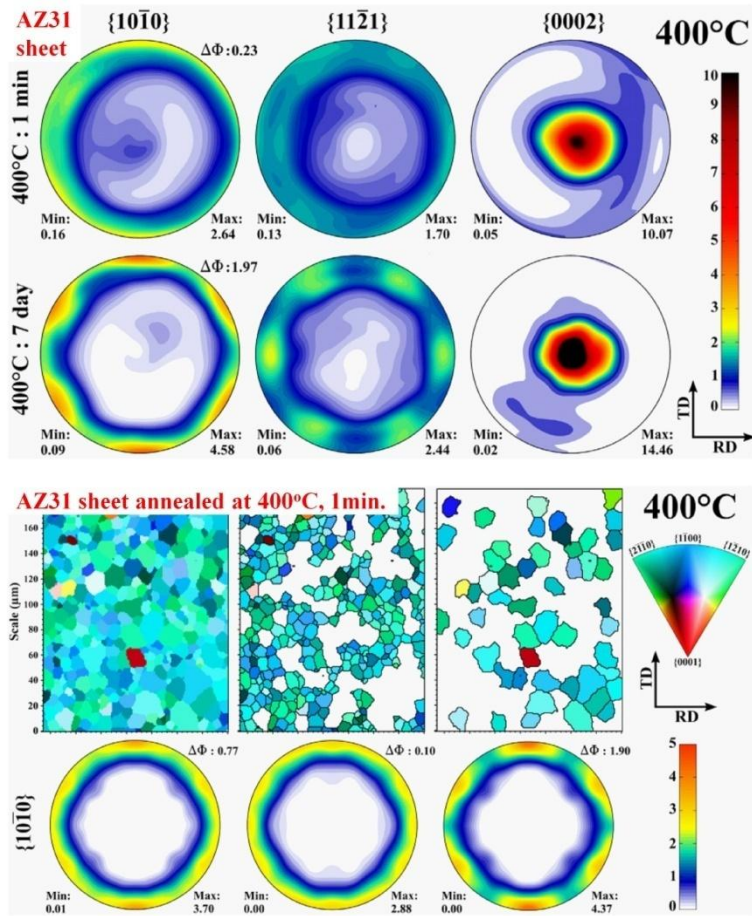


Figure 1.11 Change in texture of warm rolled AZ31 alloy sheet during grain growth annealing at 400°C [19]; (1) SRX texture change and (2) relationship between grain size and {0001}<11-20> texture at initial stage.

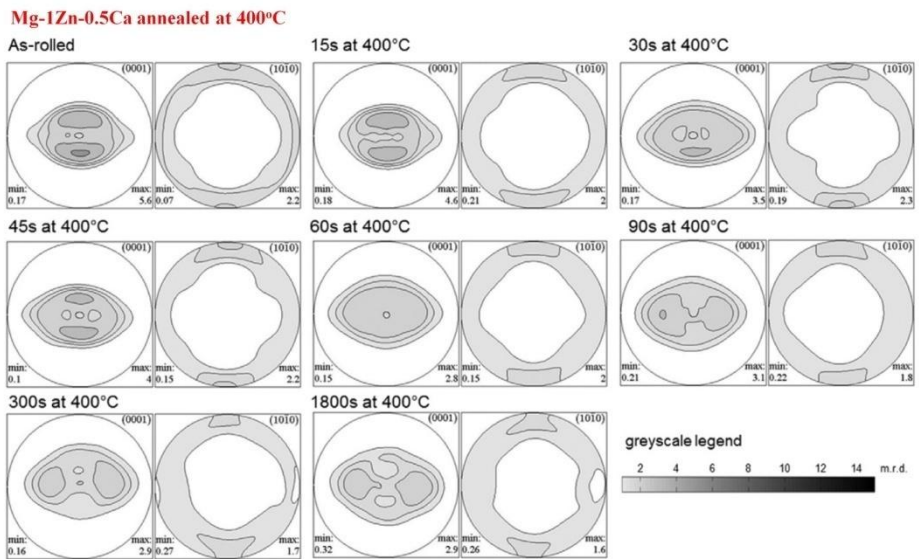
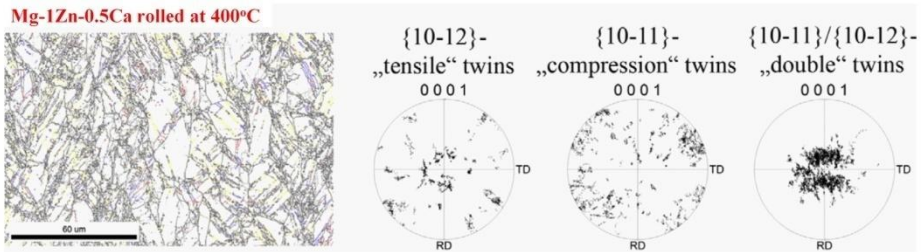


Figure 1.12 SBNeD recrystallization texture of Mg-1Zn-0.5Ca (wt.%) alloy rolled at 400°C after annealing process at 400°C [26].

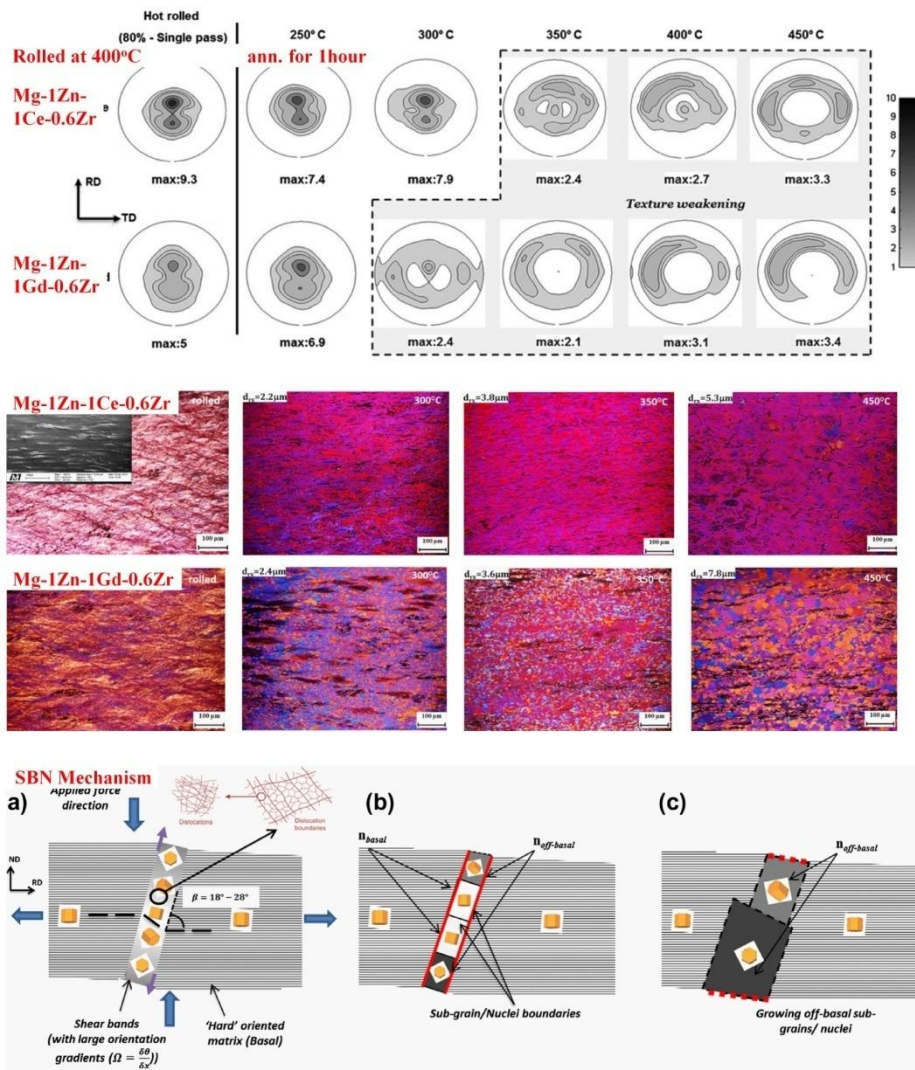


Figure 1.13 SBNed recrystallization textures of Mg-1Zn-1Ce-0.6Zr and Mg-1Zn-1Gd-0.6Zr (wt.%) alloys rolled at 400°C after annealing process at various temperatures for 1hour [23].

1.4 Experimental observation of $\langle c+a \rangle$ dislocation

Besides basal $\langle a \rangle$ and prismatic $\langle a \rangle$ slip which accommodate the strains along the a-axis, more independent slip systems which can accommodate the strains along the c-axis are necessary to alleviate the compatibility stresses between distinctly-oriented grains. Besides twins which can accommodate only the limited strain along the c-axis, $\langle c+a \rangle$ slip is capable of accommodating strains along the c-axis. However, it is still controversial from the existence to its role on plastic deformation because of its large self-energy originated from its large Burgers vector [32]. In this chapter, several cases in which $\langle c+a \rangle$ dislocations were observed by TEM were introduced as follows;

In the single crystal study,

(Case 1 - c-axis compression of pure Mg single crystal)

(Figure 1.14) compression of pure Mg single crystal along c-axis at room temperature [33,34]

(Figure 1.15) compression of pure Mg single crystal along c-axis at various temperatures and temperature dependency of CRSS of pyramidal II $\langle c+a \rangle$ slip [35]

(Case 2 - [11-20] tension of Mg-7Li single crystal)

(Figure 1.16) tension of Mg-7Li (at.%) alloy single crystal along [11-20] at various temperatures and temperature dependency of yield stress [36,37]

In the polycrystal study,

(Case 1 - tension, c-axis compression, rolling or ECAP of Mg-Zn-Al alloys)

(Figure 1.17) tension of AZ31 alloy sheet at room temperature [38,39]

(Figure 1.18) compression of Mg-4.5Al-1Zn (wt.%) alloy sheet along near

c-axis at room temperature [40]

(Figure 1.19) rolling of Mg-4.5Al-1Zn (wt.%) alloy sheet at 180°C [41]

(Figure 1.20) back-pressure ECAP of AZ31 alloy at 200°C [42,43]

(Case 2 - c-axis compression or rolling of Mg-RE alloys)

(Figure 1.21) compression of Mg-15Li (at.%) alloy along near c-axis at room temperature [44]

(Figure 1.22) rolling of Mg-3Y (wt.%) alloy sheet at room temperature [45,46]

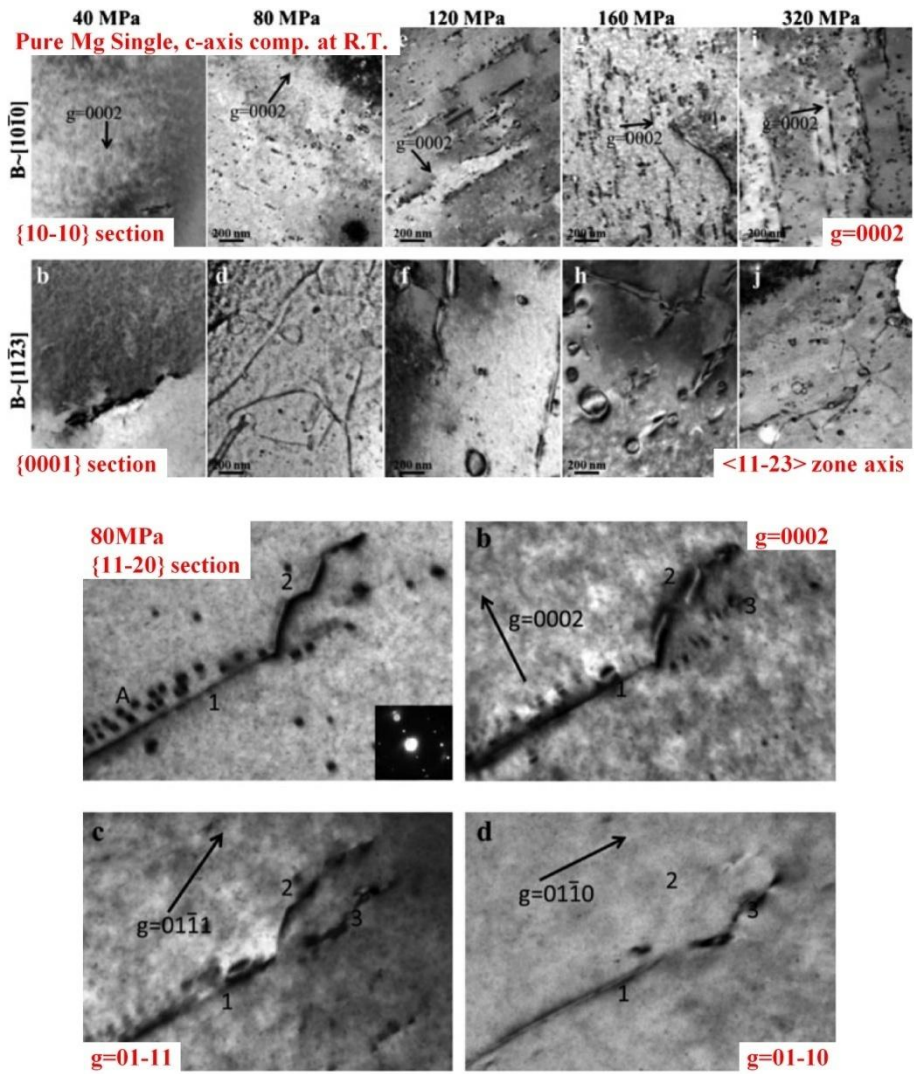


Figure 1.14 Observation of $\langle c+a \rangle$ dislocations in pure Mg single crystal compressed along c-axis at room temperature [33].

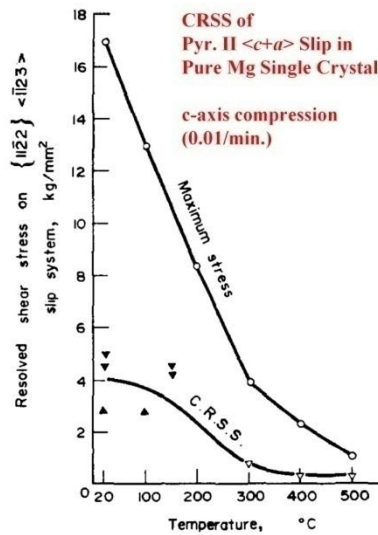
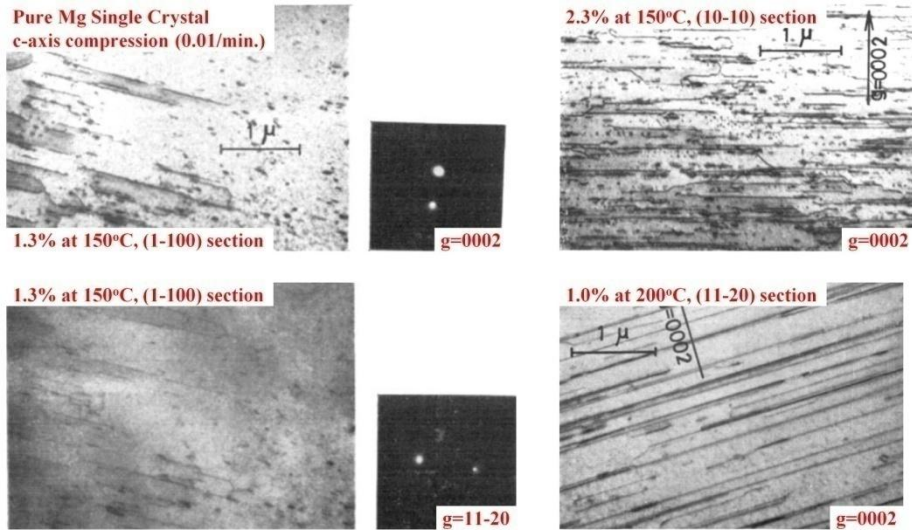


Figure 1.15 Observation of $\langle c+a \rangle$ dislocations in pure Mg single crystal compressed along c-axis at various temperatures with 0.01/min. [35]; temperature dependency of CRSS of pyramidal II $\langle c+a \rangle$ slip.

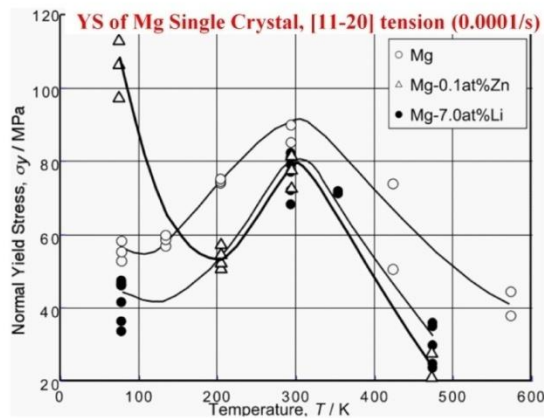
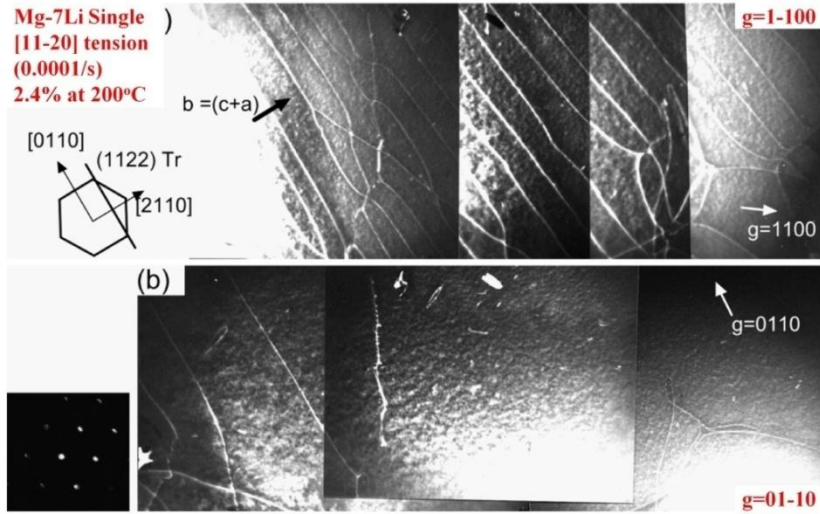


Figure 1.16 Observation of $\langle c+a \rangle$ dislocations in Mg-7Li (at.%) single crystal tensioned along [11-20] direction at various temperatures with 0.0001/s [36]; temperature dependency of yield stress.

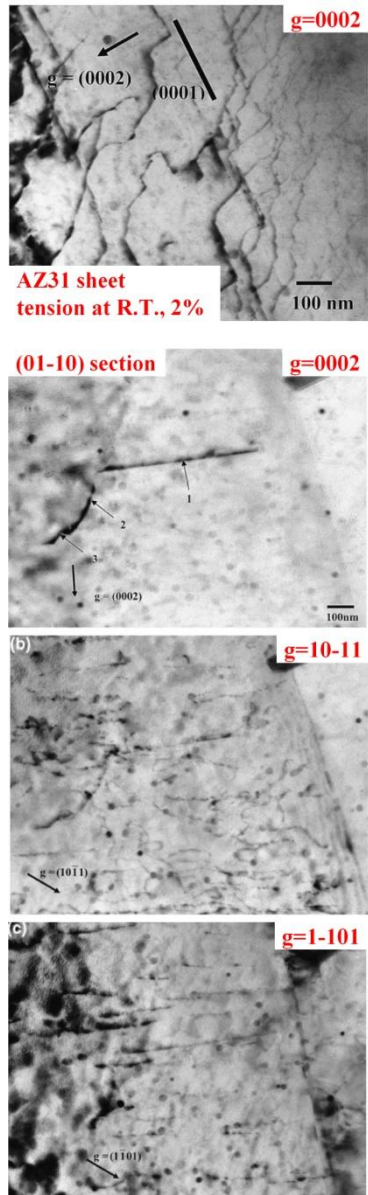


Figure 1.17 Observation of $\langle c+a \rangle$ dislocations in AZ31 alloy tensioned at room temperature to 2% [38]; (initial material) AZ31 sheet with fine recrystallized grains ($9 \mu\text{m}$) and double peak basal texture.

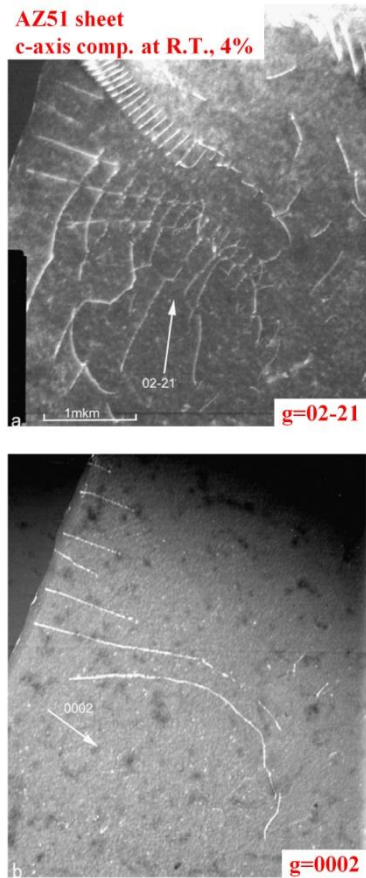


Figure 1.18 Observation of $\langle c+a \rangle$ dislocations in Mg-4.5Al-1Zn (wt.%) alloy compressed along c-axis at room temperature to 2~4% [40]; (initial material) Mg-4.5Al-Zn sheet rolled at 420°C with fine recrystallized grains (10 μm) and sharp basal texture.

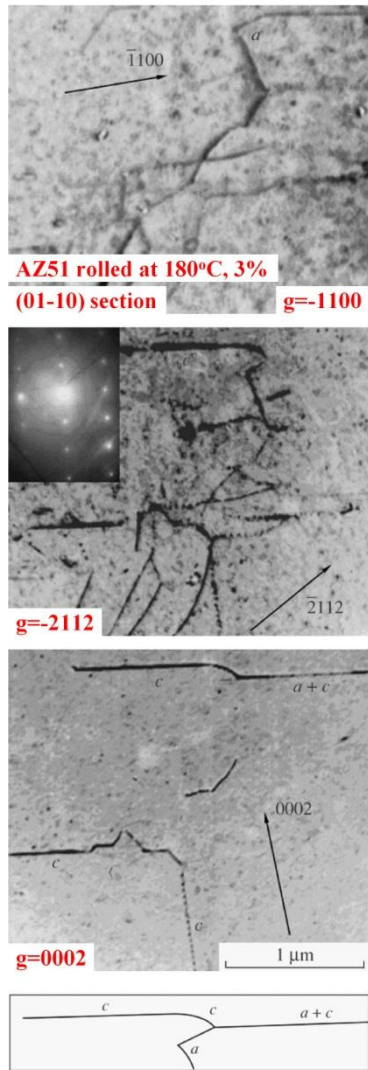


Figure 1.19 Observation of $\langle c+a \rangle$ dislocations in Mg-4.5Al-1Zn (wt.%) alloy rolled at 180°C to 2~3%; (initial material) Mg-4.5Al-Zn sheet rolled at 420°C with fine recrystallized grains (10 μm) and sharp basal texture [41].

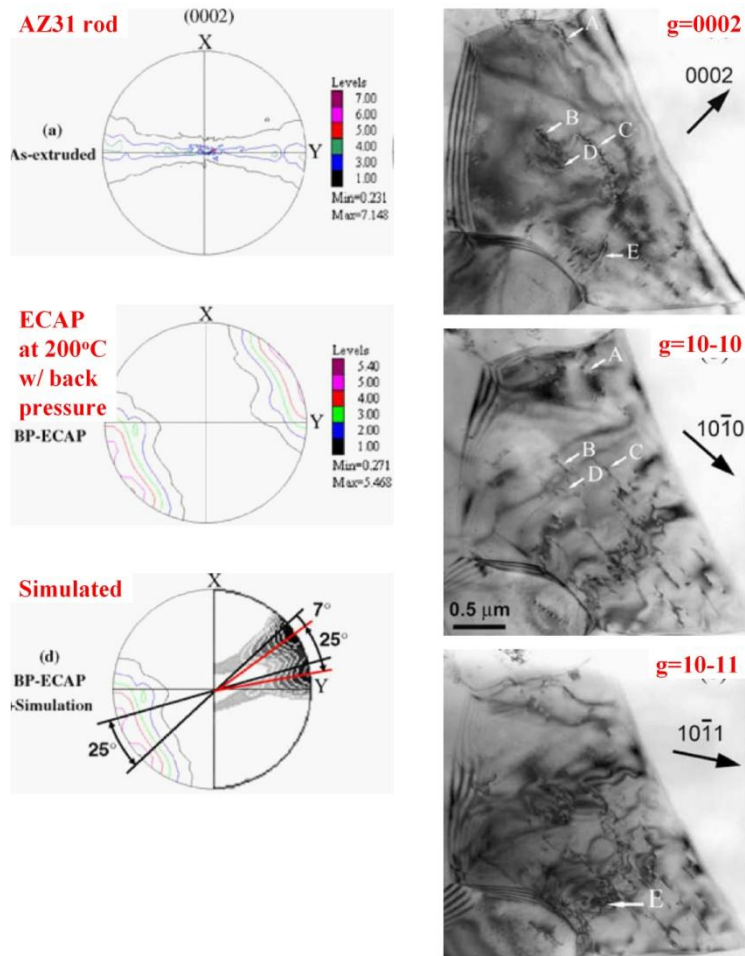


Figure 1.20 Observation of $\langle c+a \rangle$ dislocations in AZ31 alloy BP-ECAPed at 200°C [42]; (1) split of basal peak, (2) simulation by activation of $\langle c+a \rangle$ slip and (3) existence of $\langle c+a \rangle$ dislocations.

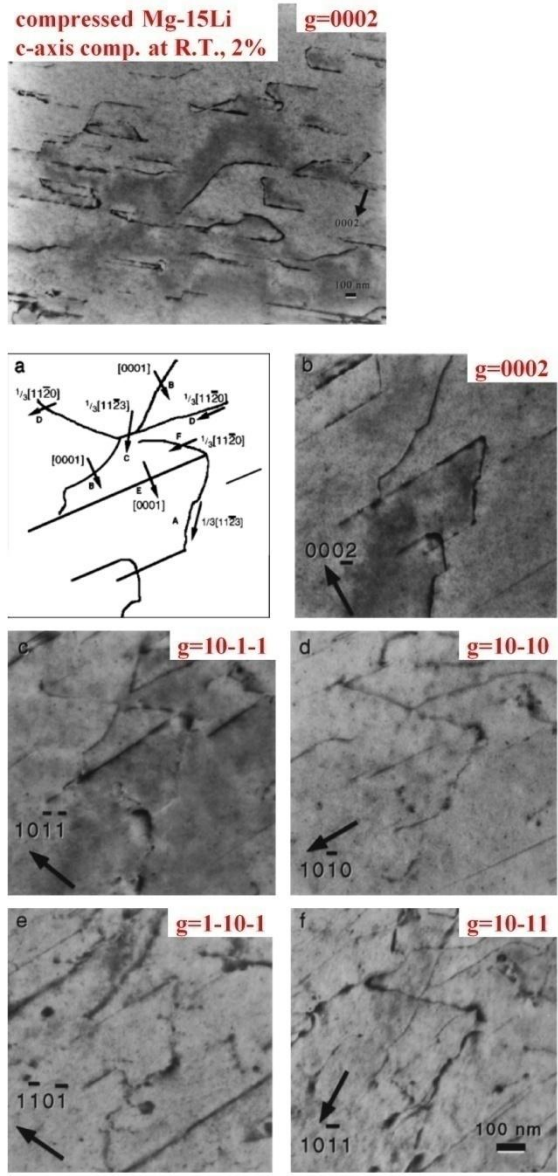


Figure 1.21 Observation of $\langle c+a \rangle$ dislocations in Mg-15Li (at.%) alloy compressed along c-axis at room temperature to 1~3% [44]; (initial material) cast Mg-15Li compressed at R.T. to 20% and annealed at 475°C for 1h with sharp basal texture.

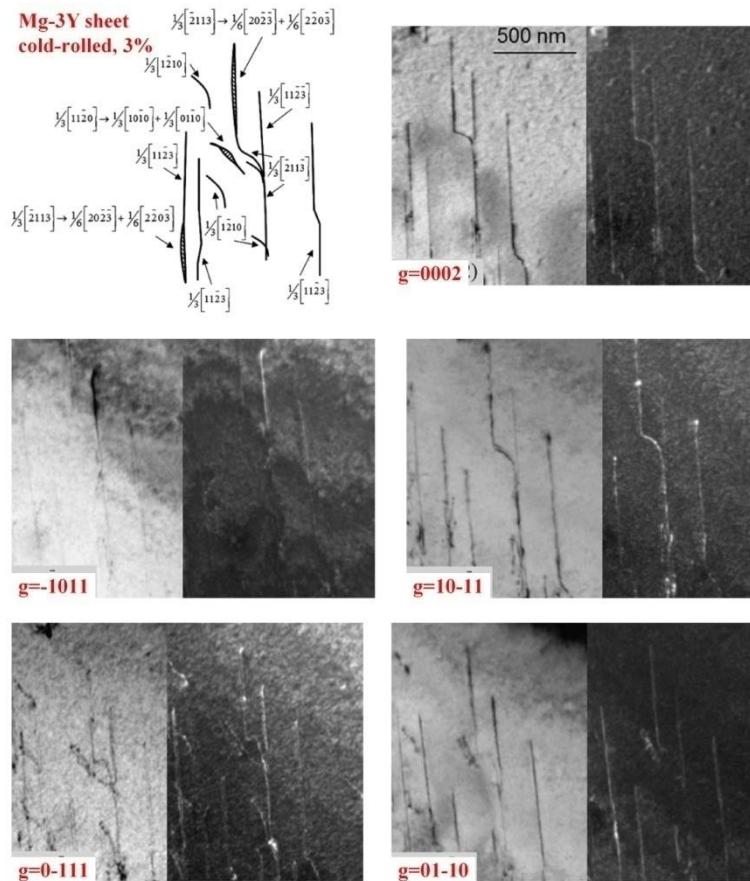


Figure 1.22 Observation of $\langle c+a \rangle$ dislocations in Mg-3Y (wt.%) alloy cold-rolled to 3% [45]; (initial material) Mg-3Y sheet rolled at 500°C to 50% and annealed at 500°C for 15min. with uniform recrystallized grains (35 μm).

1.5 Approach to activate non-basal slip

Figure 1.23 represents the four possible approaches to activate the non-basal slip based on Schmid's law. Approaches are represented as follows;

1. (Decreasing CRSS of non-basal slip) generally, with increase in temperature or decrease in strain rate, CRSS of the non-basal slip decreases.

2. (Increasing CRSS of basal slip) when Schmid factor ratio (non-basal to basal) larger than CRSS ratio (non-basal to basal), non-basal slip can be activated. The CRSS ratio decreases with increase in CRSS of the basal slip. Generally, addition of alloying elements or refinement of grain size increases the CRSS of basal slip.

3. (Increasing flow stress) when c-axis is parallel to the loading axis, non-basal slip can be activated by increasing ratio of flow stress to CRSS of non-basal slip. Generally, with decrease in temperature or increase in strain rate, flow stress increases.

4. (Increasing additional internal stress) compatibility stress originated from the grain boundary bonding force can be act as additional internal stress to make the non-basal slip activated.

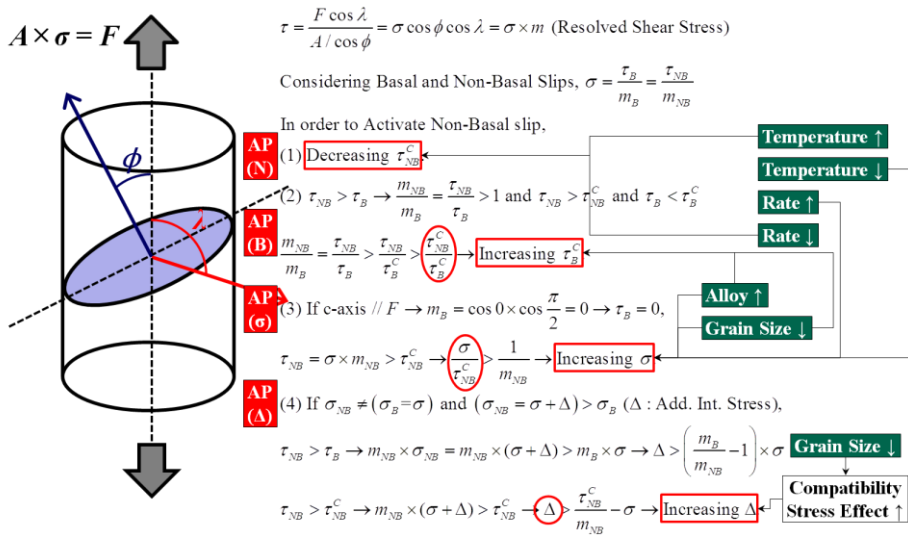


Figure 1.23 Approach to activate non-basal slip; (1) decreasing CRSS of non-basal slip, (2) increasing CRSS of basal slip, (3) increasing flow stress and (4) increasing additional internal stress.

1.5.1 Decreasing CRSS of non-basal slip

Figure 1.24 shows the effects of alloying elements on the theoretical unstable SFE (stacking fault energy) of pyramidal II $\langle c+a \rangle$ slip (calculated by A. Moitra *et al.*) [47]. It is known as the tendency to nucleate the dislocation increases with decrease in unstable SFE. Therefore, the $\langle c+a \rangle$ slip can be activated by increasing the unstable SFE ratio (basal to $\langle c+a \rangle$). Addition of Ca, Ce or Gd increased the unstable SFE ratio. However, addition of Zn or Al decreased the unstable SFE ratio.

Another possible approach to decrease the CRSS of the non-basal slip can be derived from the concept of the homologous temperature. Figure 1.25 represents the thermal activation process of the cross-slip (basal to prismatic plane). Preceding process of the cross-slip (constriction of the extended dislocation and formation of the double kink) can be activated by aid of the thermal vibrations of atoms [48,49]. And the amplitude of atomic vibrations is maximized near the melting temperature. Therefore, decrease in solidus temperature might result in decrease in cross-slip stress by increasing thermal vibrations. In that case, homologous temperature (temperature divided by solidus temperature) is useful as a substitute for temperature.

Figure 1.26 shows the temperature dependency of the CRSS (measured by M. C. Byun *et al.*) [50]. With increase in temperature, the CRSSes decreased. And the amount of decrease in the non-basal slip was much larger than that of the basal slip. Each temperature and CRSS can be converted into homologous temperature and CRSS ratio, respectively [51].

Figure 1.27 shows the effects of alloying elements on solidus and homologous temperature. With increase in alloying contents, the solidus temperature decreased. And the amount of decrease was largest in addition of Zn.

Therefore, the increase in homologous temperature was largest in addition of Zn. In the ZA alloys, the solidus temperature decreased and homologous temperature increased with increase in Zn and Al contents.

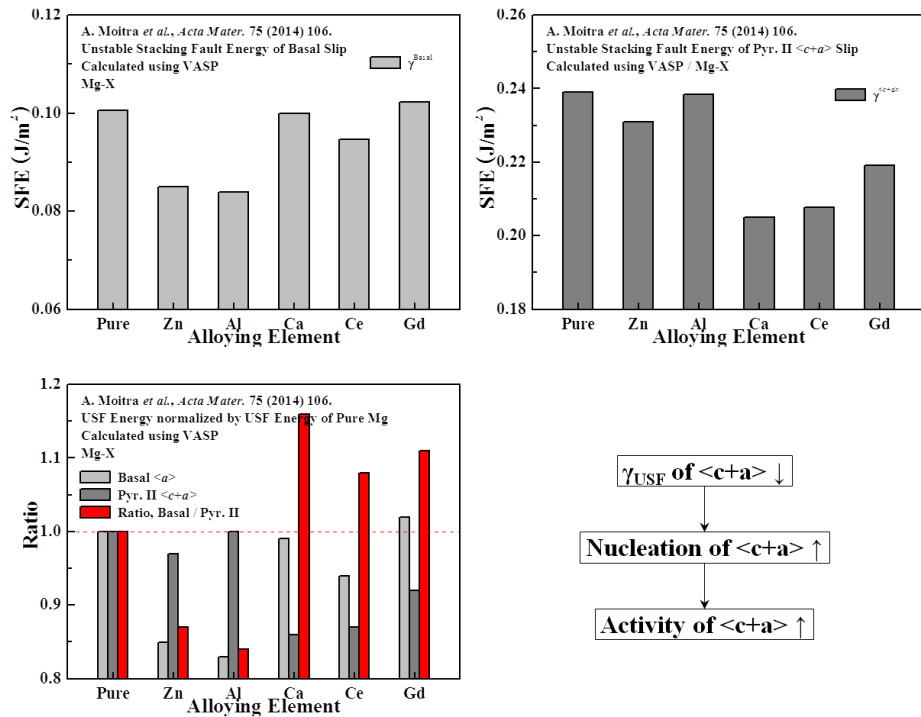


Figure 1.24 Theoretical effects of alloying element on SFE of pyramidal II $\langle c+a \rangle$; unstable SFE of basal $\langle a \rangle$ or pyramidal II $\langle c+a \rangle$ and their ratio [47].

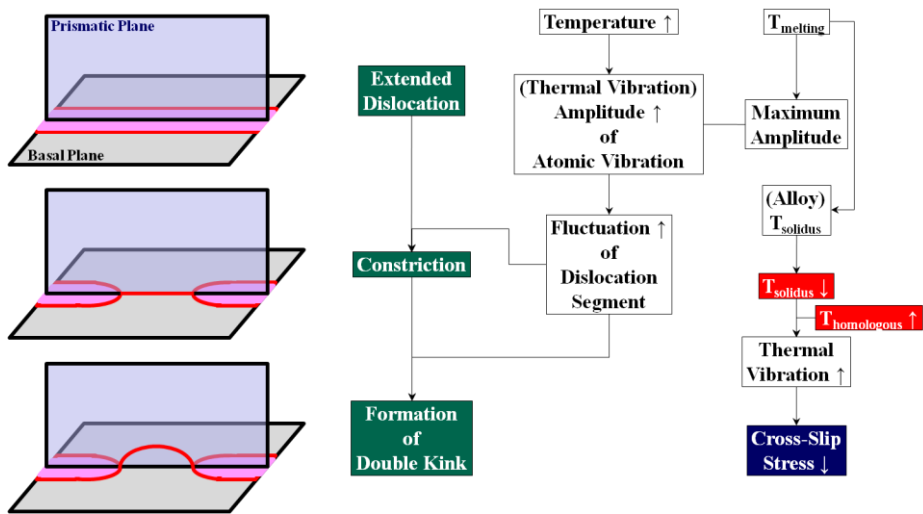


Figure 1.25 Thermal activation of cross-slip.

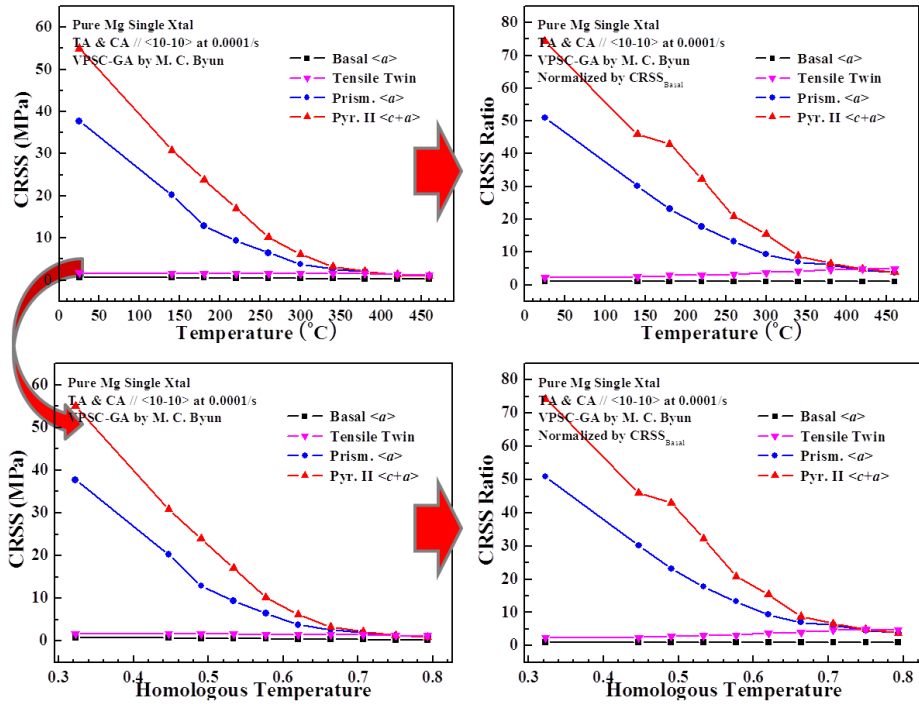


Figure 1.26 Temperature (homologous T) dependencies of CRSS (ratio) [50].

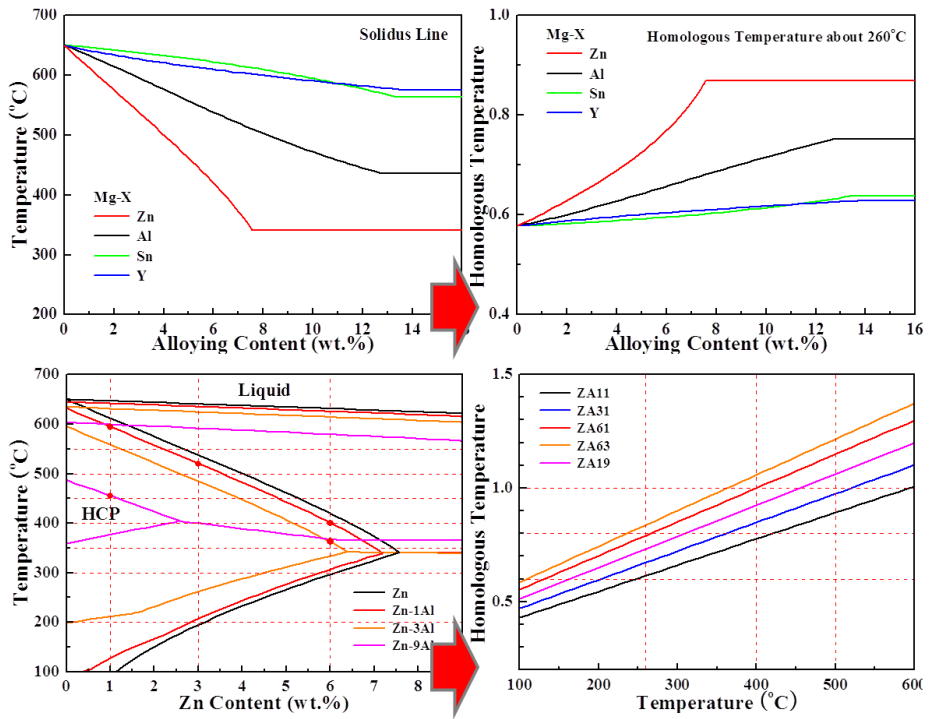


Figure 1.27 Effects of alloying elements on solidus (homologous) temperature; (1) Mg-X and (2) ZA alloys.

1.5.2 Increasing CRSS of basal slip

Figure 1.28 shows two examples which show the effects of increment or decrement on the theoretical CRSS ratio (non-basal to basal). Examples are represented as follows;

(Example 1) (Initial CRSSes of 20 (for non-basal) and 5 (for basal), Schmid factors of 0.35 and 0.10, CRSS increments of 0.2 for both) with increase in X (corresponding to alloying content), CRSS ratio decreases and critical stresses (stress necessary to activate specific slip mode) of basal and non-basal were reversed.

(Example 2) (Initial CRSSes of 20 (for non-basal) and 5 (for basal), Schmid factors of 0.35 and 0.10, CRSS increment of 0.1 for basal and decrements of 0.6, 0.4 or 0.1 for non-basal) with increase in X (corresponding to temperature), CRSS ratio decreases and critical stresses of basal and non-basal were reversed only in large decrement of 0.6 for non-basal.

Figure 1.29 shows the strengthening effects of alloying elements (Zn, Al, Ca and Y) on the theoretical CRSS (at 0K) of the basal slip [52] and athermal stress of the prismatic slip (calculated by J. A. Yasi *et al.*) [53]. The strengthening effects of Ca or Y were much larger than those of Zn or Al. Figure 1.12 shows the effects of alloying elements (Al and Y) on the theoretical CRSSes (at 0K) of the basal and prismatic and pyramidal II $\langle c+a \rangle$ slips (calculated by K. H. Kim *et al.*) [54]. The CRSS ratios (non-basal to basal) decreased with increase in Al or Y contents. And the amount of decrease was larger in Y than in Al.

Figure 1.30 shows the effects of Zn content on the CRSS of the basal slip (measured by A. Akhar *et al.*) [55] and athermal stress of prismatic slip (estimated by B. Raesisinia *et al.*) [56] at relatively high temperature. With in-

crease in Zn content, the CRSS ratio (prismatic to basal slip) decreased. Figure 1.31 shows the effects of Zn content and grain size on the CRSS of the basal and prismatic slip at room temperature [57]. With increase in Zn content or decrease in grain size, the CRSS ratio (prismatic to basal slip) decreased.

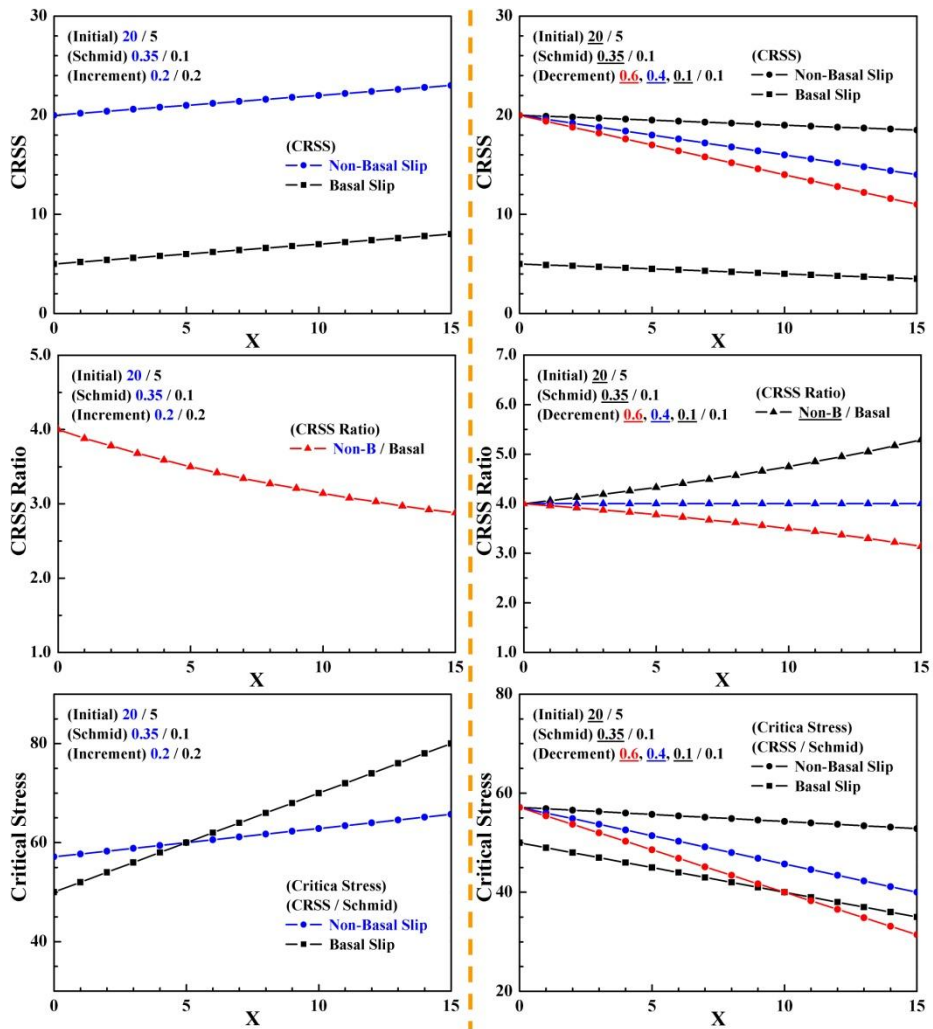


Figure 1.28 Effects of increment or decrement on theoretical CRSS ratio; (1) increment in both and (2) decrement in only non-basal slip.

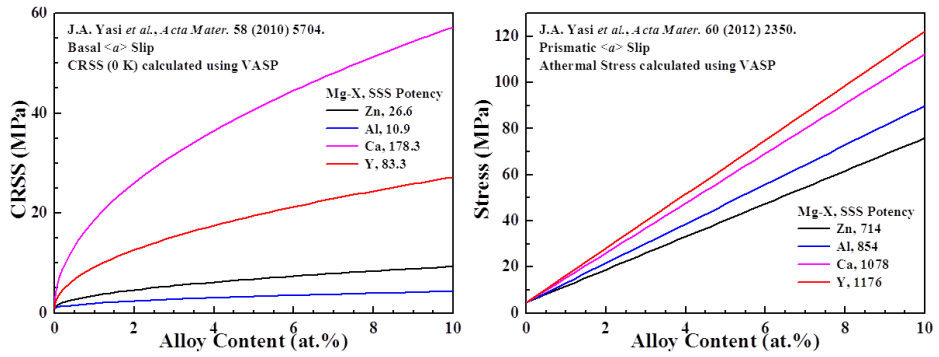


Figure 1.29 Effects of alloying elements (Zn, Al, Ca and Y) on theoretical CRSS; (1) basal slip [52] and (2) athermal stress of prismatic slip [53].

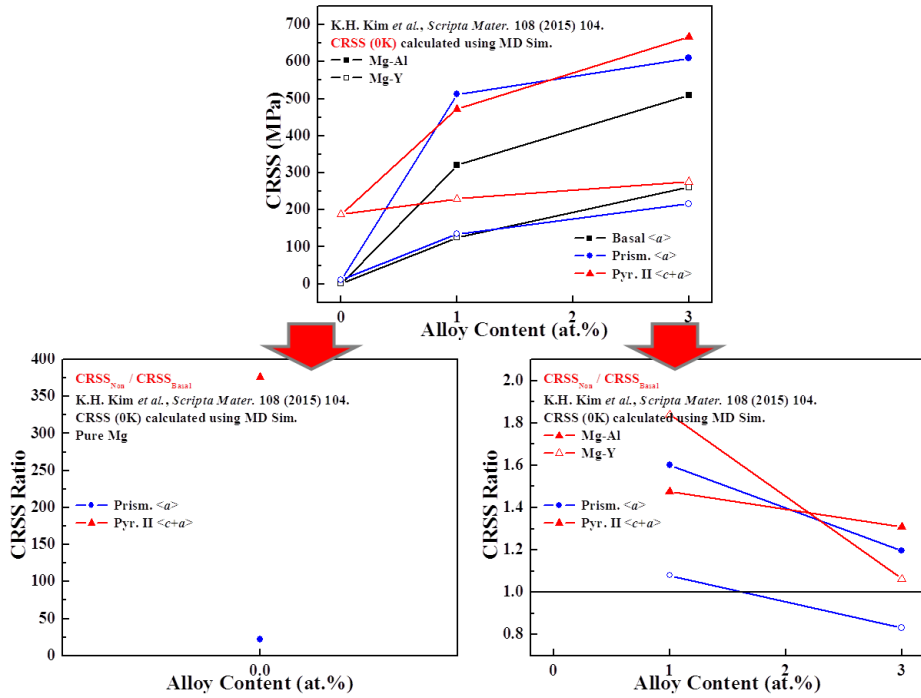


Figure 1.30 Effects of alloying elements (Al and Y) on theoretical CRSS (ratio) [54].

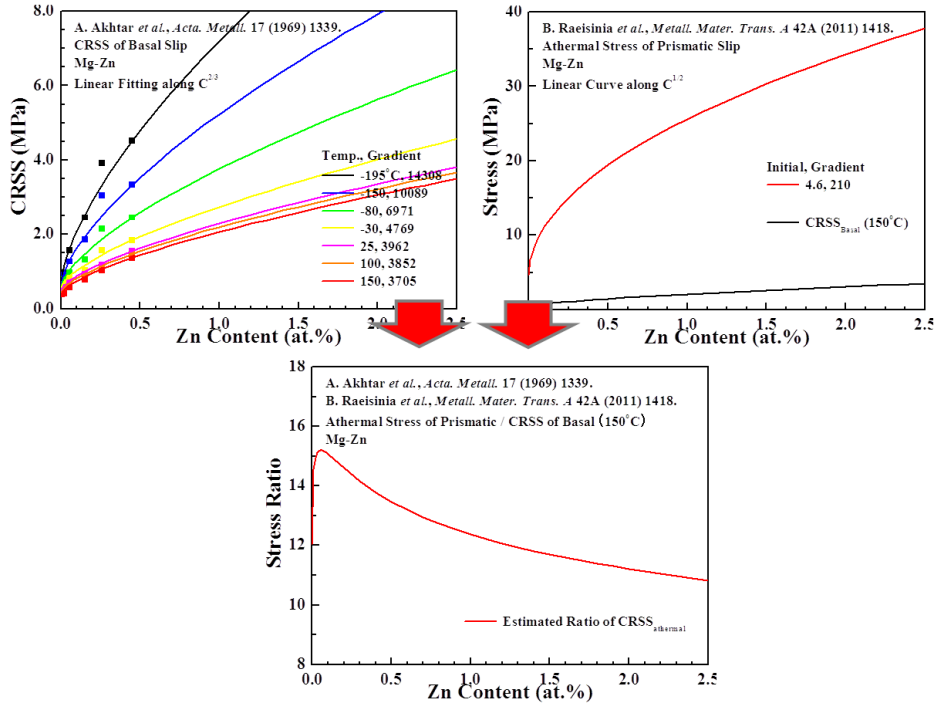


Figure 1.31 Effects of Zn content on CRSS ratio; (1) CRSS of basal slip [55], (2) athermal stress of prismatic slip [56] and (3) ratio.

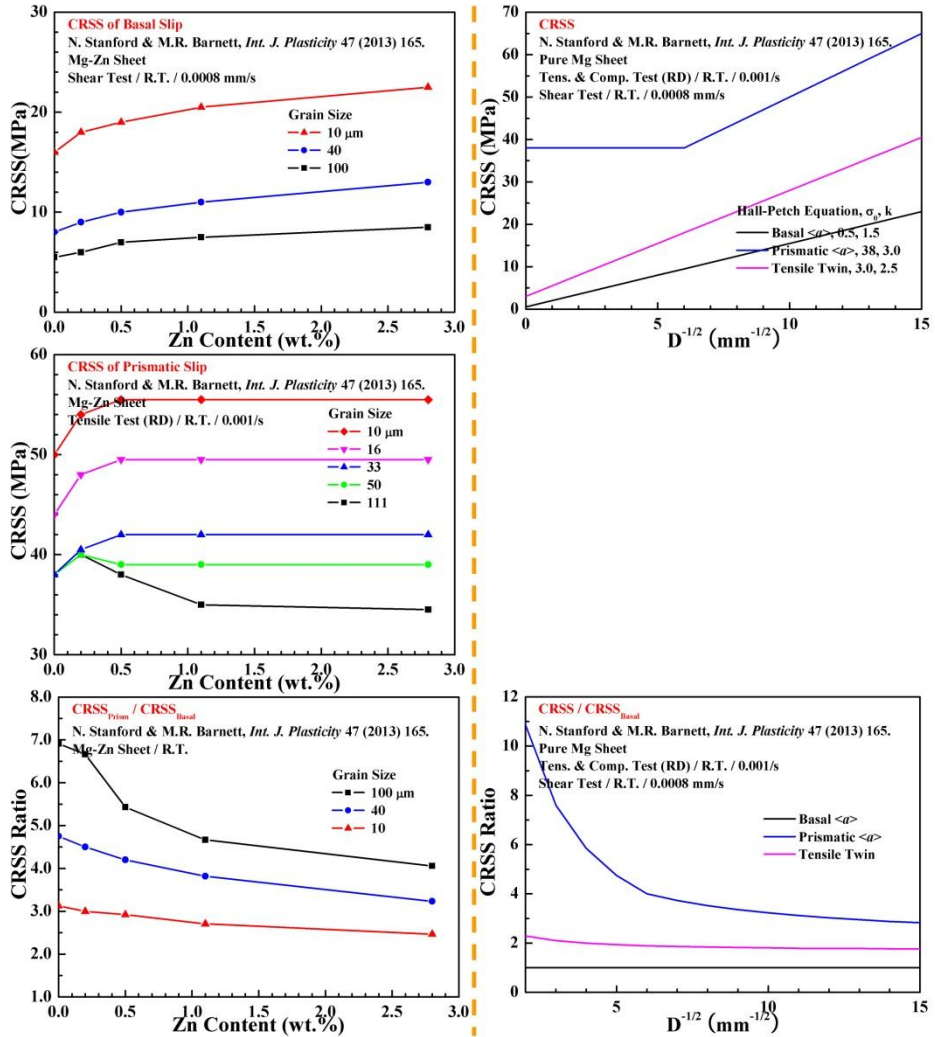


Figure 1.32 Effects of Zn content and grain size on CRSS ratio at room temperature; (1) CRSS of basal slip, (2) CRSS of prismatic slip and (3) ratio [57].

1.5.3 Grain-size dependant compatibility deformation

Figure 1.33 shows the compatibility deformation process as follows [58,59];

1. Two neighboring grains whose basal planes are tilted some degree from the loading direction are easy to deform by the basal slip.

2. When two neighboring grains deform by the basal slip freely, the interface between two grains can be broken.

3. To maintain the continuity, other deformation along c-axis is needed.

Compatibility stress is the one originated from the grain boundary bonding force to sustain the grain boundary continuity. By aid of this internal stress, hard slip modes (which has high CRSS) can be activated near the grain boundary. Because the compatibility stress decreases rapidly with increase in distance from the grain boundary, small grains are favorable to deform throughout the whole grain interior by the hard slip modes.

Figure 1.34 shows two cases which show the activation of the hard slip modes near grain boundaries. Cases are represented as follows;

(Case 1 - AZ31 alloy after tension) in large grain, non-basal slip was activated only near the grain boundary and basal slip was activated inside the grain. In small grain, pyramidal II $\langle c+a \rangle$ slip was activated inside the grain [58,60].

(Case 2 - Ti bi-crystal after compression) near the interface $\langle c+a \rangle$ slip was activated only near the interface [61].

Schematic drawing in Figure 1.34 shows the limited propagation of the dislocations nucleated at the grain boundary originated from the rapid decrease in compatibility stress with distance and difference in shear stress direction between near the grain boundary and inside the grain [62].

Change in DRX (dynamic recrystallization) behaviors with deformation

conditions shown in Figure 1.35 (compression of the stainless steel) can be summarized as follows [63-65];

1. With increase in Zener-Hollomon parameter (increase in strain rate or decrease in temperature), DRXed grain size decreased.
2. At high Z (low Temperature or high strain rate), NRX (replacement of parent grains by multi-layers of the small DRXed grains) occurred.
3. At low Z (high Temperature or low strain rate), ordinary DRX (replacement of parent grains by growth of small DRXed grains) occurred.
4. Therefore, compatibility deformation is favorable to occur throughout the entire grain in the deformation at high Z condition.

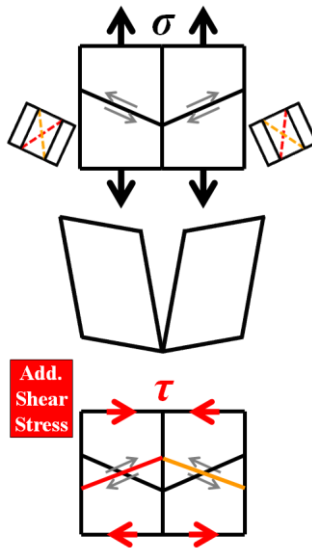


Figure 1.33 Schematic drawing on compatibility deformation [58].

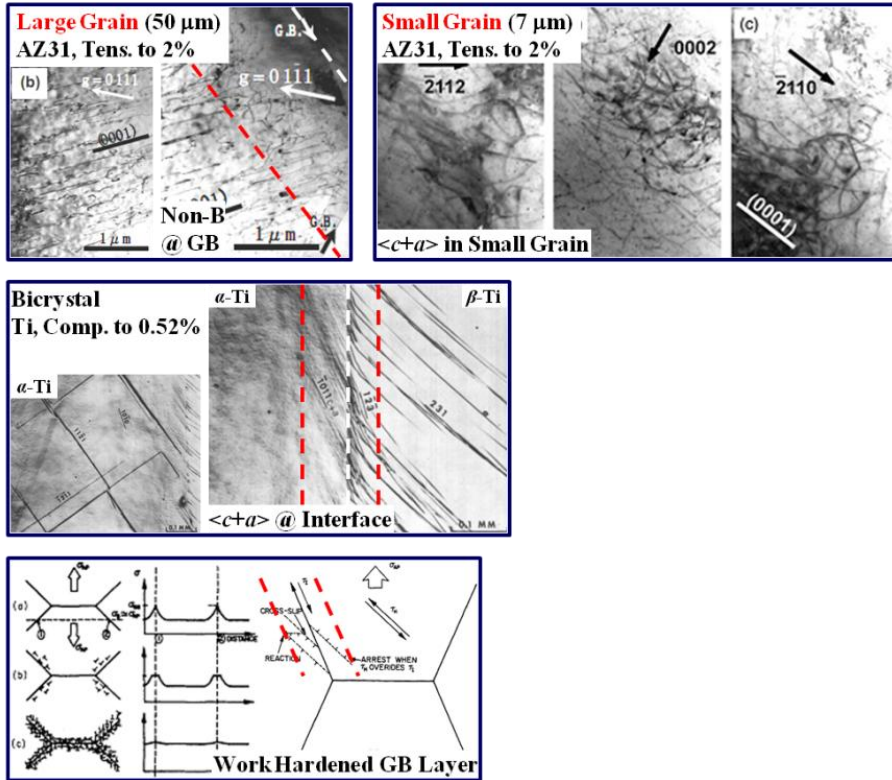
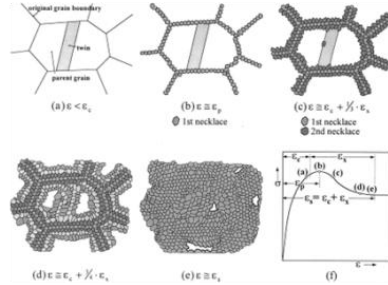
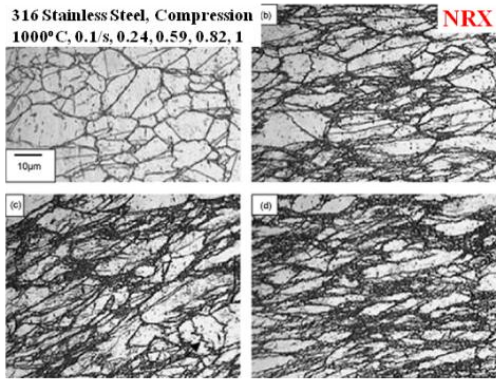


Figure 1.34 Activation of hard slip mode near grain boundary; (1) AZ31 alloy after tension [58,60], (2) Ti bicrystal after compression [61] and (3) schematic drawing on grain boundary hardening [62].



(NRX)
 (a) Parent Grain & Twin → With Increasing Strain, (b) 1st Necklace at Prior GB → (c) 2nd Necklace on Interface of 1st Layer & Parent Grain → (d, e) Expansion of Necklace.

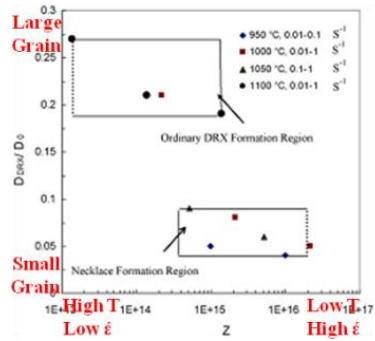
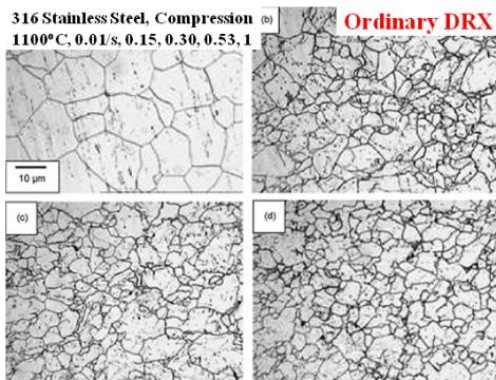


Figure 1.35 DRX behaviors with deformation condition; (1) NRX, (2) Ordinary DRX and (3) DRX mechanism map [63,64].

1.6 Summary on texture development mechanisms

1.6.1 Mechanisms for double peak basal texture

Possible mechanisms to develop the double peak basal texture were summarized in Figure 1.36 as follows;

1. Activation of the pyramidal II $\langle c+a \rangle$ slip at high temperature
2. Formation of the shear zone consisted of the rotational DRXed grains [22]
3. Formation of the shear band consisted of the compressive and double twin at low temperature and shear band nucleation at moderate temperature

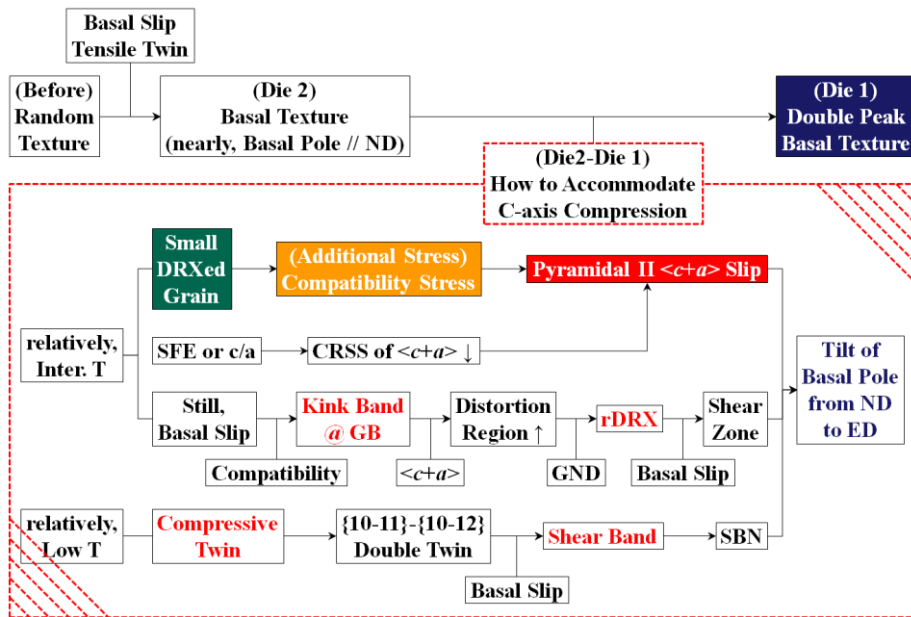


Figure 1.36 Summary on mechanisms for development of double peak basal texture.

1.6.2 Mechanisms for rare-earth texture

Possible mechanisms to develop the rare earth texture (weak basal texture) were summarized in Figure 1.37 as follows [66-69];

In precipitate state,

1. Preferred growth of the PSNed (particle stimulated nucleation) grains with random texture
2. Activation of the non-basal slip by aid of the compatibility stress caused by the grain refinement resulted from the growth retardation caused by Zener drag effect

In solid solution state,

1. Activation of the non-basal slip by aid of the compatibility stress caused by the grain refinement resulted from the growth retardation caused by solute drag effect originated from large atomic size
2. Reduction of the lattice resistance for the non-basal slip by reducing the c/a ratio
3. Activation of the non-basal slip by reducing the critical stress for the cross-slip resulted from the increase in SFE of the basal slip and decrease in SFE of the non-basal slip
4. Activation of the non-basal slip by increasing the number of stacking fault to act as nucleation site of the non-basal dislocation
5. Activation of the non-basal slip by reducing the CRSS ratio of non-basal to basal slip resulted from large solid solution strengthening effect on basal slip originated from large atomic size
6. Formation of large number of shear band consisted of the compressive and double twin and the preferred growth of the SBNed grains

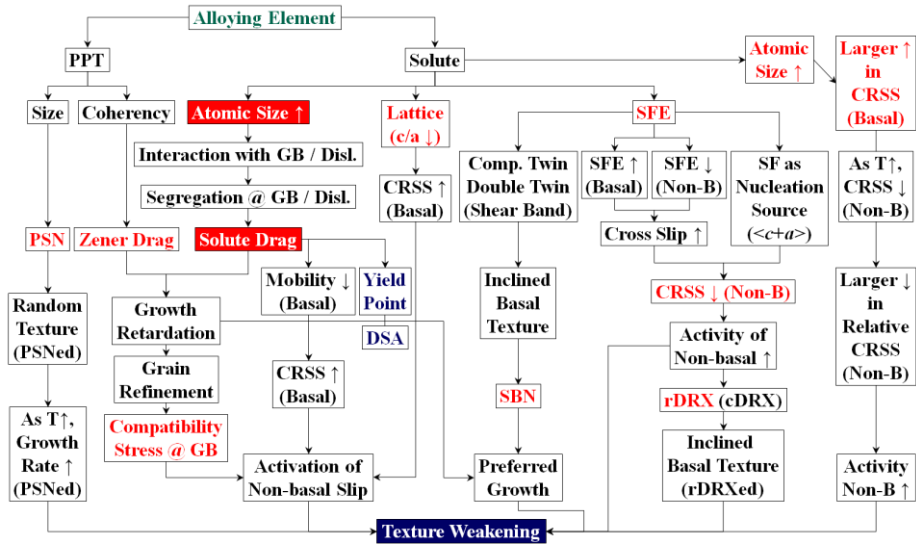


Figure 1.37 Summary on mechanisms for development of rare-earth texture.

Chapter 2 Experimental procedures

2.1 Fabrication of extruded plate

2.1.1 Extrusion process

Figure 2.1 shows the extrusion process. Mg-Zn-Al alloys were melted in a steel crucible with surface protect gas of $\text{CO}_2 + 0.5\% \text{SF}_6$. Zn and Al ingots were added to pure molten Mg at 700°C and small Mn flakes were added about 0.3wt.%. The ingots were homogenized at 400°C for 12 hrs. Extruded plates were manufactured with a shape of $30 \times 3\text{t}$ (mm^2) section or $15 \times 6\text{t}$ (mm^2) section as an extrusion ratio of 56:1 using the indirect extrusion press. After the extrusion process, extruded plates were air-cooled but remainders were quenched into cold water.

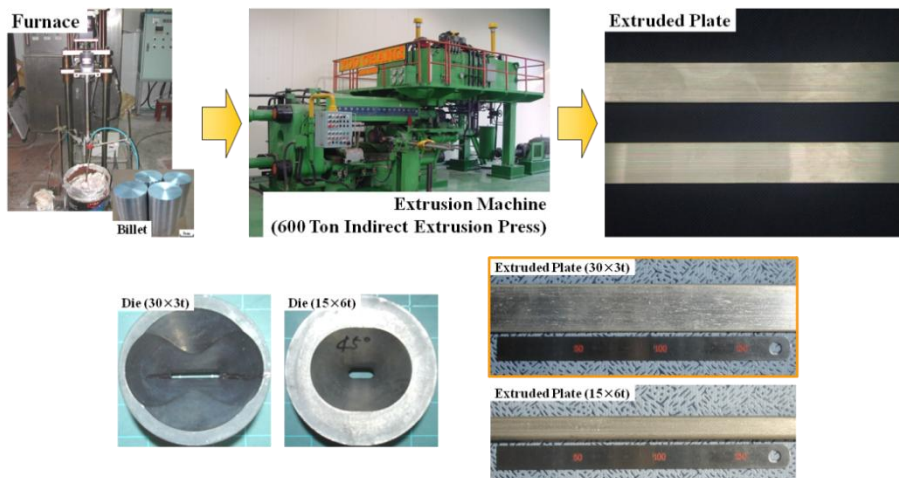


Figure 2.1 Extrusion process.

2.1.2 Alloy and extrusion condition

Extruded alloys and their extrusion conditions were summarized at Table 2.1 and Figure 2.3. The ZA alloys were extruded at 230 or 260°C. And the ZA11, ZA61 and ZA63 alloys were extruded at different temperatures. The Ca-containing ZA alloys were extruded mainly at 340°C. With increase in Zn and Al contents or addition of Ca, extrusion pressure increased. With increase in extrusion temperature, extrusion pressure decreased. At high extrusion temperature, extrusion speed was lowered because of extrusion defect. And also Ca-containing ZA alloys were extruded at low speed to adopt the similar speed for all of them.

Figure 2.2 represents the designation for them. Extrusions were mainly designated as ‘alloy name - extrusion temperature’. For 15×6t-sectional extrusion, ‘6t’ was denoted at the last part of extrusion name. For the extrusion remainder, ‘specimen position’ in the remainder was denoted at the last part of extrusion name.

ZA61-260
ZA61-260-6t
ZA61-260 (Air)

(Name of Specimen for Extruded Plate)

- ZA61-260 : (Section, 30×3t) Alloy-Extrusion Temperature
 - ZA61-260-6t : (Section, 15×6t) Alloy-Extrusion Temperature-Thickness
 - ZA61-260 (Air) : Alloy-Extrusion Temperature (Specimen Position in Remainder)
-

Figure 2.2 Designation for specimen of extruded plate.

Table 2.1 Extruded alloys (extrusion name) and their extrusion conditions.

Extrusion Name	Nominal Composition (wt.%)	Extrusion Temp. (°C)	Extrusion Speed (cm/min.)	Extrusion Pressure (kgf/cm²)
ZA11-230	Mg-1Zn-1Al-0.3Mn	230	160	90
ZA13-230	Mg-1Zn-3Al-0.3Mn	230	-	120
ZA31-230	Mg-3Zn-1Al-0.3Mn	230	160	110
ZA33-230	Mg-3Zn-3Al-0.3Mn	230	-	120
ZA11-260	Mg-1Zn-1Al-0.3Mn	260	80	130
ZA13-260	Mg-1Zn-3Al-0.3Mn	260	80	150
ZA19-260	Mg-1Zn-9Al-0.3Mn	260	80	145
ZA31-260	Mg-3Zn-1Al-0.3Mn	260	80	140
ZA61-260	Mg-6Zn-1Al-0.3Mn	260	80	140
ZA11-260-6t	Mg-1Zn-1Al-0.3Mn	260	80	130
ZA13-260-6t	Mg-1Zn-3Al-0.3Mn	260	80	135
ZA31-260-6t	Mg-3Zn-1Al-0.3Mn	260	80	130
ZA61-260-6t	Mg-6Zn-1Al-0.3Mn	260	80	130

Table 2.1 Continued.

Extrusion Name	Nominal Composition (wt.%)	Extrusion Temp. (°C)	Extrusion Speed (cm/min.)	Extrusion Pressure (kgf/cm²)
ZA11-260	Mg-1Zn-1Al-0.3Mn	260	80	130
ZA11-400	Mg-1Zn-1Al-0.3Mn	400	50	60
ZA11-450	Mg-1Zn-1Al-0.3Mn	450	21	79
ZA61-260	Mg-6Zn-1Al-0.3Mn	260	80	130
ZA61-300	Mg-6Zn-1Al-0.3Mn	300	-	115
ZA61-340	Mg-6Zn-1Al-0.3Mn	340	-	75
ZA61-400	Mg-6Zn-1Al-0.3Mn	400	5	65
ZA63-260	Mg-6Zn-3Al-0.3Mn	260	80	145
ZA63-300	Mg-6Zn-3Al-0.3Mn	300	-	120
ZA63-340	Mg-6Zn-3Al-0.3Mn	340	-	75
ZA63-400	Mg-6Zn-3Al-0.3Mn	400	2.3	55

Table 2.1 Continued.

Extrusion Name	Chemical Composition (wt.%)	Extrusion Temp. (°C)	Extrusion Speed (cm/min.)	Extrusion Pressure (kgf/cm ²)
Pure-450	Mg	450	38	54
Ce0.2-450	Mg-0.26Ce	450	11	89
Z1Ce0.2-400	Mg-1Zn-0.2Ce	400	100	110
ZA61Ce2-340	Mg-5.9Zn-0.9Al-2.4Ce	340	6.4	115
Ca0.6-450	Mg-0.75Ca	450	56	88
Z1Ca0.2-340	Mg-0.9Zn-0.2Ca	340	-	145
Z1Ca0.4-340	Mg-0.9Zn-0.4Ca	340	-	150
ZA11Ca1-340	Mg-0.9Zn-1.1Al-1.2Ca	340	17	157
Z6Ca0.2-340	Mg-6.0Zn-0.1Ca	340	8.2	99
Z6Ca1-340	Mg-5.9Zn-1.1Ca	340	8.7	110
ZA61Ca0.2-340	Mg-5.9Zn-1.0Al-0.1Ca	340	11	70
ZA61Ca1-260	Mg-6.3Zn-1.0Al-1.1Ca	260	4.4	164
ZA61Ca1-340	Mg-6.0Zn-1.0Al-1.1Ca	340	3.3	103
ZA61Ca1-400	Mg-6.3Zn-1.0Al-1.1Ca	400	13	84
ZA61Ca2-340	Mg-6.2Zn-0.9Al-2.0Ca	340	7.6	151
ZA63Ca1-340	Mg-6.3Zn-2.7Al-1.0Ca	340	17	104

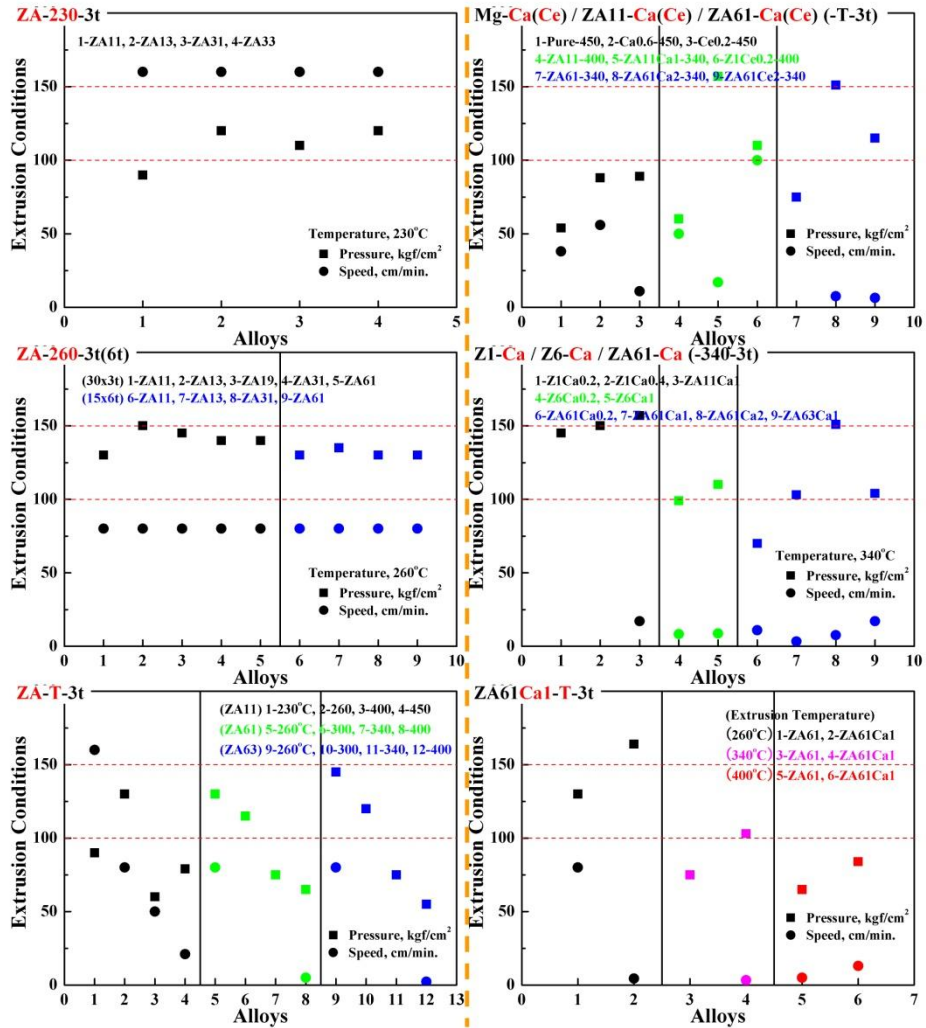


Figure 2.3 Extrusion conditions (extrusion pressure and speed).

2.2 Plane strain compression test

2.2.1 Plane strain compression process

Figure 2.4 shows the plane strain compression process. Cube specimens ($6\times 6\times 6\text{ mm}^3$) were fabricated from the $15\times 6\text{t}$ sectional extruded plates and cast billets. Surfaces of the cube specimen and PSC jig were coated by BN powder. Two kinds of PSC jigs were used. Mainly used one was rectangular shape and the other one was diamond shape (designated as EX) used for imposing the constriction strain through the transverse direction. The specimen and PSC jig were heated at the objective temperature for 30 min. before high-temperature PSC tests.

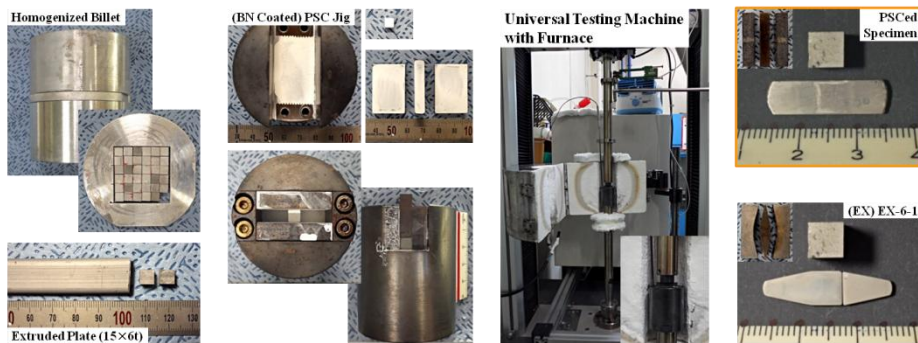


Figure 2.4 Plane strain compression process.

2.2.2 Alloy and plane strain compression condition

15×6t sectional extruded ZA11, ZA31, ZA61 and cast ZA63, ZA19, ZA31, ZA61, ZA61Ca1 alloys were used for PSC tests. And the 15×6t sectional extruded ZA61 alloys annealed at 300 or 450°C for 5 hrs (designated as a300 or a450) were also used for PSC tests.

Three kinds of PSC tests were conducted. Main one was two-step PSC test (designated as two-step PSC) consisted of room-temperature PSC as a first step and high-temperature PSC as a second step. As a first step, cube specimen was PSCed to a true strain of 0.1 (0.12 for cast alloys) at room temperature with an initial strain rate of 0.0002/sec. And as a second step, the room-temperature PSCed specimens were PSCed to a true strain of 1.0 at various temperatures (200 ~ 550°C) and initial strain rates (0.0002 ~ 0.8000/sec) using the same PSC-specimen-loading coordinate system. Two kinds of PSC-specimen-loading coordinate systems were used for the 15×6t sectional extruded alloys. One is the two-step PSC (CA // TD) where each compression axis (CA), longitudinal direction (LD) and constraint direction (CD) in the PSC-specimen-loading coordinate system was parallel to the transverse direction (TD), normal direction (ND) and extrusion direction (ED), respectively. The other one is the two-step PSC (CA // ED) where each compression axis (CA), longitudinal direction (LD) and constraint direction (CD) in the PSC-specimen-loading coordinate system was parallel to the extrusion direction (ED), normal direction (ND) and transverse direction (TD), respectively. Each Figure 2.6 and 2.7 show the flow stresses of the extruded and cast alloys during the two-step PSC tests, respectively.

Another one was the two-step PSC test with specimen rotation (designated as two-step PSC (ROT)) and two-step PSC (ROT) tests were conducted us-

ing cast ZA63, ZA61, ZA19 and ZA31 alloys. As a first step, cube specimen was PSCed to a true strain of 0.07 at room temperature with an initial strain rate of 0.0002/sec. Before a second step, the room-temperature PSCed specimen was rotated 90° on the rotation axis of CD (CA in first step PSC became LD in second step). Then as a second step, the 90°-rotated room-temperature PSCed specimens were PSCed to a true strain of 1.0 at various temperatures (300 ~ 450°C) with an initial strain rate of 0.0002/sec.

The other one was general PSC test (designated as one-step PSC) and one-step PSC tests were conducted to a true strain of 1.0 at various temperatures (340 ~ 450°C) and initial strain rates (0.0002 ~ 0.4000/sec) using the cast ZA63 alloys. And additional one-step PSC tests were conducted at 400°C with 0.4000/sec using the cast ZA61 and ZA19 alloys. The PSCed specimens were quenched in cold water right after the high-temperature PSC. Designation for the PSCed specimens was shown in Figure 2.5.

ZA63-RT/0.12-450/0.4/1.0
ZA61-260-6t-TD/ND-RT/0.1-260/0.04/1.0
ZA63-RT/0.07-ROT-EX-300/1.0

- ZA63 : (Cast Billet) Alloy
 - ZA61-260-6t: (Extruded Plate) Alloy-Extrusion Temperature-Thickness (Section, 15×6t)
 - TD/ND : (PSC Coordinate System) Compression Axis (CA) / Longitudinal Direction (LD)
 - RT/0.12 : (PSC 1st Step) 20°C / (Initial Strain Rate) 0.0002/sec / Plastic Strain (Compression Axis)
 - 450/1.0 : (PSC 2nd Step) Temperature / (Initial Strain Rate) 0.0002/sec / Plastic Strain
 - 260/0.04/1.0: (PSC 2nd Step) Temperature / Initial Strain Rate (/second) / Plastic Strain
 - ROT : 90° Rotation of Specimen on CD Axis after PSC 1st Step
 - EX : PSC Die Type
-

Figure 2.5 Designation for PSCed specimen.

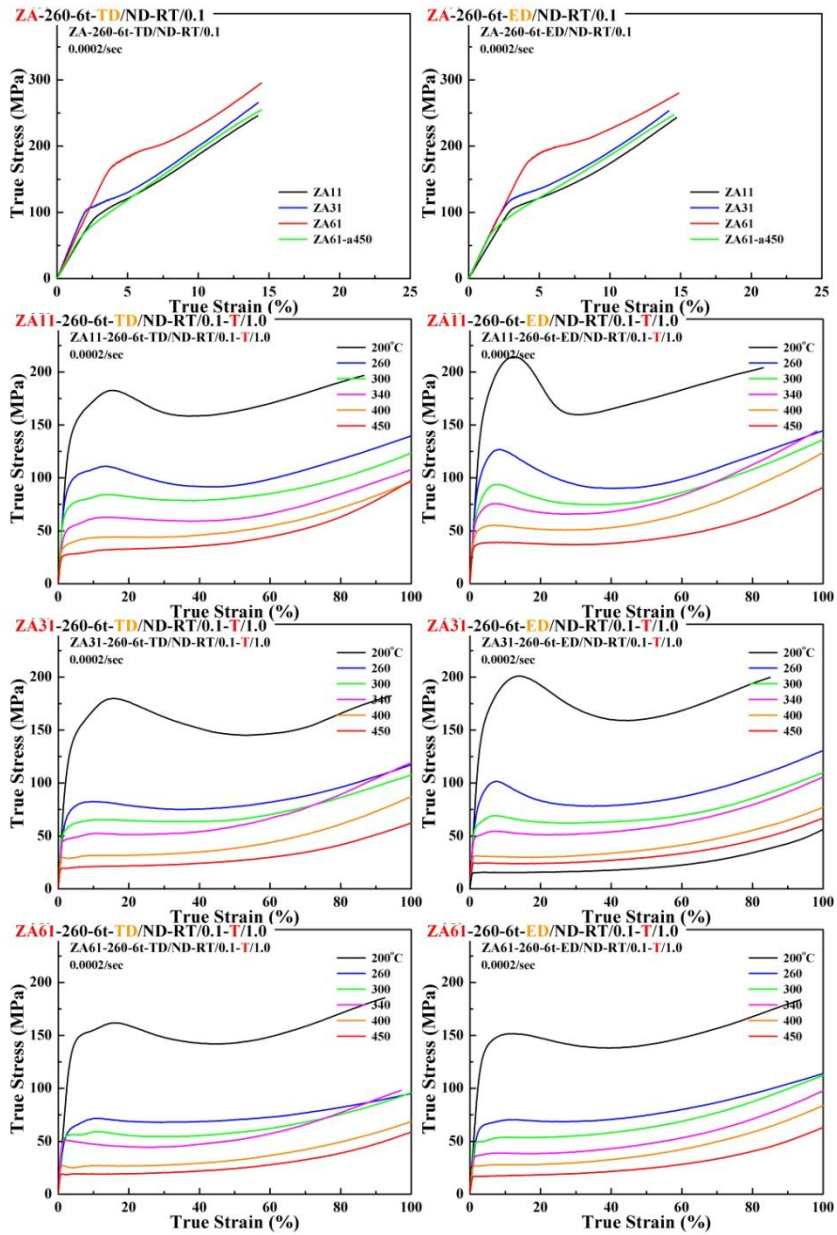


Figure 2.6 Flow stress during two-step PSC of extruded plate; (1) first step PSC and (2) second step PSC.

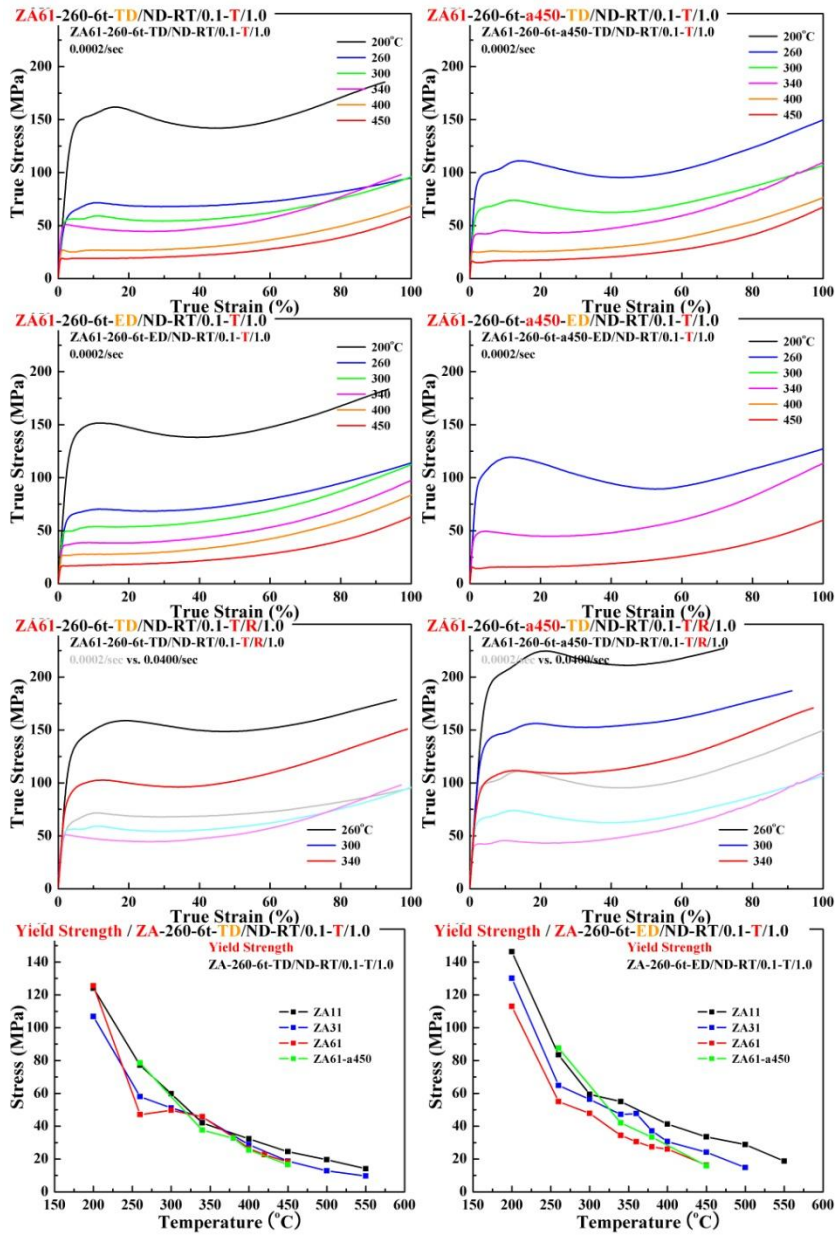


Figure 2.6 Continued.

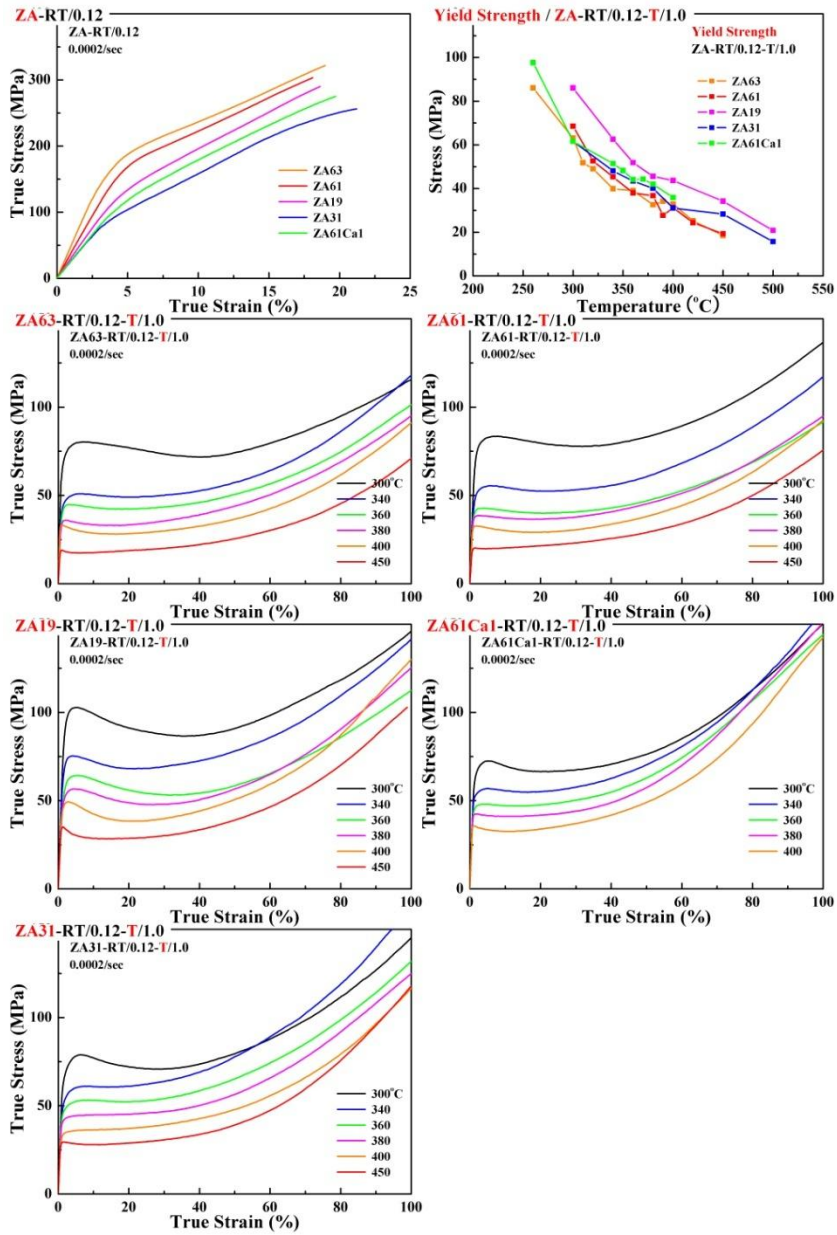


Figure 2.7 Flow stress during two-step PSC of cast specimen; (1) first step PSC and (2) second step PSC.

2.3 Characterization of microstructure and texture

2.3.1 Microstructure

Microstructure specimens of the ZA alloys extruded or PSCed were cut along the half thickness plane normal to the ND in the extruded plate or CA in the PSCed specimen. They were polished on sandpapers and then fine-polished with 0.3 and 0.05 μm alumina powder. To identify the grain boundaries optically, these specimens were etched with acetic-picral etchant (10 ml acetic acid + 4.2 g picric acid + 10 ml distilled water + 70 ml ethanol (95%)). Average grain size was measured by line intercept method.

2.3.2 Texture

Texture specimens of the ZA alloys extruded or PSCed were cut along the half thickness plane normal to the ND in extruded plate or CA in the PSCed specimen. They were mechanically polished with sandpapers and then fine-polished with 0.3 and 0.05 μm alumina powders. The {0002}, {10-10}, {10-11}, {11-20} pole figures were measured on this half thickness-plane using X'pert PRO MRD (x-ray diffractometer system). Background correction, defocusing correction and complete pole figure calculation were conducted using LaboTex 3 software.

Figure 2.8 represents the configurations of the microstructures and pole figures for extruded plates and PSCed specimens used in this dissertation. And Figure 2.9 represents the designation of the texture components in extruded plates and PSCed specimens used in this dissertation.

To reveal the texture development process, remainders of the 30×3t sectional extruded plates were examined using specimens extracted from them at the positions shown in Figure 2.10. Remainders were quenched at cold water right after the extrusion but the extruded plates were air-cooled.

Micro-texture was measured using SU 70 (FE-SEM) equipped with EBSD camera. OIM (orientation image microscopy) analysis was conducted using TSL OIM Analysis 4 software.

Theoretical deformation textures were calculated using VPSC 7 (Viscoplastic Self-consistent) software developed by LANL. Four deformation modes were adopted as basal $\langle a \rangle$, prismatic $\langle a \rangle$, pyramidal II $\langle c+a \rangle$ slip and {10-12} twin. To observe the change in theoretical deformation texture with relative activity of each deformation mode, only initial CRSS ratios were varied without strain hardening. Boundary condition was adopted as plane strain compression condition.

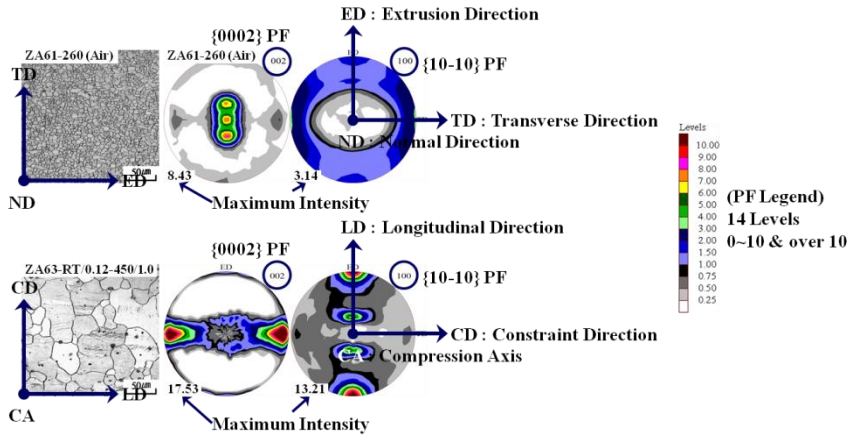


Figure 2.8 Configurations of microstructures and pole figures for extruded plates and PSCed specimens.

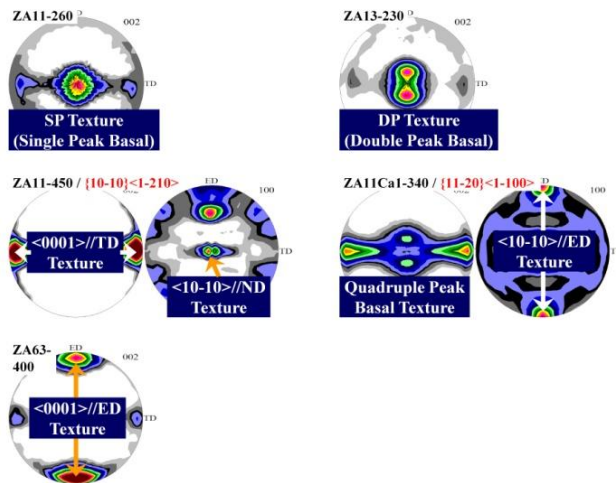


Figure 2.9 Designation of texture components in extruded plates and PSCed specimens; (1) SP texture, (2) DP texture, (3) TD (CD) texture and (4) ED (LD) texture.

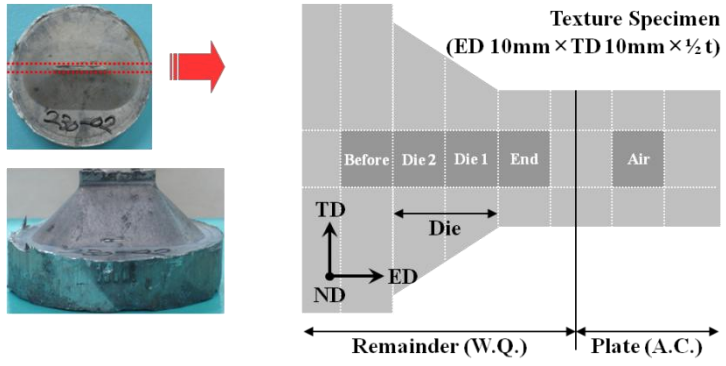


Figure 2.10 Texture specimens for extrusion remainder.

Chapter 3 Results

3.1 Effects of Zn and Al on double peak basal textures

Microstructures and textures of the ZA alloys extruded at 230 or 260°C are represented in Figure 3.1 and their basal pole intensity distributions were compared in Figure 3.5 as follows;

1. With increase in Zn and Al contents, spread of the basal poles toward the ED (ED spread) and tilt angle corresponding to the peak in the DP (double peak basal) texture increased as 15° for the ZA11-230 (ZA11 alloy extruded at 230°C with 30×3t section), 20° for the ZA13-230, 20° for the ZA31-230, 25° for the ZA33-230 and 0° for the ZA11-260, 20° for the ZA13-260, 25° for the ZA19-260, 20° for the ZA31-260, 30° for the ZA61-260, 30° for the ZA81-260 and 0° for the ZA11-260-6t (ZA11 alloy extruded at 260°C with 15×6t section), 20° for the ZA13-260-6t, 20° for the ZA31-260-6t, 25° for the ZA61-260-6t alloy. Instead of that, spread of the basal poles toward the TD (TD spread) in basal texture decreased with increase in Zn and Al contents. Especially in 15×6t-sectional extrusions, intensity of TD texture ($\langle 0001 \rangle // \text{TD}$) decreased with increase in Zn and Al contents.

2. With increase in Zn and Al contents, grain size decreased as 23 μm for the ZA11-230, 9 μm for the ZA13-230, 8 μm for the ZA31-230, 8 μm for the ZA33-230 and 30 μm for the ZA11-260, 9 μm for the ZA13-260, 7 μm for the ZA19-260, 9 μm for the ZA31-260, 5 μm for the ZA61-260, 4 μm for the ZA81-260 and 43 μm for the ZA11-260-6t (ZA11 alloy extruded at

260°C with 15×6t section), 9 μm for the ZA13-260-6t, 9 μm for the ZA31-260-6t, 4 μm for the ZA61-260-6t alloy.

3. ED spread and tilt angle corresponding to the peak in the DP texture increased with decrease in grain size.

4. Addition of Zn was more effective to increase the ED spread and decrease the grain size than addition of Al.

Microstructure and texture evolutions of the ZA alloys during the extrusions at 230 or 260°C are represented in Figure 3.2 and their basal pole intensity distributions were compared in Figure 3.5 as follows;

1. At the initial stage (before - die 2) where the massive fine DRXed grains were nucleated, broad SP texture was developed. Even though the DRXed grains might have broader texture distributions, their textures rotated back to the basal textures by the continuing deformation. Then the SP was split into the DP during the continuing extrusion process.

2. Even in SP texture developed initially, ED spread increased with increase in Zn and Al contents.

3. During grain growth air-cooling, SP strengthened and DP weakened. Especially in the ZA11-260, the DP was disappeared and changed into the SP during the severe grain growth.

4. As shown in Figure 3.3, during grain growth annealing, SP component ($\langle 0001 \rangle // ND$) strengthened. This phenomenon might be related to the difference in stored energy between DP and SP grains. Because DP grains might experience additional deformation accommodated by the $\langle c+a \rangle$ slip after one by the basal slip, they might have higher stored energy than SP grains. Therefore, during the SRX, the SP grains with lower stored energy might consume the DP grains with higher stored energy.

5. As shown in Figure 3.4, SP can split into DP by activation of the pyramidal II $\langle c+a \rangle$ slip. Moreover, tilt angle corresponding to the peak in DP texture can increase with increase in activity of the pyramidal II $\langle c+a \rangle$ slip.

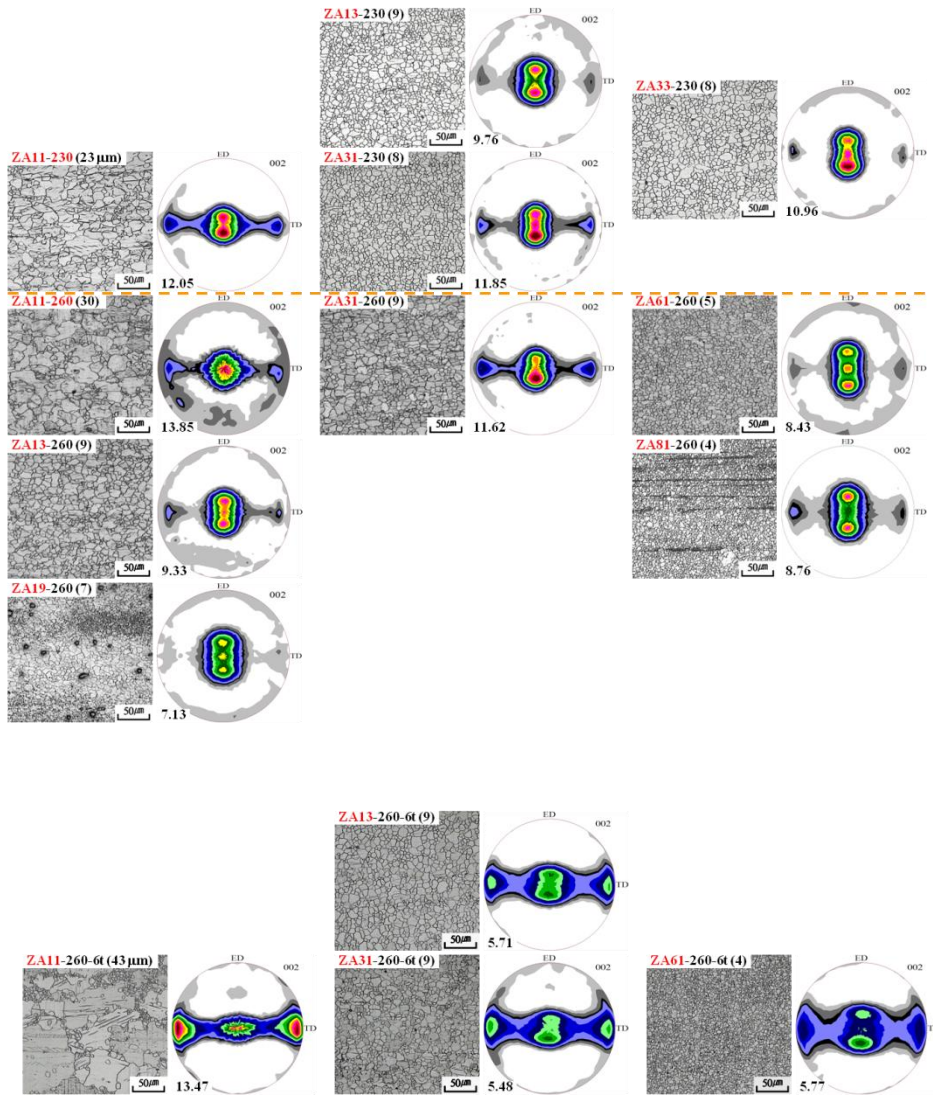


Figure 3.1 Microstructures and textures of ZA alloys extruded at 230 or 260°C; (1) 30×3t-sectional and (2) 15×6t-sectional extrusions.

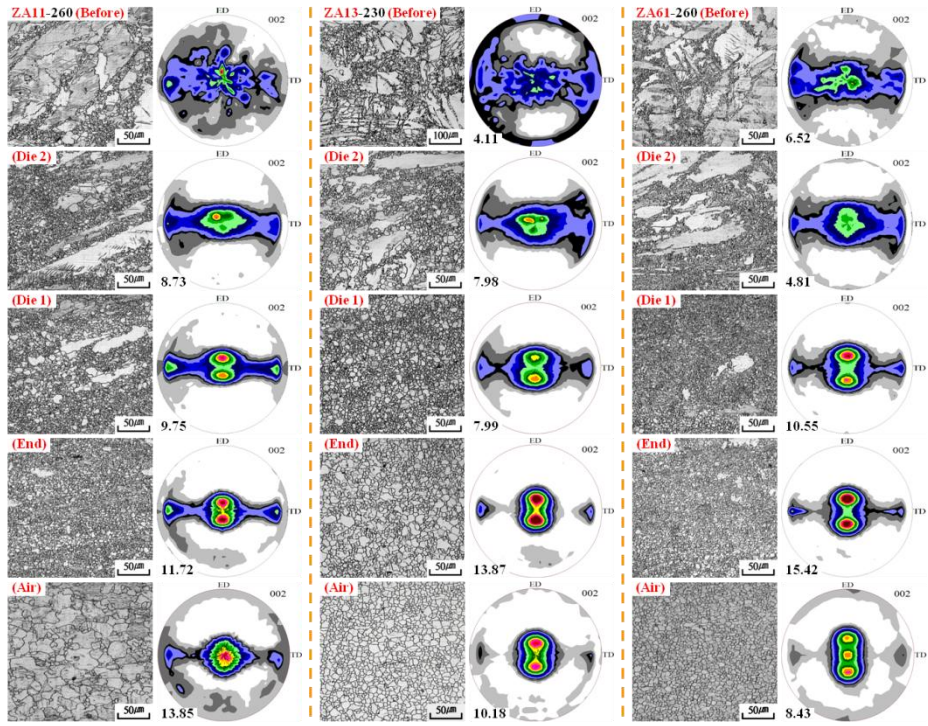


Figure 3.2 Microstructure and texture evolutions of ZA alloys during extrusions at 230 or 260°C; (1) ZA11-260, (2) ZA13-230 and (3) ZA61-260.

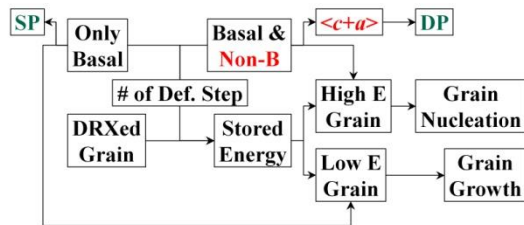
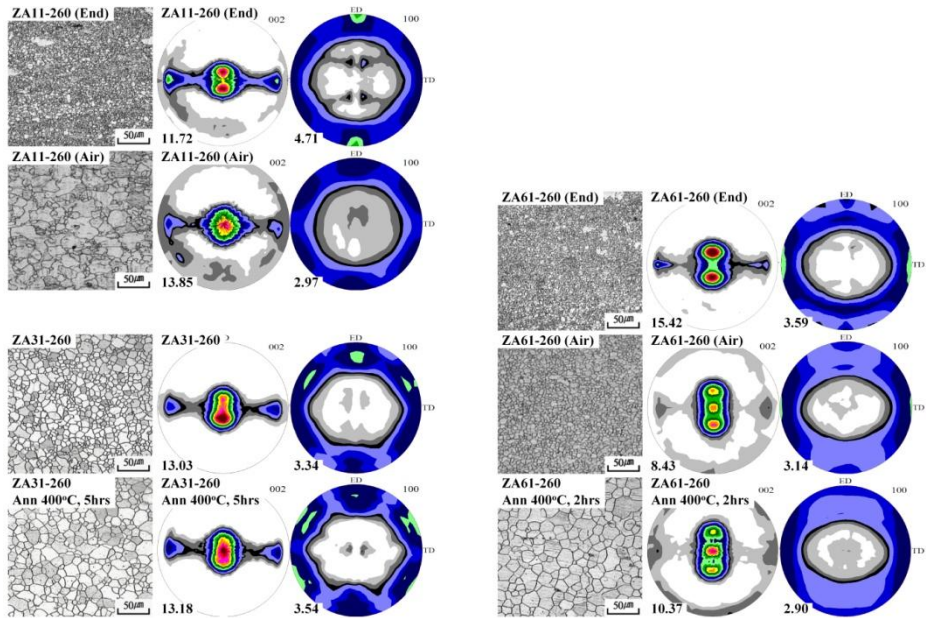


Figure 3.3 SRX textures of extruded ZAx1 alloys after air-cooling or annealing at 400°C.

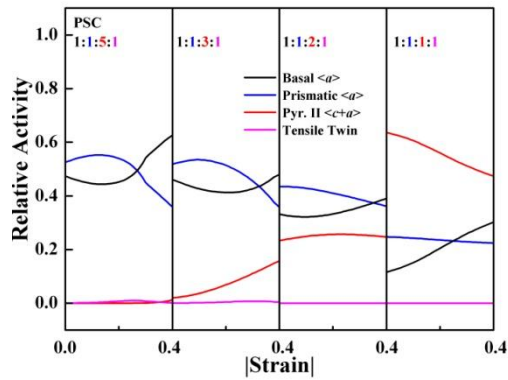
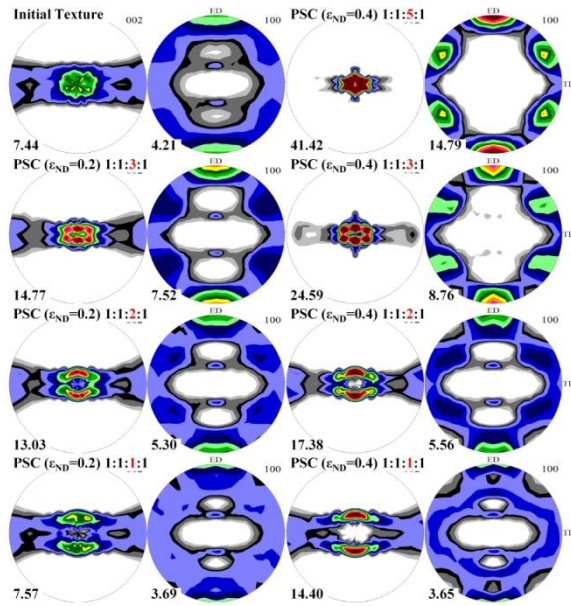


Figure 3.4 Theoretical deformation textures developed during PSC with different CRSS ratio; (initial texture) SP texture, (1) 1:1:5:1, (2) 1:1:3:1, (3) 1:1:2:1 and (4) 1:1:1:1.

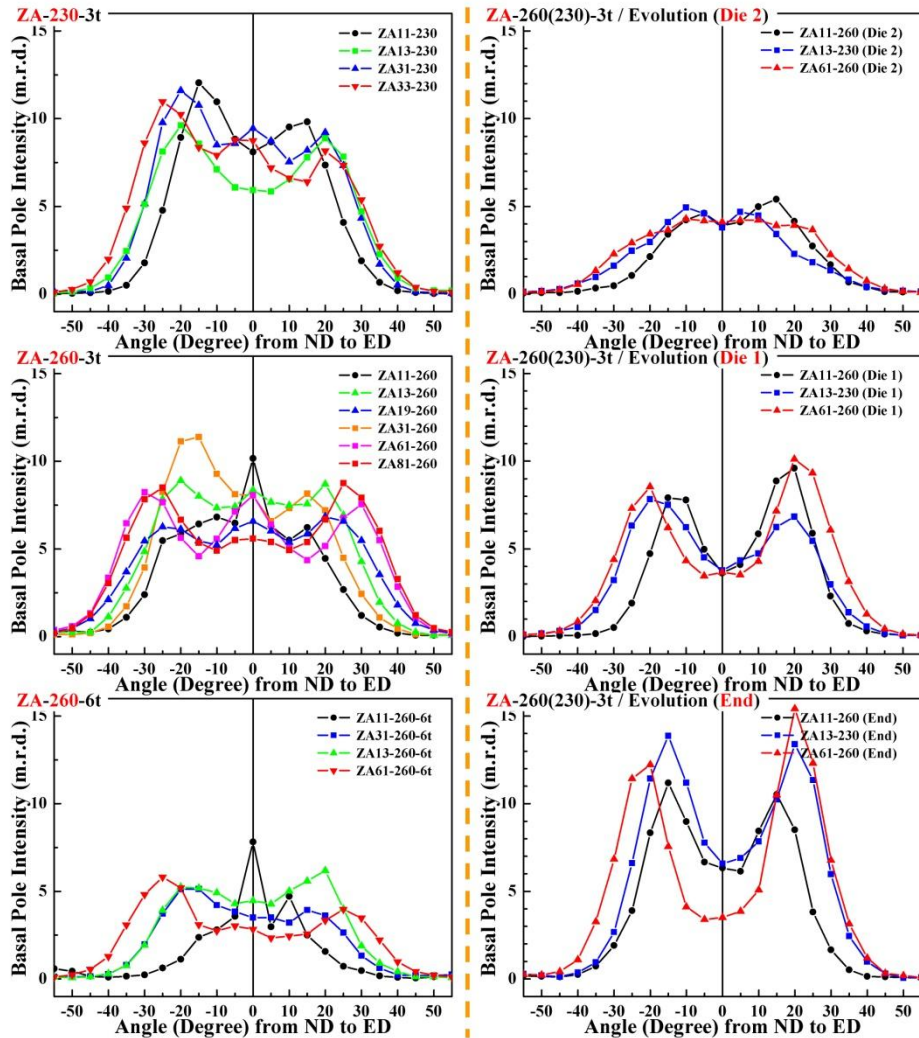


Figure 3.5 Distributions of basal pole intensities (with tilt angle from ND to ED) of ZA alloys extruded at 230 or 260°C.

3.2 Effects of extrusion temperature on textures

Microstructures and textures of the ZA alloys extruded at different temperatures are represented in Figure 3.6 and their basal pole intensity distributions were compared in Figure 3.14 as follows;

1. In the all ZA alloys, with increase in extrusion temperature, SP texture was developed and ED spread decreased.

2. In the all ZA alloys, with increase in extrusion temperature, grain size increased. Especially in the ZA11 alloys, severe grain growth was occurred even at 260°C.

3. In the ZA11 alloys, TD texture ($\langle 0001 \rangle // \text{TD}$ texture) strengthened with increase in temperature. Additionally, the $\langle 10\text{-}10 \rangle // \text{ND}$ texture also strengthened with increase in temperature.

4. In the ZA61 and ZA63 alloys, ED texture ($\langle 0001 \rangle // \text{ED}$ texture) was developed at high temperature and strengthened with increase in temperature. Moreover, the intensity of ED texture increased with increase in Al content.

Microstructure and texture evolutions of ZA alloys (ZA11, ZA61, ZA63) during the extrusions at different temperatures are represented in Figure 3.7 (ZA11), 3.9 (ZA61) and 3.10 (ZA63) as follows;

1. (ZA11-400) initially, $\{11\text{-}20\} \langle 1\text{-}100 \rangle$ texture with SP texture were developed. In contrast with the ZA11-260 whose SP split into DP with massive NRX, the SP was sustained with growth of the DRXed grains. However, in the ZA11-260-6t, similar with the ZA11-260, SP split into DP with massive NRX. Then the $\{11\text{-}20\} \langle 1\text{-}100 \rangle$ texture weakened and the $\{10\text{-}10\} \langle 1\text{-}210 \rangle$ texture strengthened during severe grain growth in the ZA11-400 and ZA11-260-6t.

2. As shown in Figure 3.8, during grain growth annealing, the $\{10-10\}\langle 1-210\rangle$ texture strengthened by faster growth of the $\{10-10\}\langle 1-210\rangle$ grains. This phenomenon might be related to the difference in stored energy between the $\{11-20\}\langle 1-100\rangle$ and $\{10-10\}\langle 1-210\rangle$ grains. Because the $\{11-20\}\langle 1-100\rangle$ grains might experience additional deformation accommodated by the prismatic $\langle a\rangle$ slip after one by the basal slip, they might have higher stored energy than $\{10-10\}\langle 1-210\rangle$ grains. Therefore, during the SRX, the $\{10-10\}\langle 1-210\rangle$ grains with lower stored energy might consume the $\{11-20\}\langle 1-100\rangle$ grains.

3. (ZA61-400, ZA63-340(400)) through whole extrusion process, SP texture strengthened with decrease in ED spread. And at the initial stage, most of the ED texture was already developed and intensity of the ED texture was maintained during the continuing extrusion process.

4. Regardless of extrusion temperature, SP textures were developed at the initial stage where massive DRXed grains were nucleated at the grain boundaries and replaced the parent grains by the NRX. Then during the continuing process, the SP split into DP only if the DRXed grains sustained their small size. At high temperature, the DRXed grains were grown and SP strengthened. Instead of that, TD (in ZA11) or ED (in ZA6x) texture was developed at high temperature.

5. As shown in Figure 3.12, $\{11-20\}\langle 1-100\rangle$ can strengthen with increase in activity of the prismatic $\langle a\rangle$ slip.

6. As shown in Figure 3.13, ED texture can occur from the random texture by activation of the pyramidal II $\langle c+a\rangle$ slip and inactivation of the tensile twin. However, unlike experimental texture (SP with ED), DP texture occurs by activation of the pyramidal II $\langle c+a\rangle$ in theoretical PSC texture.

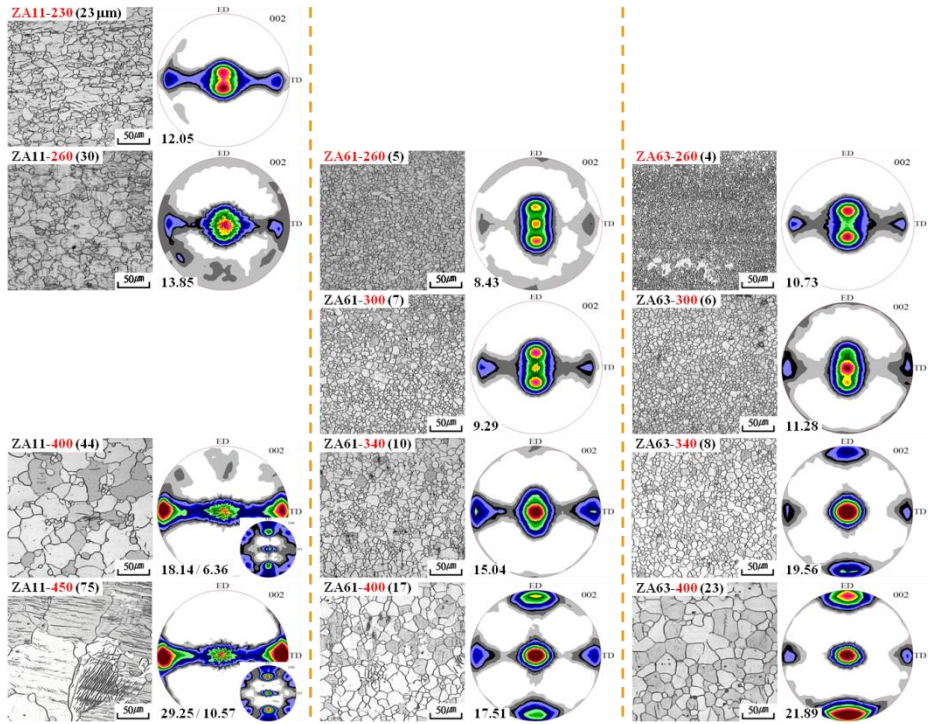


Figure 3.6 Microstructures and textures of ZA alloys extruded at different temperatures; (1) ZA11, (2) ZA61 and (3) ZA63 alloys.

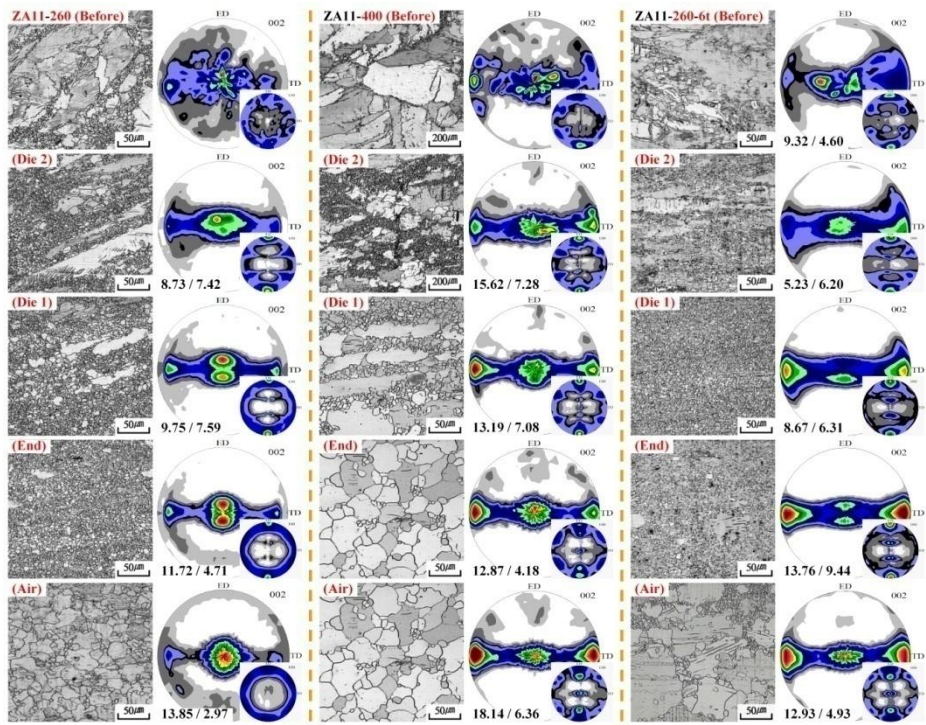


Figure 3.7 Microstructure and texture evolutions of ZA11 alloys during extrusions at 260 or 400°C; (1) ZA11-260, (2) ZA11-400 and (3) ZA11-260-6t.

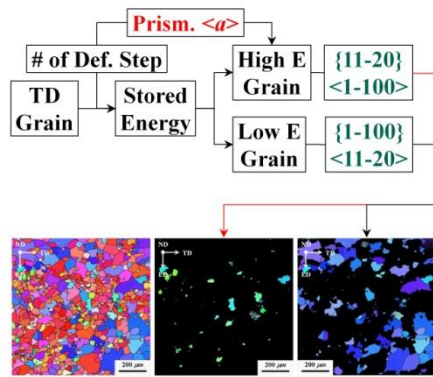
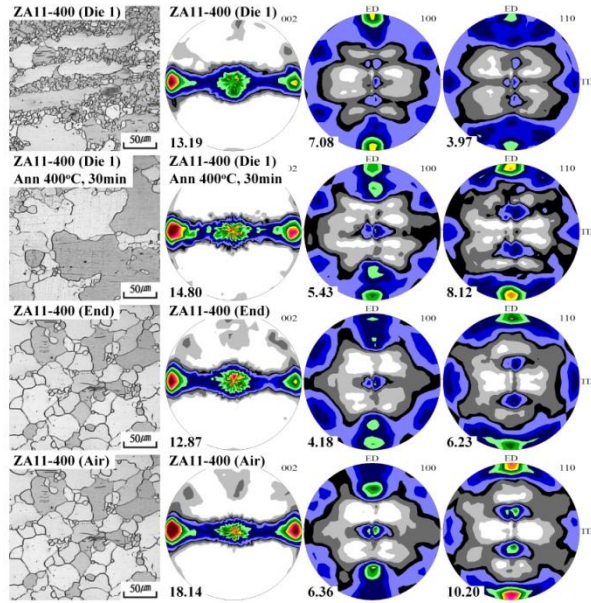


Figure 3.8 SRX textures of ZA11-400 after air-cooling or annealing at 400°C.

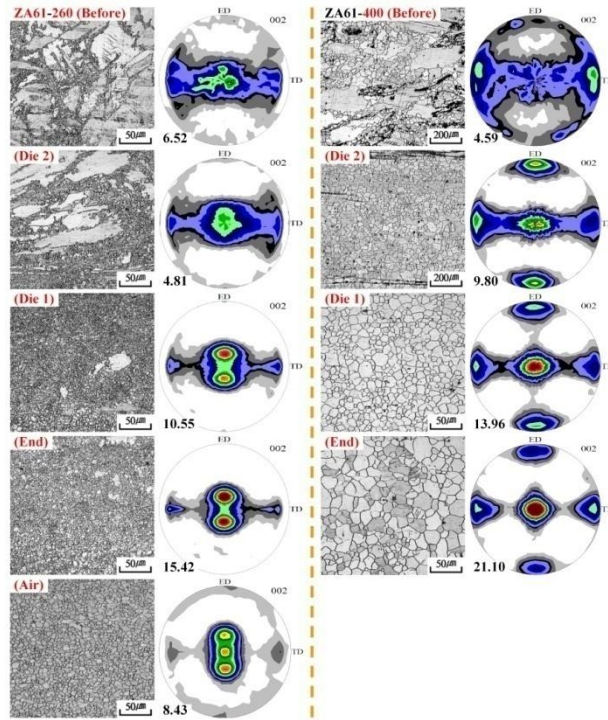


Figure 3.9 Microstructure and texture evolutions of ZA61 alloys during extrusions at 260 or 400°C; (1) ZA61-260 and (2) ZA61-400.

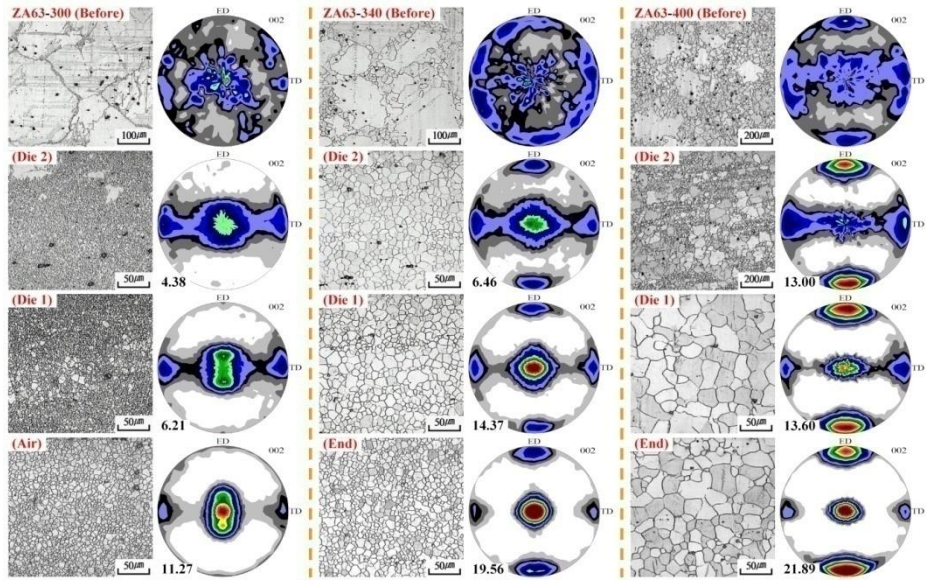


Figure 3.10 Microstructure and texture evolutions of ZA63 alloys during extrusions at different temperatures; (1) 300, (2) 340 and (3) 400°C.

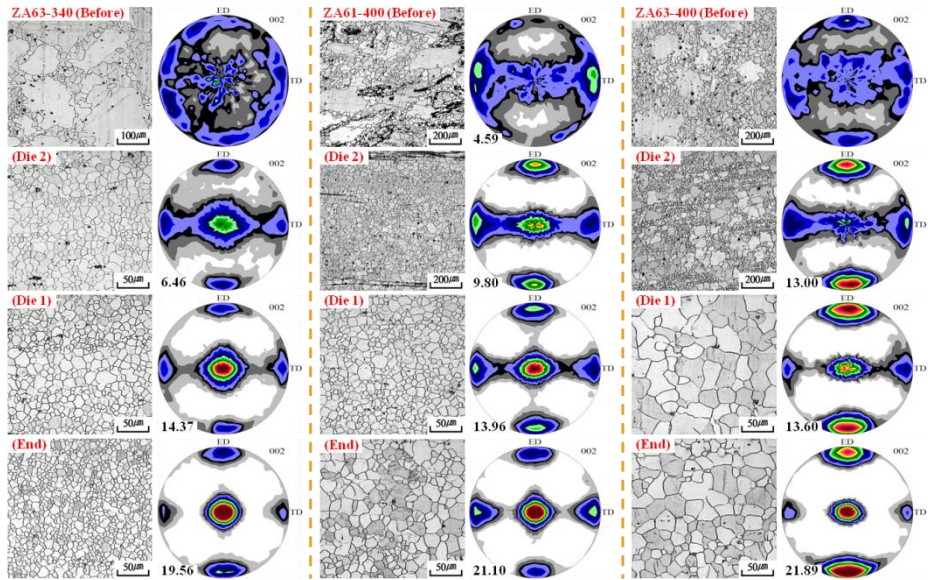


Figure 3.11 Microstructure and texture evolutions of ZA61 or ZA63 alloys during extrusions; (1) ZA63-340, (2) ZA61-400 and (3) ZA63-400.

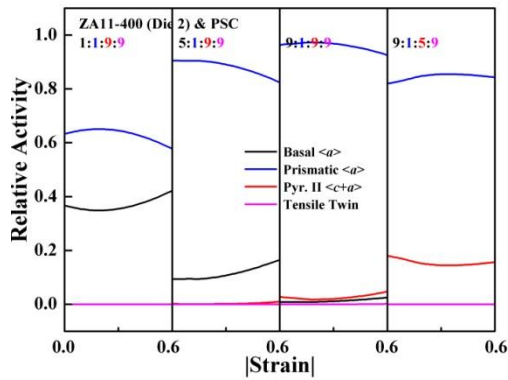
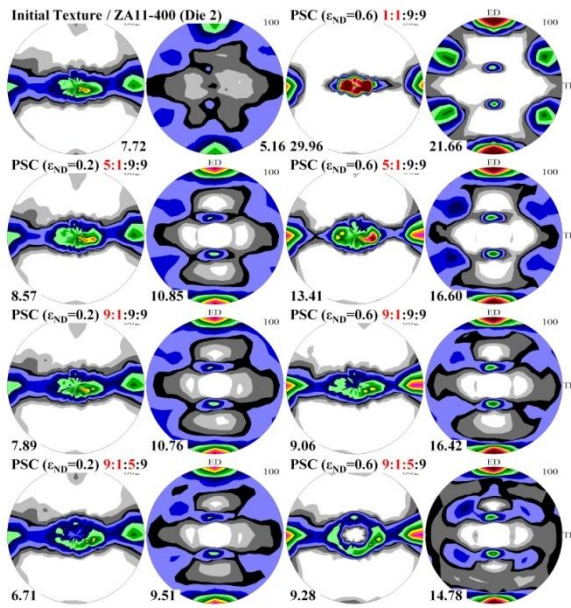


Figure 3.12 Theoretical deformation textures developed during PSC with different CRSS ratio; (initial texture) ZA11-400 (Die 2), (1) 1:1:9:9, (2) 5:1:9:9, (3) 9:1:9:9 and (4) 9:1:5:9.

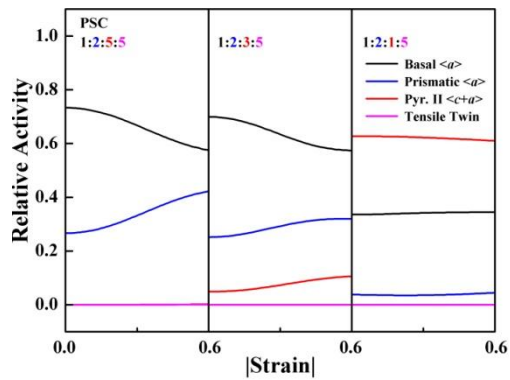
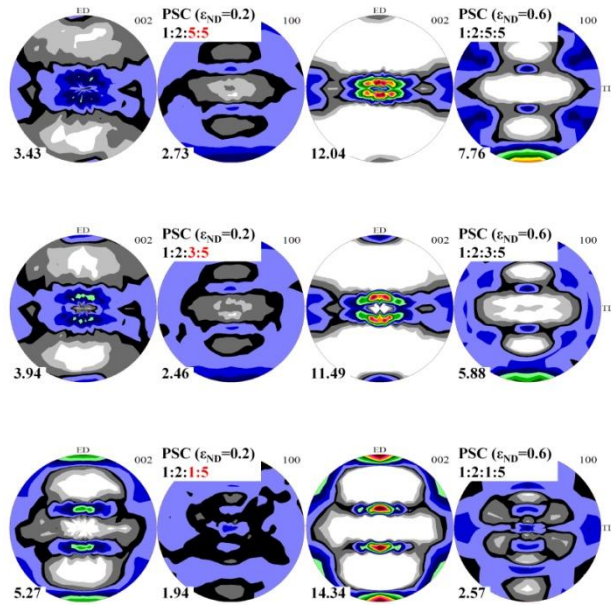


Figure 3.13 Theoretical deformation textures developed during PSC with different CRSS ratio; (initial texture) random texture, (1) 1:2:5:5, (2) 1:2:3:5 and (3) 1:2:1:5.

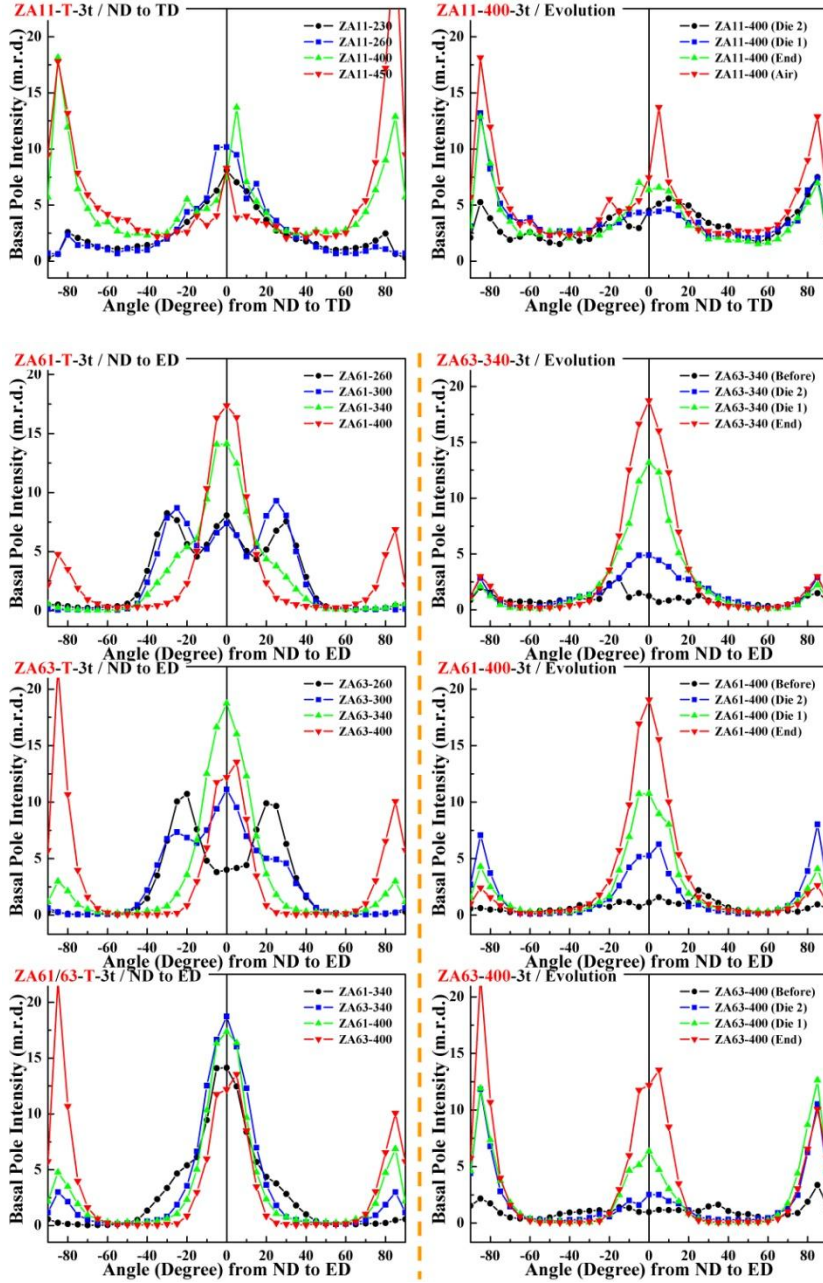


Figure 3.14 Distributions of basal pole intensities (with tilt angle from ND to ED or TD) of ZA alloys (ZA11, ZA61 and ZA63) extruded at different temperatures.

3.3 Effects of Ca on textures

Microstructures and textures of the extruded Ca-containing Mg or ZA alloys are represented in Figure 3.15 and 3.16 and their basal pole intensity distributions were compared in Figure 3.22 as follows;

1. In the all alloys, grain size decreased by addition of Ca or Ce. Especially, in the pure Mg and ZA11 extruded at high temperature whose grains were large, grain refinement effect was significant.
2. (Pure Mg) with addition of Ca or Ce, intensity of the DP texture weakened and ED spread and tilt angle corresponding to the peak in the DP texture increased.
3. (ZA1x) with addition of Ca or Ce, DP texture with weak intensity was developed and $\{11-20\}\langle 1-100\rangle$ texture was developed.
4. (ZA61) with addition of Ca, DP texture with weak intensity was developed and $\{11-20\}\langle 1-100\rangle$ texture was developed.
5. (ZA61) with addition of Ce, DP texture with strong intensity similar with one in the ZA61-260 was developed and $\{11-20\}\langle 1-100\rangle$ texture with relatively weaker intensity was developed.
6. As shown in Figure 3.22, because Ce is only soluble in the Z1 and not soluble in the ZA61 alloy, unlike Ca which is both soluble in the ZA11 and ZA61 alloys, weak DP + strong TD texture was developed only in the Z1Ce0.2-400.
7. With increase in Ca content in Z6 or ZA61 alloys, intensity of the TD texture increased instead of decrease in intensity of the DP texture.
8. With increase in Zn or Al contents in Z6 or ZA61 alloys, Ca-effect on texture diminished because Ca solubility decreased.

9. With increase in extrusion temperature in ZA61Ca1 alloys, grain size increased but it was relatively smaller than that of ZA61 alloy. And DP was changed into SP but with weaker intensity than that of ZA61 alloy and TD texture was developed. However, ZA61Ca1 alloy still sustained DP texture with fine microstructure even at 340°C.

Microstructure and texture evolutions of Ca-containing Mg or ZA alloys during the extrusions are represented in Figure 3.17 ~ 3.20 as follows;

1. (Mg-Ca) as shown in Figure 3.17, initially, $\langle 10\text{-}10 \rangle // \text{ED}$ texture was developed with the NRXed grains at the grain boundaries. Then DP texture was developed with the fully DRXed fine microstructure formed by the severe NRX.

2. (SRX texture in Mg-Ce) as shown in Figure 3.18, during annealing of the partially DRXed Ce0.2-400, $\langle 10\text{-}10 \rangle // \text{ED}$ texture disappeared and DP texture was developed with growth of the DRXed grains which had broader ED spread and weak $\langle 10\text{-}10 \rangle // \text{ED}$ texture.

3. (ZA11Ca1-340 / ZA61Ca2-340) as shown in Figure 3.19, initially, SP texture with $\{11\text{-}20\} \langle 1\text{-}100 \rangle$ texture was developed with the NRXed grains at the grain boundaries. Then the SP texture weakened and it was changed into the DP texture with the fully DRXed fine microstructure formed by the severe NRX.

4. (ZA61Ca1-T) as shown in Figure 3.20, overall tendency was similar with the ZA61 alloys except weaker intensity and finer grain size. Regardless of extrusion temperature, SP textures were developed at the initial stage where massive fine NRXed grains were replacing the parent grains. Then during the continuing process, the SP split into DP only if the DRXed grains sustained their small size. At high temperature, DRXed grains were grown and

SP strengthened. Instead of that, TD texture was developed at high temperature.

5. As shown in Figure 3.21, $\{11-20\}\langle 1-100\rangle$ can strengthen with increase in activity of the prismatic $\langle a \rangle$ slip. In addition, SP can weaken and split into weak DP by activation of the pyramidal II $\langle c+a \rangle$ slip. Additionally, by activation of the tensile twin at the initial strain, quadruple basal texture can be developed.

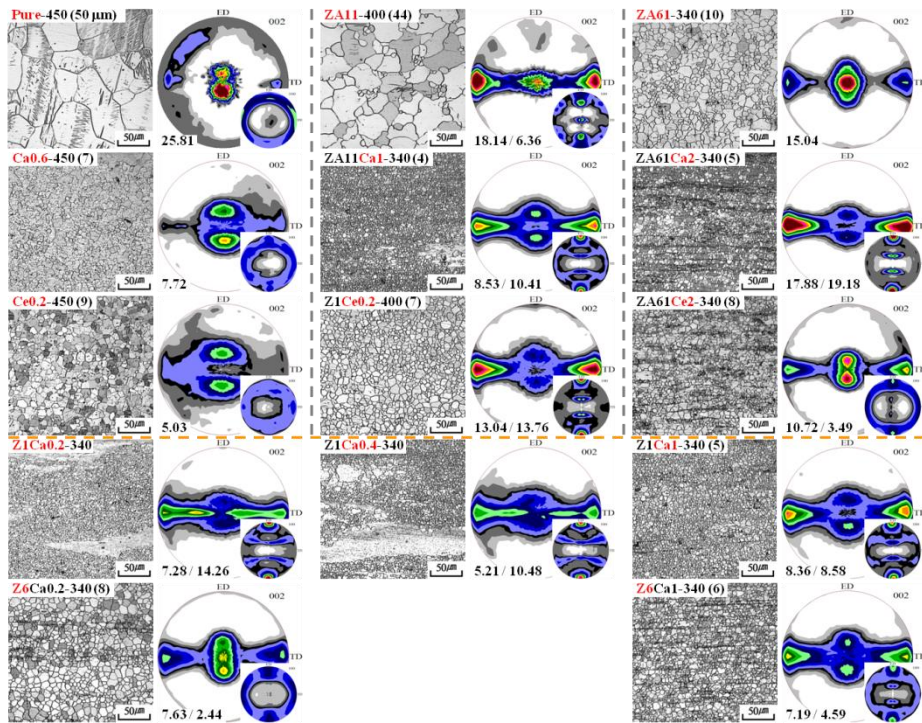


Figure 3.15 Microstructures and textures of extruded Ca-containing Mg or ZA alloys; (1) comparison between Ca and Ce effects and (2) effects of Zn and Ca contents.

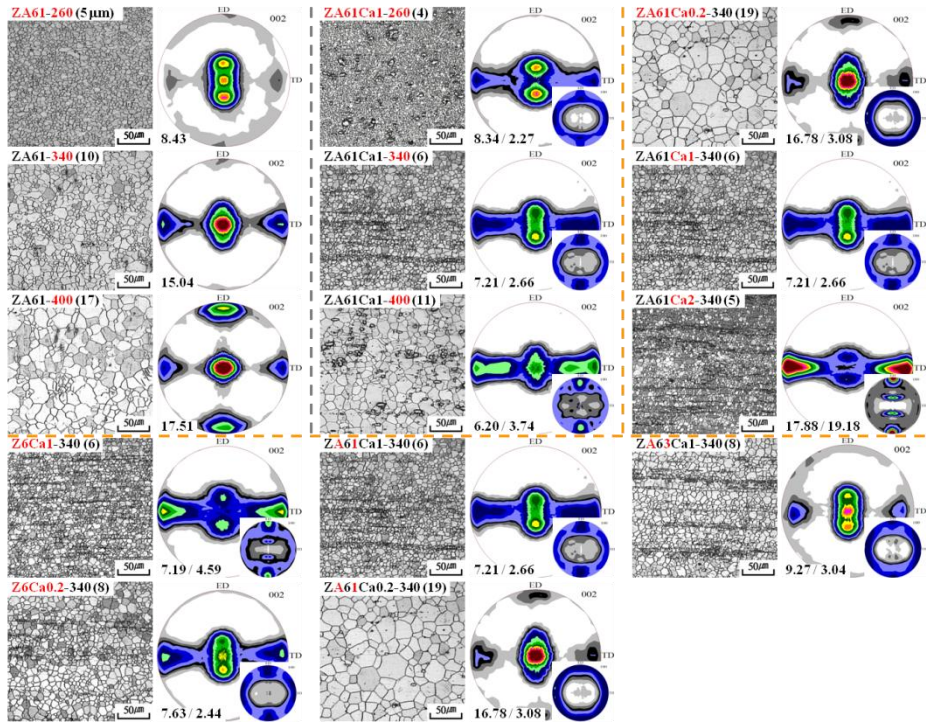


Figure 3.16 Microstructures and textures of extruded Ca-containing ZA61 alloys; (1) ZA61Ca1 alloys extruded at different temperatures and (2) effects of Zn, Al and Ca contents.

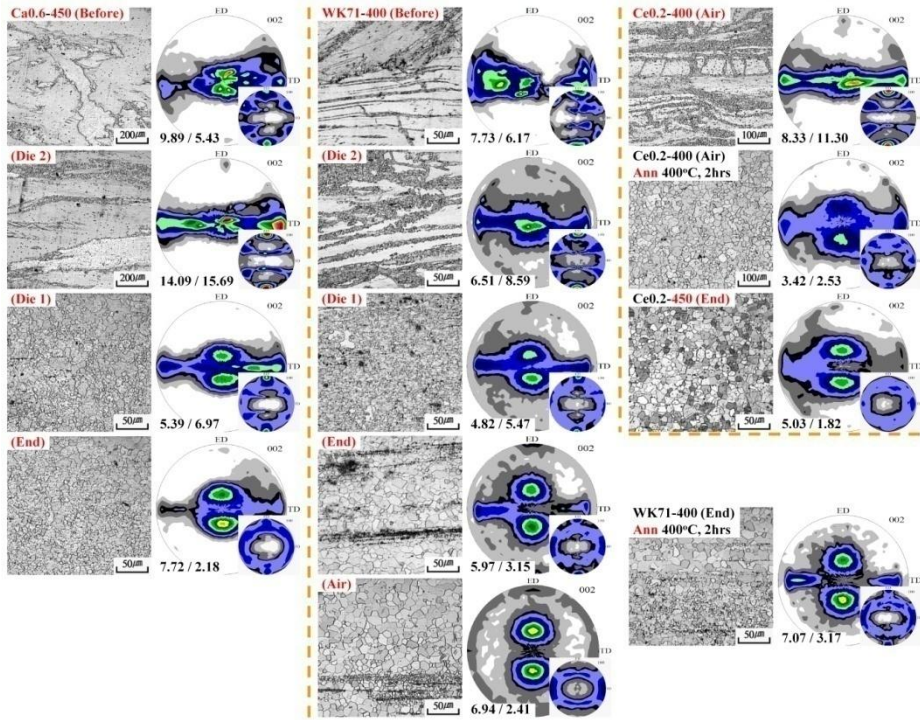


Figure 3.17 Microstructure and texture evolutions of Ca-containing Mg alloys during extrusions; (1) Mg-0.6Ca-450, (2) Mg-7Y-1Zr-400 and (3) Mg-0.2Ce-400.

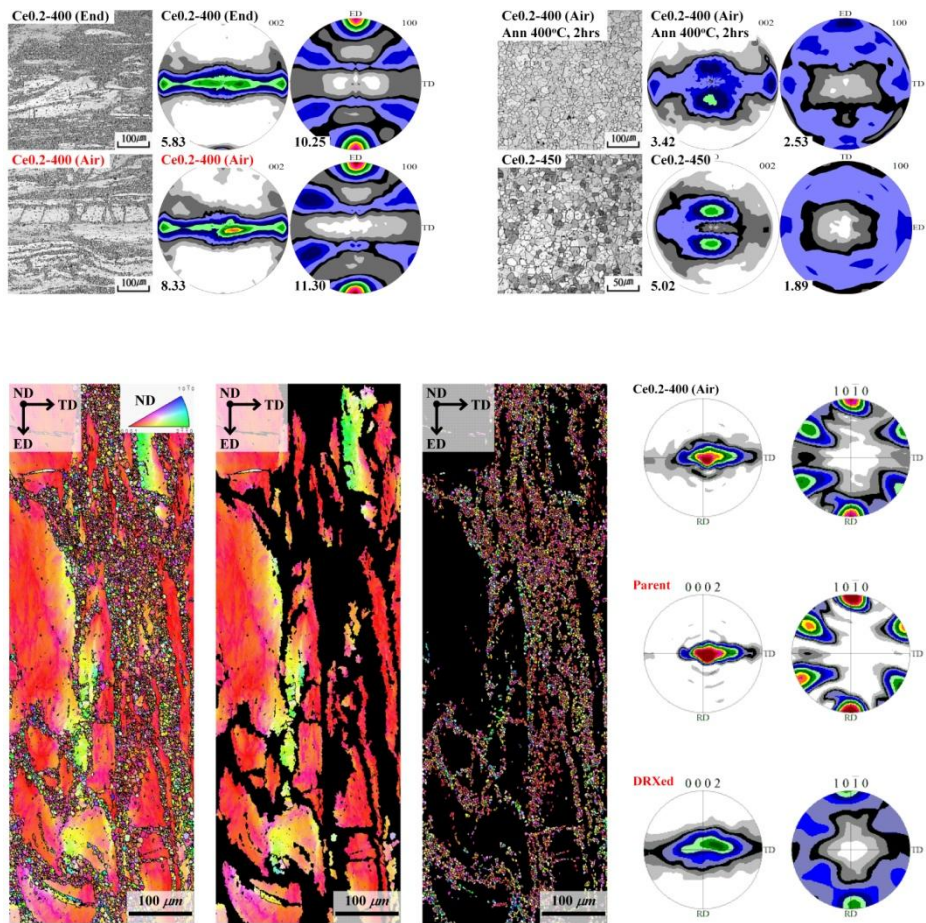


Figure 3.18 SRX textures of Ce_{0.2}-400 (Mg-0.2Ce alloy extruded at 400°C) after air-cooling or annealing at 400°C.

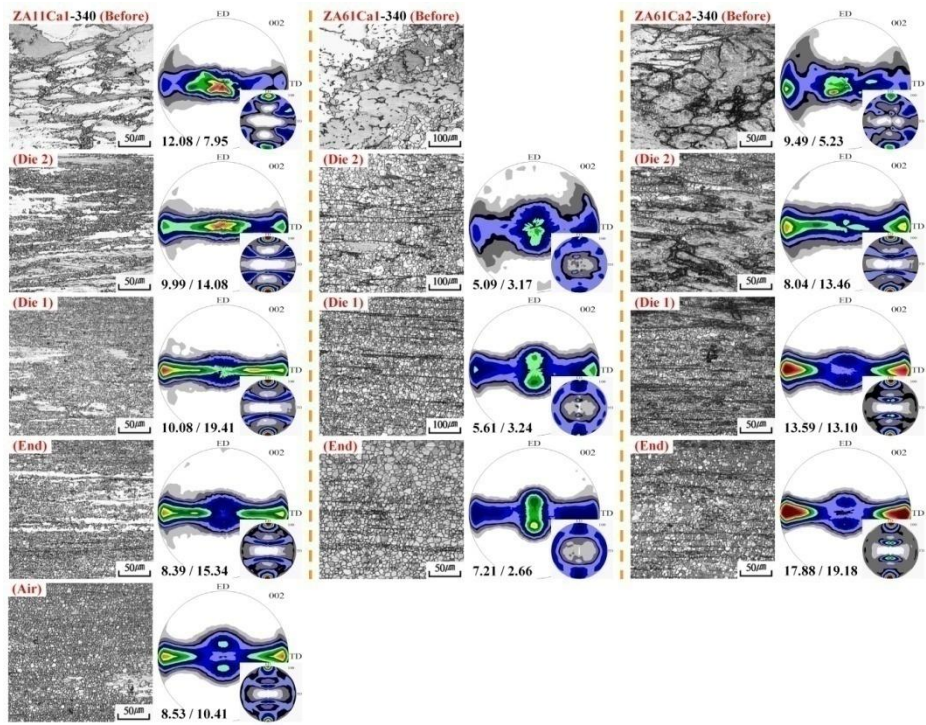


Figure 3.19 Microstructure and texture evolutions of Ca-containing ZA alloys during extrusions at 340°C; (1) ZA11Ca1, (2) ZA61Ca1 and (3) ZA61Ca2 alloy.

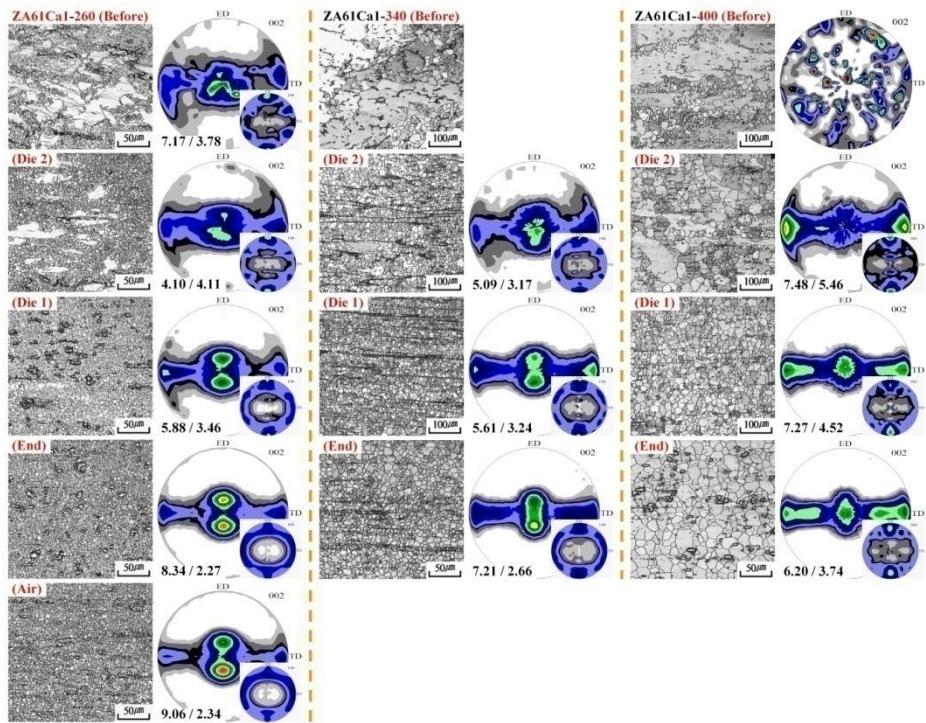


Figure 3.20 Microstructure and texture evolutions of ZA61Ca1 alloys during extrusions at different temperatures; (1) 260, (2) 340 and (3) 400°C.

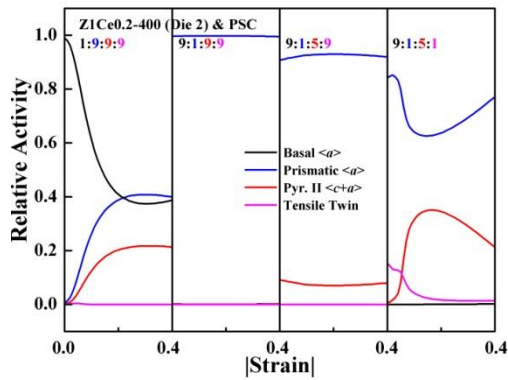
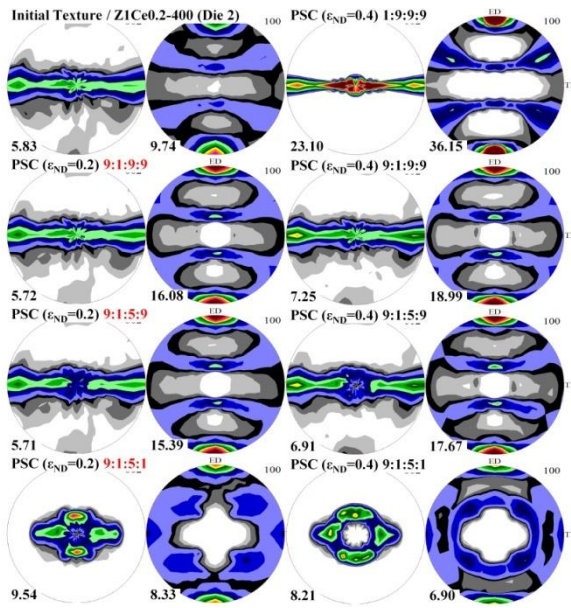


Figure 3.21 Theoretical deformation textures developed during PSC with different CRSS ratio; (initial texture) ZrCe0.2-400 (Die 2), (1) 1:9:9:9, (2) 9:1:9:9, (3) 9:1:5:9 and (4) 9:1:5:1.

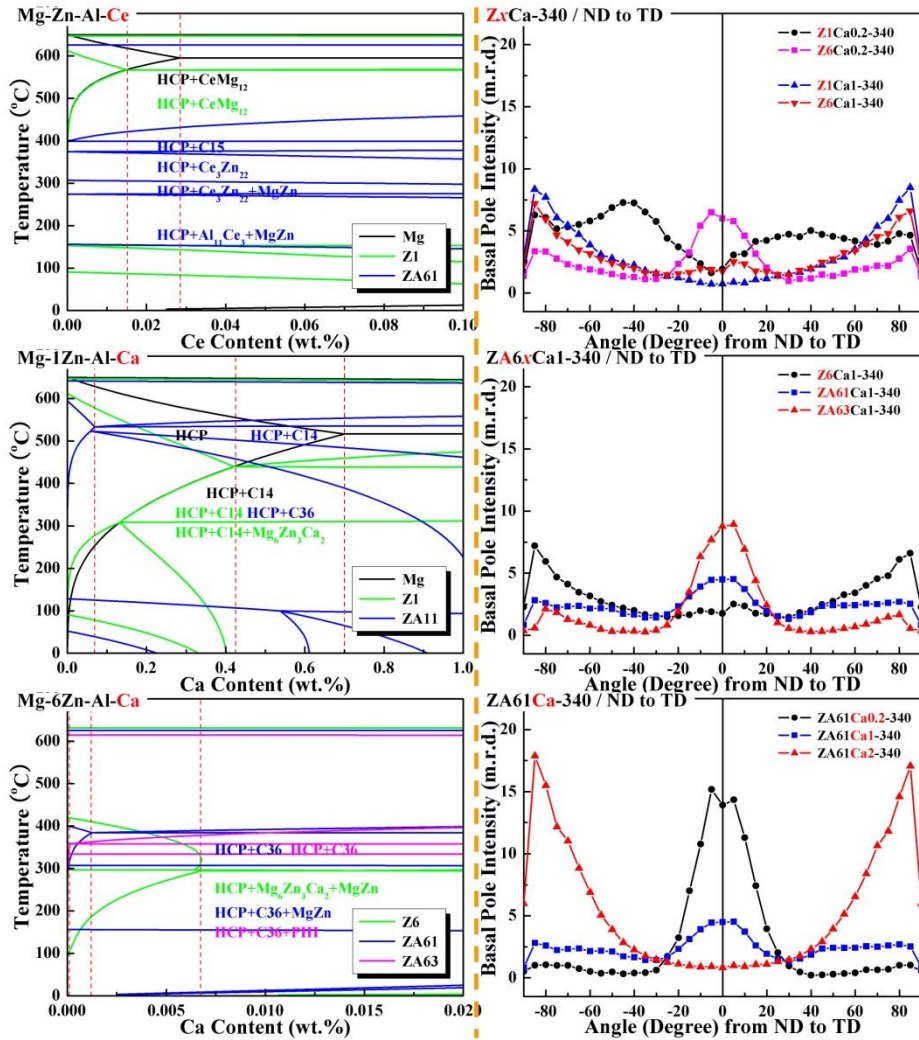


Figure 3.22 Distributions of basal pole intensities (with tilt angle from ND to ED or TD) of extruded Ca-containing ZA alloys; (1) Ce or Ca solubility (phase diagrams) and (2) basal pole intensities.

3.4 Summary

Extrusion texture results and possible texture development mechanisms were summarized in Figure 3.23 as follows;

1. DP texture was developed at low temperature but SP texture was developed at high temperature;

In the ZA alloys extruded at 260°C, DP texture was developed with fine microstructure developed by the NRX. And with increase in extrusion temperature, SP texture was developed with coarse microstructure developed by the ordinary DRX. In the Ca-containing ZA alloys, even at relatively high temperature of 340°C, DP texture was developed with fine microstructure. And with increase in extrusion temperature, SP texture was developed with coarse microstructure.

These phenomena can be explained from the viewpoint of the grain-size dependant compatibility deformation. Theoretically, DP texture can be developed by activation of the pyramidal II $\langle c+a \rangle$ slip. And this pyramidal II $\langle c+a \rangle$ slip which has high CRSS value can be activated by aid of the compatibility stress resulted from the grain size refinement. Moreover, effect of Ca addition on texture was significant at high temperature rather than low temperature because decrement of the grain size was larger at high temperature. Therefore, even at high temperature, DP texture can be developed in the Ca-containing ZA alloys.

However, with increase in extrusion temperature, grain growth occurs and DRXed grains consume the parent grains by their growth instead of nucleation of new DRXed grains (NRX). As grain size increases, compatibility stress can be activated only near the grain boundary and cannot propagate

inside the grain. Therefore, only basal slip which has low CRSS value can be activated inside the grain and SP texture is developed by the basal slip.

2. Tilt angle corresponding to the peak in DP texture increased with increase in Zn and Al content;

In the ZA alloys extruded at 260°C, with increase in Zn and Al content, ED spread and tilt angle corresponding to the peak in DP texture increased.

At first, with increase in Zn and Al contents, as-cast grain size (initial grain size before extrusion) decreases. Therefore, because parent grain boundary acts as a nucleation site, NRX is promoted and fraction of the small DRXed grain region increases during extrusion process with increase in Zn and Al contents. This can enhance the activity of the pyramidal II $\langle c+a \rangle$ slip.

At second, these phenomena can be explained from the viewpoint of the thermal activation of the cross-slip. With increase in Zn and Al content, solidus temperature decreases and inversely, homologous temperature increases. With increase in homologous temperature, activity of the pyramidal II $\langle c+a \rangle$ slip can be enhanced by aid of the increased thermal stress. As compared with rare earth elements, effect of Zn and Al on SFE is relatively insignificant. However, in the solidus temperature, Zn and Al decrease the solidus temperature significantly.

3. ED texture ($\langle 0001 \rangle //$ ED texture) was developed at high temperature and intensity of the ED texture increased with increase in Al content;

In the ZA61 and ZA63 alloys extruded at high temperature (340°C, 400°C), ED texture occurred and intensity of the ED texture increased with increase in temperature. And also the intensity of the ED texture increased with increase in Al content.

These phenomena also can be explained from the viewpoint of the thermal activation of the cross-slip. Theoretically, ED texture can be developed at the

condition where the tensile twin is inactivated and the pyramidal II $\langle c+a \rangle$ slip is activated. And at sufficiently high temperature (transition temperature), CRSSes of the tensile twin and pyramidal II $\langle c+a \rangle$ slip can be reversed. With increase in Al content, solidus temperatures of the ZA6x alloys decrease as 400°C for the ZA61 and 363°C for the ZA63 alloy and inversely, homologous temperatures increase. With increase in homologous temperature, activity of the pyramidal II $\langle c+a \rangle$ slip can be enhanced by aid of the thermal stress and the transition temperature can be lowered.

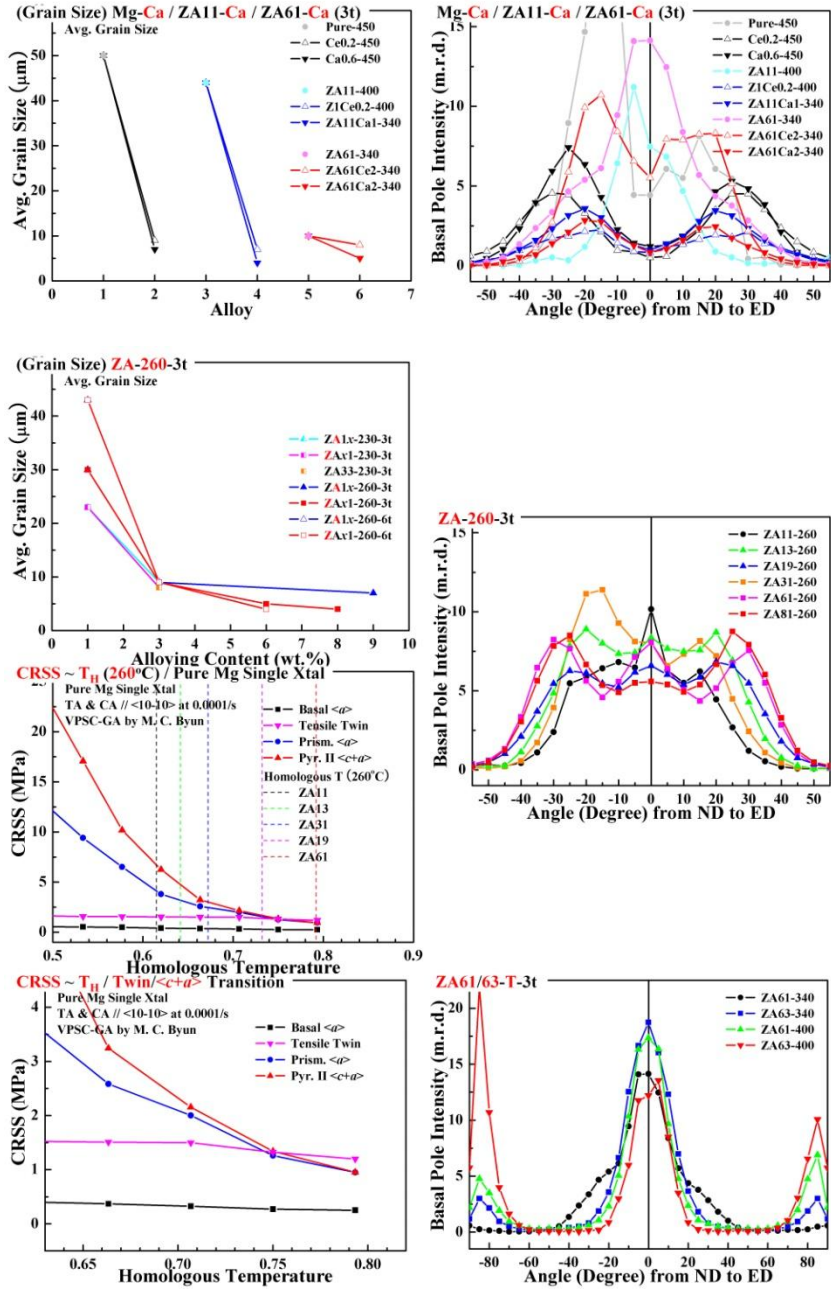


Figure 3.23 Summary; analysis on (1) DP texture based on grain size and (2) ED texture based on solidus temperature.

Chapter 4 Discussions

4.1 Two-step PSC of extruded plate

Microstructures and textures of the 15×6t sectional extruded ZAx1 alloys before the second step PSC in the two-step PSC are represented in Figure 4.1 as follows;

1. After the first step PSC in the two-step PSC (CA // TD), SP texture with wide LD spread (spread of the basal poles toward LD (//ND)) was developed.
2. After the first step PSC in the two-step PSC (CA // ED), SP texture with weak CD texture ($\langle 0001 \rangle$ //CD (//TD) texture) was developed.
3. After the first step PSC in the two-step PSC, with increase in Zn content, grain size decreased as 25 or 17 μm for the ZA11, 8 μm for the ZA31, 4 μm for the ZA61 alloy.
4. (Annealed ZA61 alloys) after the first step PSC in the two-step PSC (CA // TD), grain size was 4 μm for the as-extruded one, 14 μm for the 300°C-annealed one and 23 μm for the 450°C-annealed one with similar SP textures.

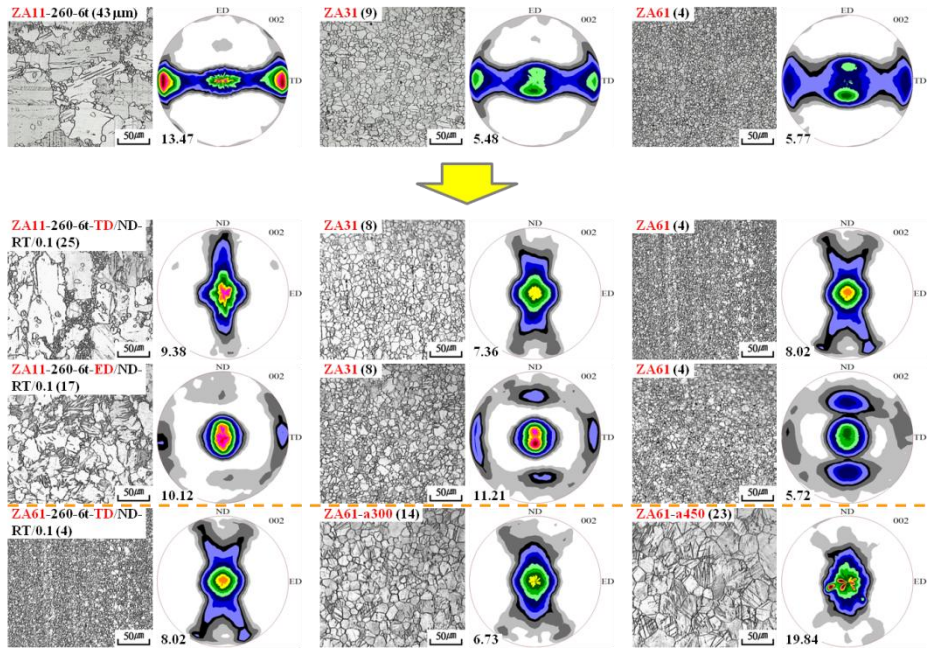


Figure 4.1 Microstructures and textures of extruded ZAx1 alloys before second step PSC in two-step PSC; (1) initial state and (2) after first step.

4.1.1 Two-step PSC (CA // TD)

Microstructures and textures of the extruded ZAx1 alloys after the second step PSC at different temperatures (200 ~ 550°C) with an initial strain rate of 0.0002 or 0.0400/sec in the two-step PSC (CA // TD) are represented in Figure 4.2 as follows;

In the two-step PSC (CA // TD) of the ZAx1 alloys,

200°C - DP - ($T_{DP, low}$) - SP - ($T_{DP, high}$) - DP - (T_{CD}) - DP + CD - 550°C

1. At relatively low temperature, DP texture was developed with the partially DRXed fine microstructure developed by the NRX.
2. At mid temperature, SP texture was developed with the fully DRXed coarse microstructure developed by the NRX and grain growth.
3. At high temperature, DP + CD texture (DP and {11-20}<1-100> texture) was developed with large grains occurred by ordinary DRX.
4. With increase in Zn content, $T_{DP, low}$ (highest temperature where DP texture could be developed) decreased as 340°C for the ZA11, 260°C for the ZA31 and 260°C for the ZA61 alloy. In the ZA11 alloy, DP texture was still developed with the partially DRXed microstructure even at 340°C. Above 300°C, in the ZA31 and ZA61 alloys, SP textures were developed but LD spread in the ZA61 alloy was smaller than that in the ZA31 alloy until at 400°C.
5. With increase in Zn content, LD spread and tilt angle corresponding to the peak in DP texture developed at low temperature increased as 5° for the ZA11, 15° for the ZA31, 20° for the ZA61 at 200°C and 10° for the ZA11, 15° for the ZA31, 20° for the ZA61 at 260°C, 0.0400/sec and 10° for the ZA11, 15° for the ZA31, 20° for the ZA61 at 260°C and 10° for the ZA11, 10° for the ZA31, 20° for the ZA61 at 300°C, 0.0400/sec.

6. With increase in Zn content, $T_{DP, high}$ (lowest temperature where DP texture could be developed) decreased as 550°C for the ZA11, 420°C for the ZA31 and 420°C for the ZA61 alloy.
7. With increase in Zn content, LD spread and tilt angle corresponding to the peak in DP texture developed at high temperature increased as 10° for the ZA11 at 550°C, 15° for the ZA31 at 500°C and 25° for the ZA61 at 420°C.
8. With increase in Zn content, T_{CD} (lowest temperature where CD texture could be developed) decreased as 550°C for the ZA11, 500°C for the ZA31 and 400°C for the ZA61 alloy.
9. With increase in Zn content, intensity of the CD texture increased.
10. Above 340°C, grain size increased with increase in Zn content because of the increase in grain growth rate originated from the decrease in solidus temperature as 594°C for the ZA11, 520°C for the ZA31 and 400°C for the ZA61 alloy.
11. Effect of increase in strain rate was similar to the effect of decrease in temperature because flow stress increased and grain size decreased with increase in strain rate.
12. (ZA61) at 260°C, DP textures were developed with the partially DRXed fine microstructures in both 0.0002 and 0.0400/sec.
13. (ZA61) at 300 and 340°C, SP texture was developed in 0.0002/sec but DP texture was developed in 0.0400/sec with fine grains.
14. (ZA61) at 450°C, DP + CD texture was developed in 0.0002/sec but SP texture was developed in 0.0400/sec with smaller grains.
15. DP texture was sustained until the partially DRXed fine microstructure was sustained. And SP texture was developed with the fully DRXed coarse microstructure.

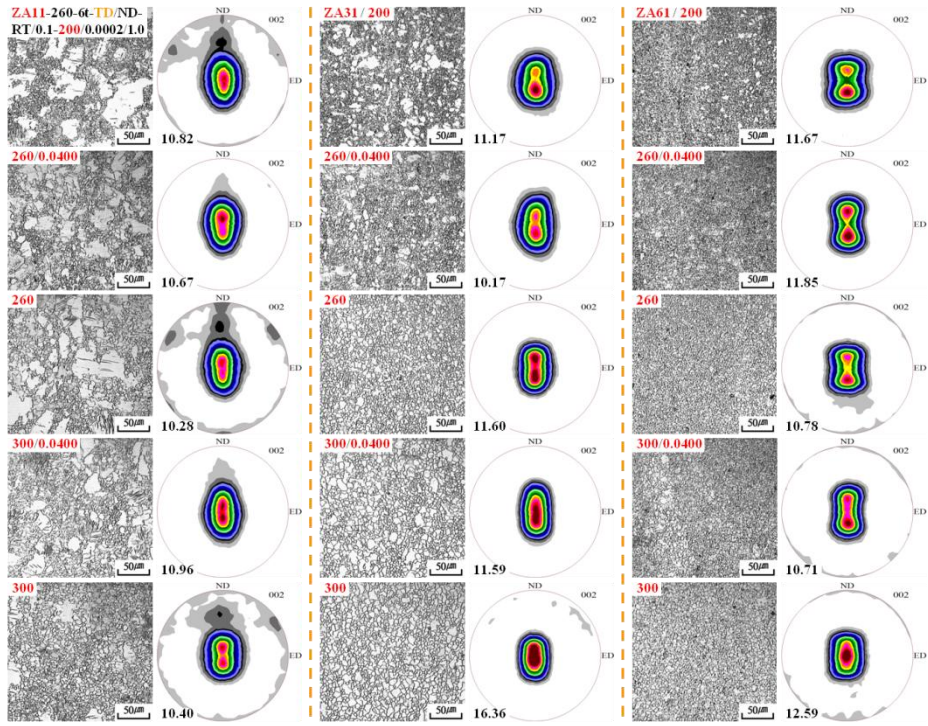


Figure 4.2 Microstructures and textures of extruded ZAx1 alloys after second step PSC at different temperatures (200 ~ 550°C) with initial strain rate of 0.0002 or 0.0400/sec in two-step PSC (CA // TD).

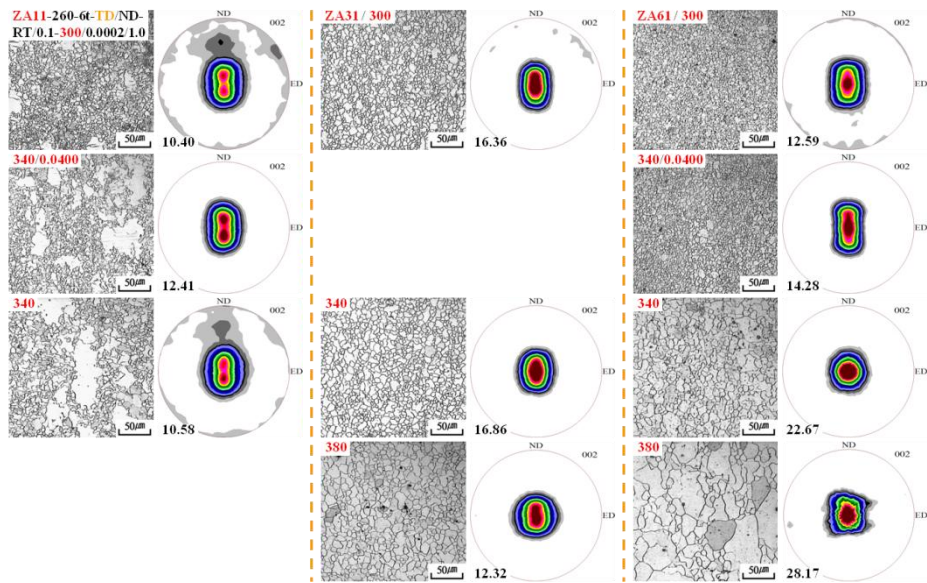


Figure 4.2 Continued.

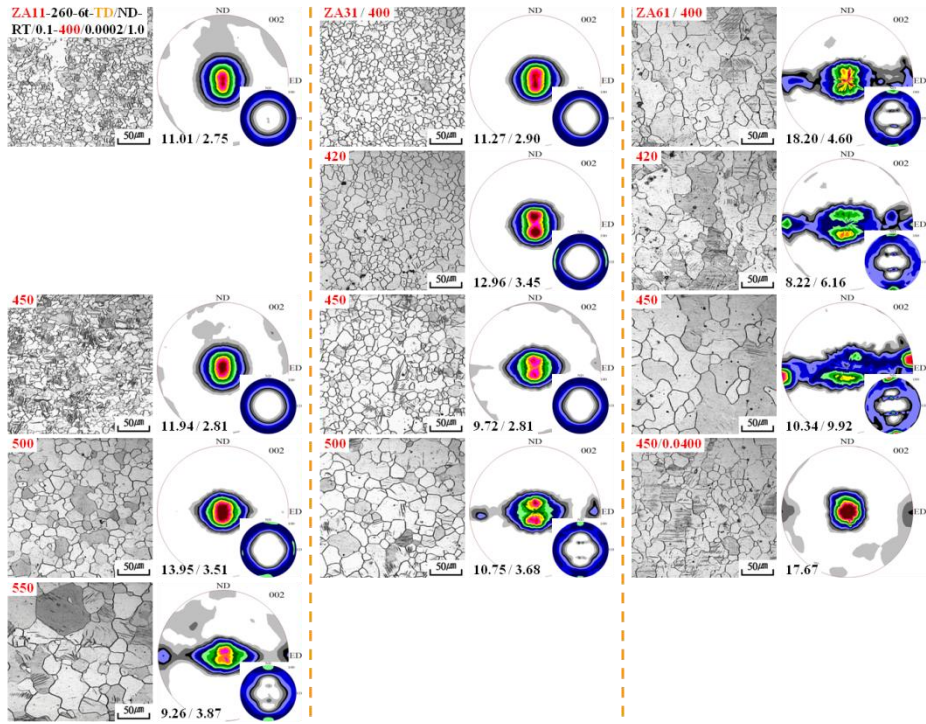


Figure 4.2 Continued.

4.1.2 Two-step PSC (CA // ED)

Microstructures and textures of the extruded ZAx1 alloys after the second step PSC at different temperatures (200 ~ 550°C) in the two-step PSC (CA // ED) are represented in Figure 4.3 as follows;

In the two-step PSC (CA // ED) of the ZAx1 alloys,

200°C - DP - ($T_{DP, low}$) - SP - (T_{CD}) - SP + CD - ($T_{DP, high}$) - DP + CD - 550°C

1. At low temperature, DP texture was developed with the partially DRXed fine microstructure developed by NRX.

2. At mid temperature, SP + CD texture was developed with the fully DRXed coarse microstructure developed by NRX and grain growth.

3. At high temperature, DP + strong CD texture was developed with large grains occurred by ordinary DRX. With increase in temperature, intensity of the CD texture increased instead of decrease in intensity of the DP texture.

4. With increase in Zn content, $T_{DP, low}$ decreased as 340°C for the ZA11, 300°C for the ZA31 and 300°C for the ZA61 alloy.

5. With increase in Zn content, LD spread and tilt angle corresponding to the peak in DP texture developed at low temperature increased as 0° for the ZA11, 5° for the ZA31 and 20° for the ZA61 at 260°C.

6. With increase in Zn content, T_{CD} decreased as 550°C for the ZA11, 340°C for the ZA31 and 340°C for the ZA61 alloy.

7. With increase in Zn content, intensity of the CD texture increased.

8. With increase in Zn content, $T_{DP, high}$ decreased as 550°C for the ZA11, 380°C for the ZA31 and 380°C for the ZA61 alloy.

9. With increase in Zn content, LD spread and tilt angle corresponding to the peak in DP texture developed at high temperature increased as 15° for the ZA11 at 550°C, 15° for the ZA31 at 400°C and 25° for the ZA61 at 400°C.

10. Above 340°C, grain size increased with increase in Zn content because of increase in grain growth rate originated from decrease in solidus temperature.

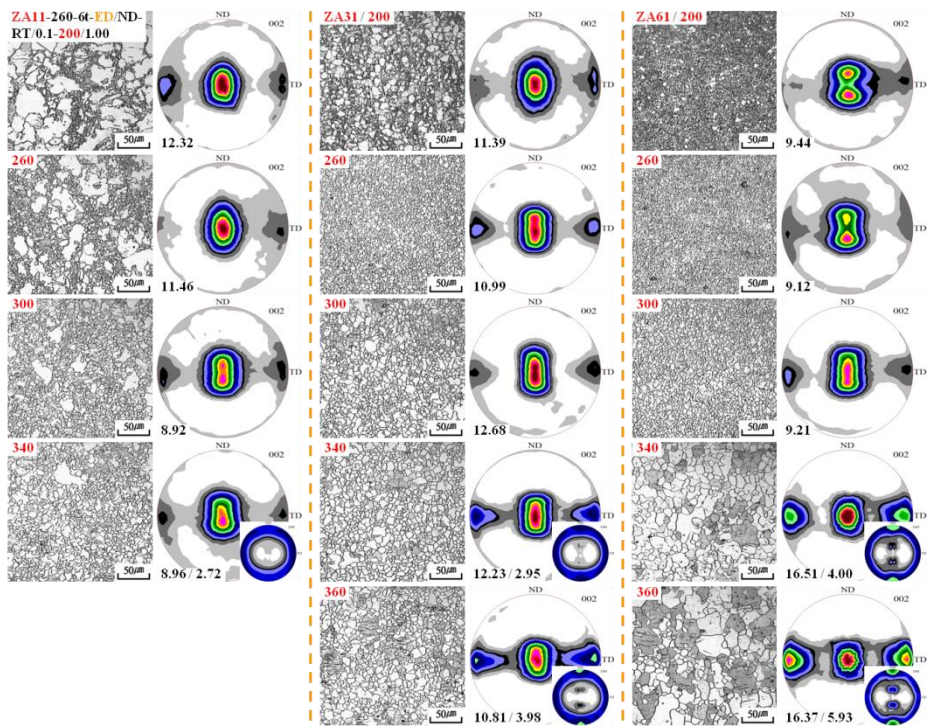


Figure 4.3 Microstructures and textures of extruded ZAx1 alloys after second step PSC at different temperatures (200 ~ 550°C) in two-step PSC (CA // ED).

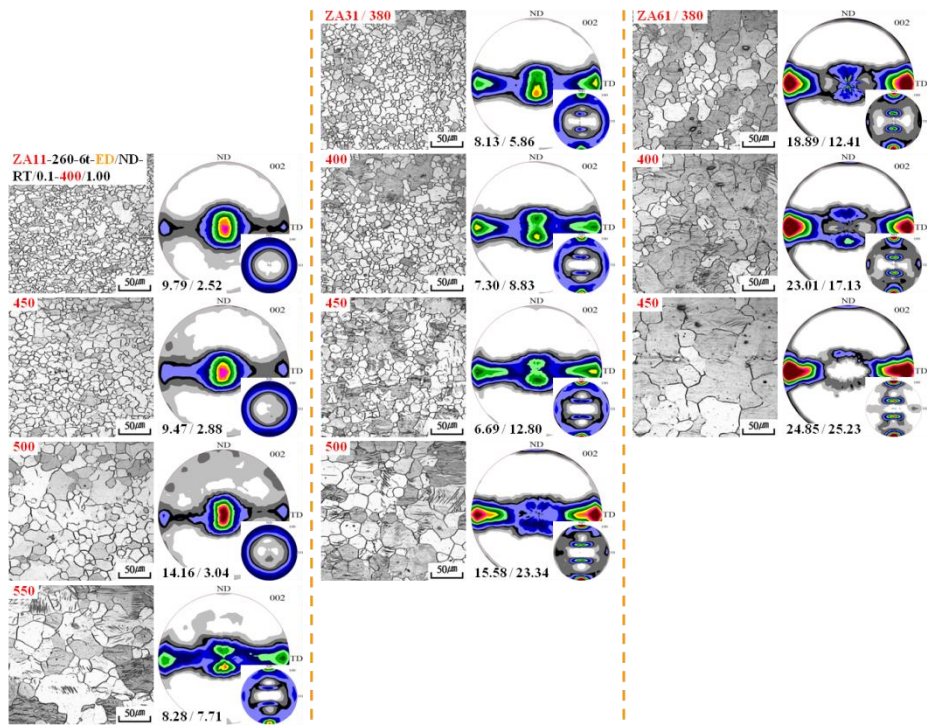


Figure 4.3 Continued.

4.1.3 Texture development process

Microstructure and texture evolutions of the extruded ZA61 alloys during the second step PSC at different temperatures (200 ~ 450°C) in the two-step PSC (CA // TD) and at 400°C in the two-step PSC (CA // ED) are represented in Figure 4.4 as follows;

1. (Low temperature) at initial stage, SP texture strengthened and LD spread decreased. Then the SP split into DP but still the LD spread decreased with fine microstructure.
2. (Mid temperature) throughout the whole process, SP texture strengthened and LD spread decreased with some amount of grain growth.
3. (High temperature) at initial stage, SP texture strengthened and LD spread decreased. Then the SP split into DP but still the LD spread decreased. At mid stage, split angle between two peaks and LD spread decreased but the CD spread in DP texture increased. Then the CD texture occurred. After occurrence of the CD texture, the DP texture weakened and the CD texture strengthened with severe grain growth.
4. (High temperature) as shown in Figure 4.5, during the second step PSC (CA // ED) at 400°C, the CD grains (grains with CD texture) grew faster with consuming the DP grains (grains with DP texture). At the initial stage, the SP grains might accommodate the LD strain by basal $\langle a \rangle$ and pyramidal II $\langle c+a \rangle$ slips and after all might become DP grains, which might have higher stored energy. During the continuing PSC, the CD grains which might have lower stored energy grew faster and might accommodate the LD strain by prismatic $\langle a \rangle$ slip at the same time.
5. (High temperature) as shown in Figure 4.6 and 4.7, with increase in Zn content, LD spread and tilt angle corresponding to the peak in DP texture

increased and this tendency was more clear in the initially developed DP textures (strain of 0.25) as 10° for the ZA11, 20° for the ZA31, 25° for the ZA61 at 400°C and 10° for the ZA11 at 550°C , 20° for the ZA31 at 500°C and 25° for the ZA61 at 420°C in the two-step PSC (CA // TD). And also in the two-step PSC (CA // ED) at 400°C , they increased as 30° for the ZA31 and 35° for the ZA61 at 400°C .

6. As shown in Figure 4.8, DP texture can be developed from the SP texture corresponding to the texture of the ZA61-260-6t-TD/ND-RT/0.1-200/0.12 by activation of the pyramidal II $\langle c+a \rangle$ slip. And tilt angle corresponding to the peak in DP texture can increase with increase in activity of the pyramidal II $\langle c+a \rangle$ slip.

7. As shown in Figure 4.9, DP texture can be developed from the SP texture corresponding to the texture of the ZA61-260-6t-ED/ND-RT/0.1-400/0.05 by activation of the pyramidal II $\langle c+a \rangle$ slip. And tilt angle corresponding to the peak in DP texture can increase with increase in activity of the pyramidal II $\langle c+a \rangle$ slip.

8. As shown in Figure 4.10, $\{11-20\}\langle 1-100 \rangle$ texture can strengthen with increase in activity of the prismatic $\langle a \rangle$ slip. Moreover, $\{11-20\}\langle 1-100 \rangle$ texture can occur from the random texture by activation of the prismatic $\langle a \rangle$ slip as shown in Figure 1.3.

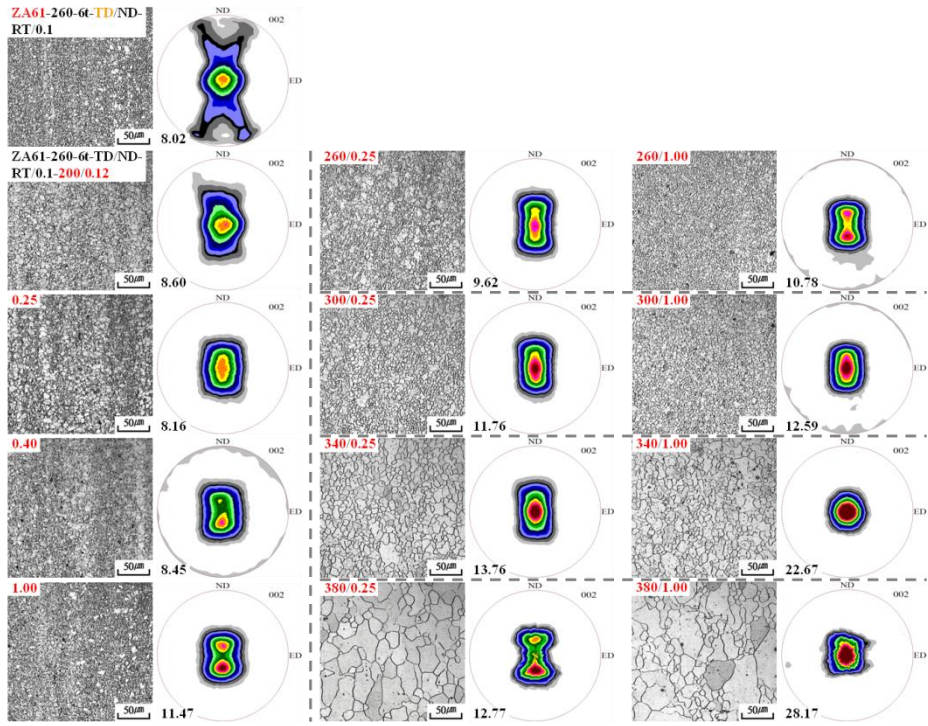


Figure 4.4 Microstructure and texture evolutions of extruded ZA61 alloys during second step PSC at different temperatures (200 ~ 450°C) in two-step PSC (CA // TD).

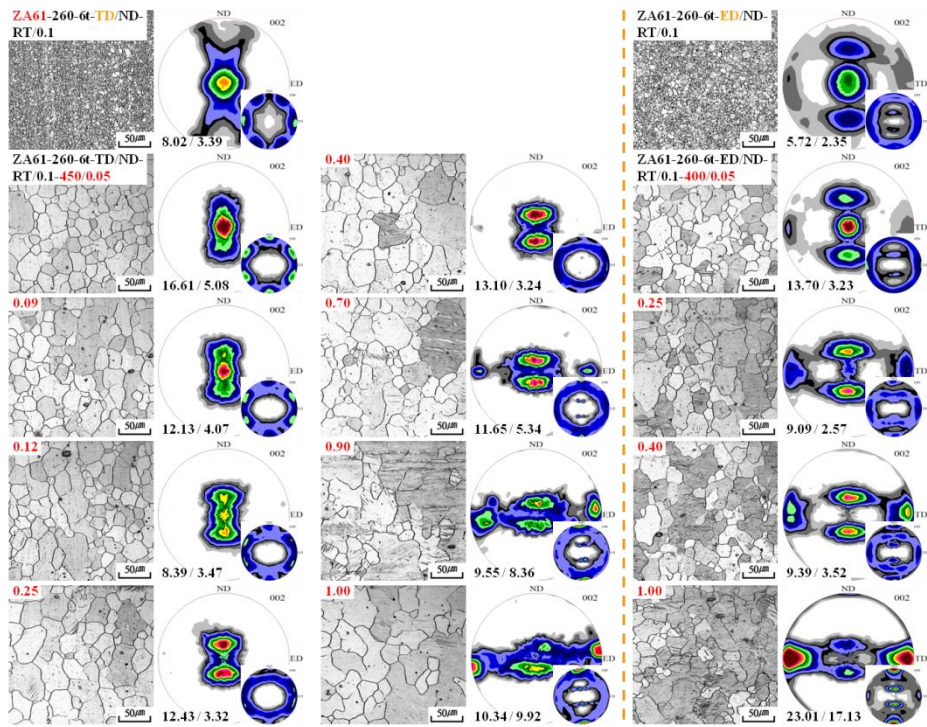


Figure 4.4 Continued; (1) PSC (CA // TD) at 450°C and (2) PSC (CA // ED) at 400°C.

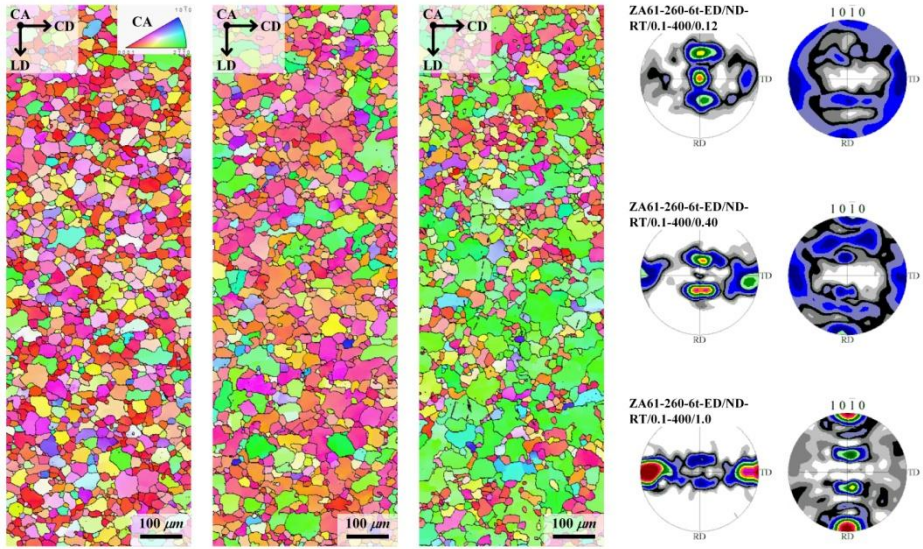


Figure 4.5 Texture evolution of extruded ZA61 alloy during second step PSC at 400°C in two-step PSC (CA // ED).

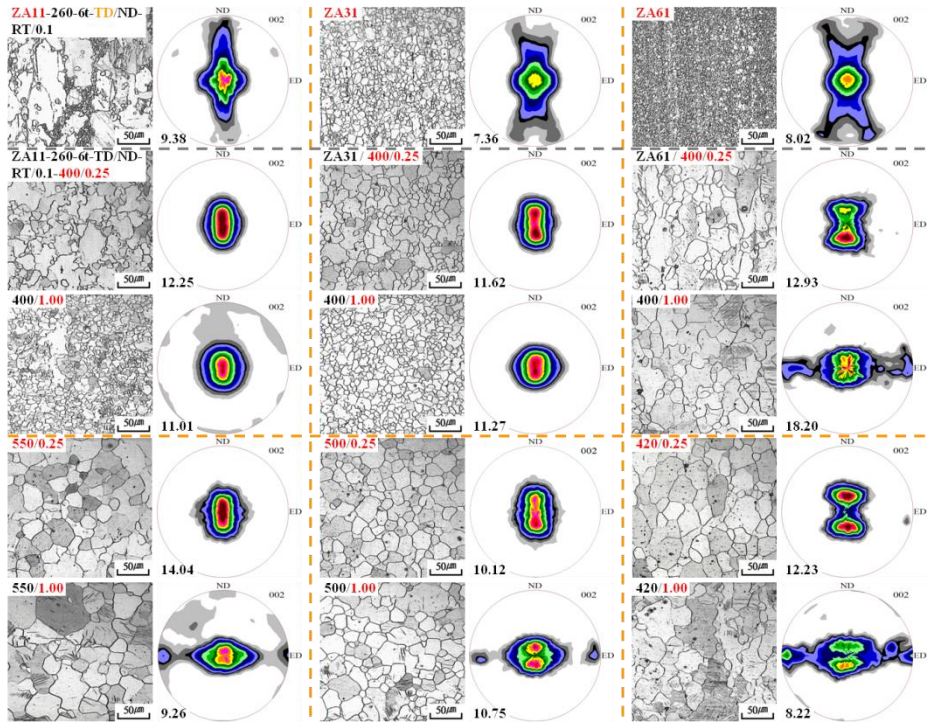


Figure 4.6 Microstructure and texture evolutions of extruded ZAx1 alloys during second step PSC above 400°C in two-step PSC (CA // TD).

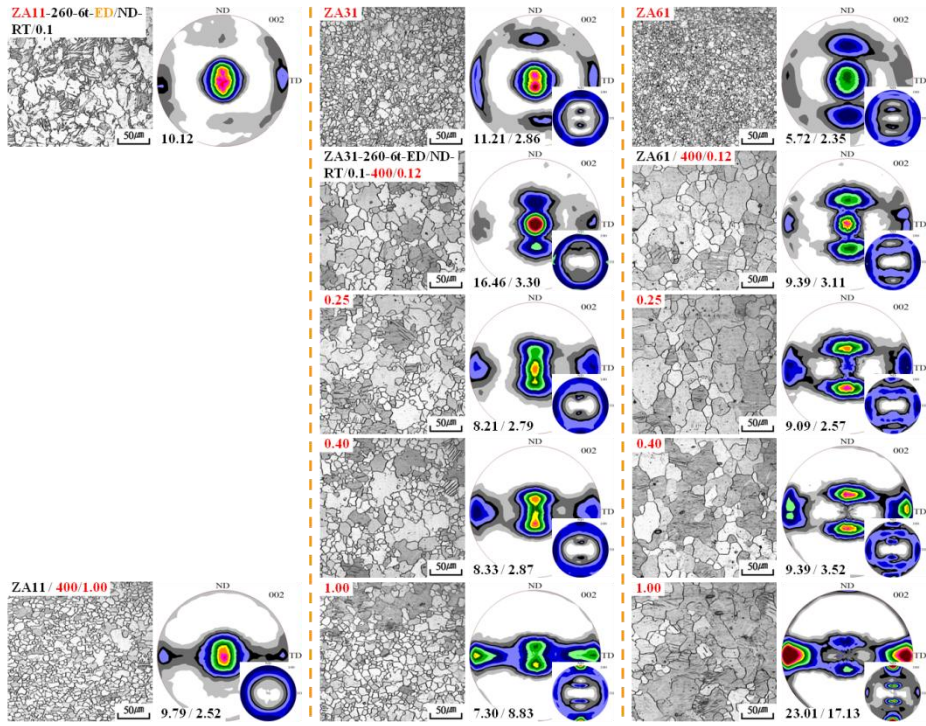


Figure 4.7 Microstructure and texture evolutions of extruded ZAx1 alloys during second step PSC at 400°C in two-step PSC (CA//ED).

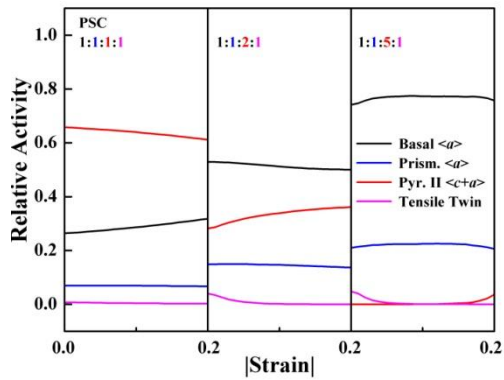
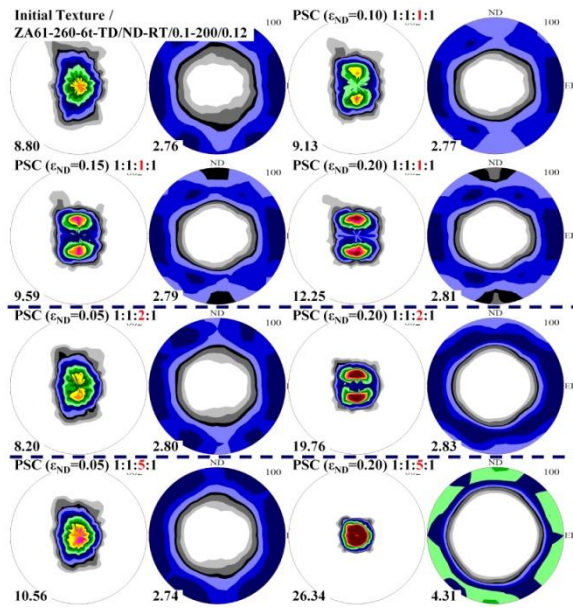


Figure 4.8 Theoretical deformation textures developed during PSC with different CRSS ratio; (initial texture) SP texture of ZA61-260-6t-TD/ND-RT/0.1-260/0.12, (1) 1:1:1:1, (2) 1:1:2:1 and (3) 1:1:5:1.

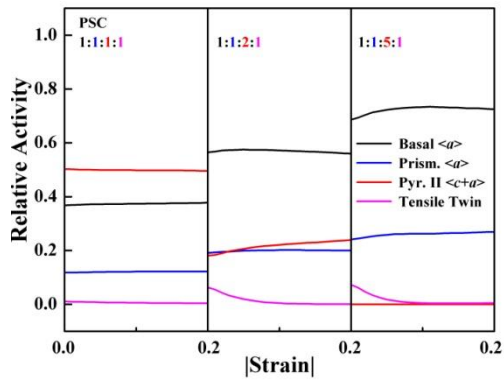
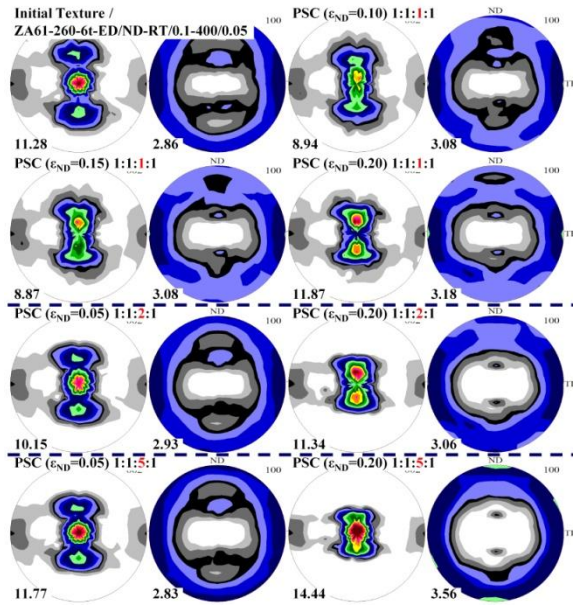


Figure 4.9 Theoretical deformation textures developed during PSC with different CRSS ratio; (initial texture) texture of ZA61-260-6t-ED/ND-RT/0.1-400/0.05, (1) 1:1:1:1, (2) 1:1:2:1 and (3) 1:1:5:1.

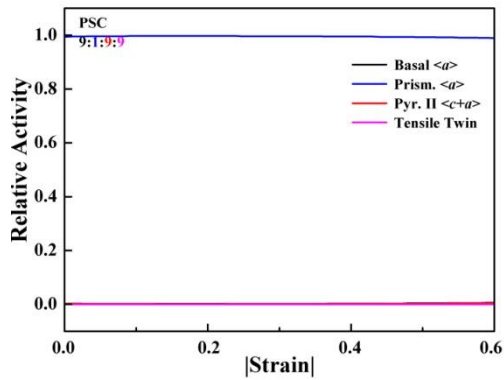
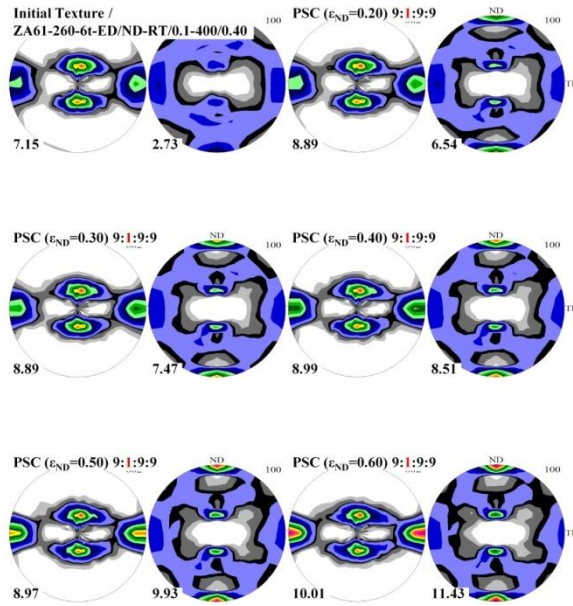


Figure 4.10 Theoretical deformation textures developed during PSC with CRSS ratio of 9:1:1:1; (initial texture) DP + CD texture of ZA61-260-6t-ED/ND-RT/0.1-400/0.40.

4.1.4 Effect of initial grain size on texture

Microstructures and textures of the annealed ZA61 alloys after the second step PSC at different temperatures (260 ~ 450°C) with initial strain rate of 0.0002 or 0.0400/sec in the two-step PSC (CA // TD) and two-step PSC (CA // ED) are represented in Figure 4.11 and 4.12 as follows;

In the two-step PSC (CA // TD) of the annealed ZA61 alloys,

260°C - DP - ($T_{DP, low}$) - SP - ($T_{DP, high}$) - DP - (T_{CD}) - DP + CD - 450°C

1. Initial grain size was 4 μm for the as-extruded ZA61 alloy, 14 μm for the 300°C-annealed one and 23 μm for the 450°C-annealed one.
2. At 260°C and 300°C with 0.0400/sec, with decrease in initial grain size, LD spread and tilt angle corresponding to the peak in DP texture increased as 10° for the 450°C-annealed ZA61 alloy, 15° for the 300°C-annealed one, 20° for the as-extruded one at 260°C, 0.0400/sec and 15° for the 450°C-annealed ZA61 alloy, 20° for the 300°C-annealed one, 20° for the as-extruded one at 260°C and 15° for the 450°C-annealed ZA61 alloy, 20° for the as-extruded one at 300°C, 0.0400/sec. And also fraction of the small DRXed grain region increased with decrease in initial grain size.
3. With increase in initial grain size, $T_{DP, low}$ increased as 260°C for the as-extruded ZA61 alloy and 300°C for the 450°C-annealed one.
4. At 300°C, SP texture with the fully DRXed microstructure was developed in the as-extruded ZA61 alloy but DP texture with the partially DRXed microstructure was developed in the 450°C-annealed one.
5. At 340°C with 0.0400/sec, SP texture with similar LD spread with the one in DP texture was developed in both as-extruded and 450°C-annealed

ZA61 alloys. However, the LD spread of the 450°C-annealed one was smaller than that of the as-extruded one with larger grain size.

6. With increase in initial grain size, T_{CD} decreased as 400°C for the as-extruded ZA61 alloy and 340°C for the 450°C-annealed one.

7. At 340°C and 380°C, SP texture was developed in the as-extruded ZA61 alloy. But the SP + weak CD texture with smaller LD spread was developed in the 450°C-annealed one with much larger grain size. And above 340°C, grain size increased with increase in initial grain size.

8. At 400°C, DP + weak CD texture was developed in the as-extruded ZA61 alloy. But strong TD texture with very weak DP texture was developed in the 450°C-annealed one with much larger grain size.

9. It seems important to sustain the grain size small to develop the DP texture and increase the fraction of the small grain region as fast as possible to increase the tilt angle corresponding to the peak. However, it seems important to grow enough to develop the CD texture because CD texture is developed after contraction of the LD spread performed by the basal slip.

10. In two-step PSC (CA // ED), similar textures were developed in both as-extruded and 450°C-annealed ZA61 alloys. Because they already had the weak CD texture before second step, formation process to make the CD texture didn't need and just strengthening process was progressed.

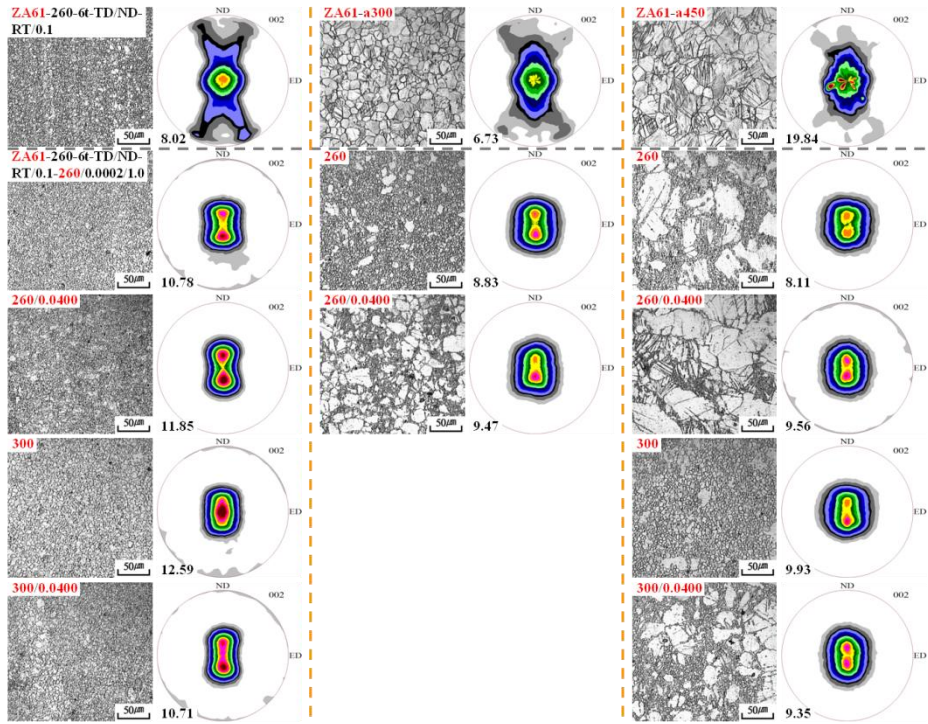


Figure 4.11 Microstructures and textures of annealed ZA61 alloys after second step PSC at different temperatures (260 ~ 450°C) with initial strain rate of 0.0002 or 0.0400/sec in two-step PSC (CA // TD).

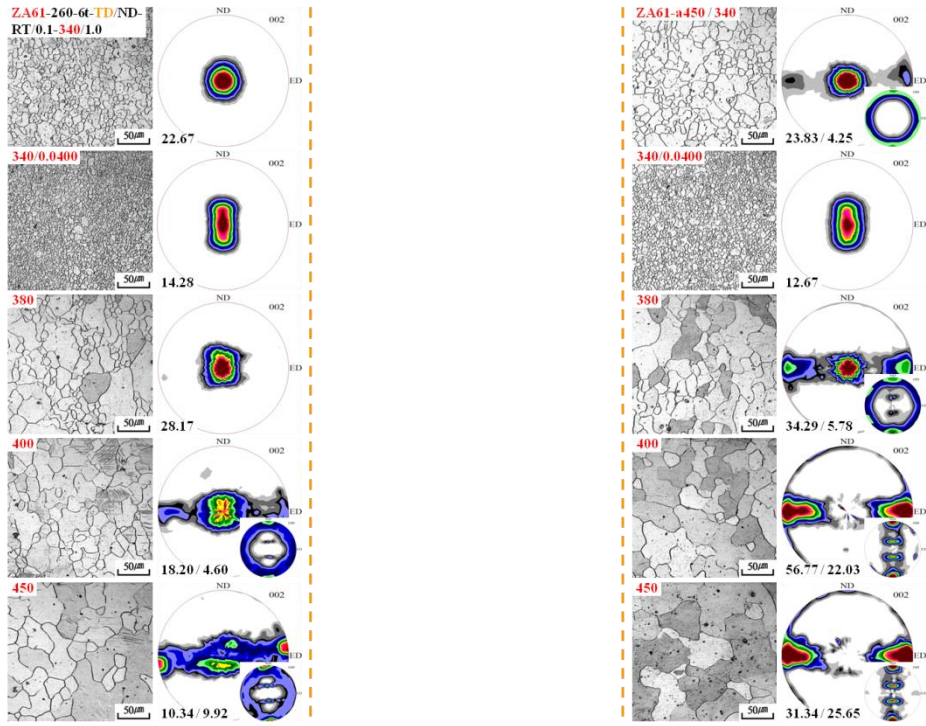


Figure 4.11 Continued.

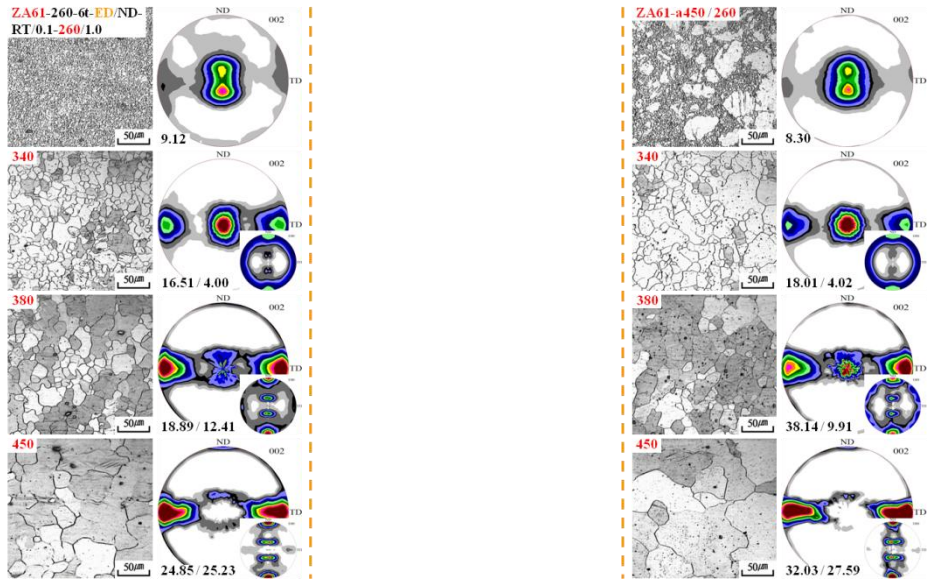


Figure 4.12 Microstructures and textures of annealed ZA61 alloys after second step PSC at different temperatures (260 ~ 450°C) in two-step PSC (CA // ED).

4.2 Two-step PSC of cast specimen

Microstructures and textures of the cast ZA alloys before the second step PSC in the two-step PSC are represented in Figure 4.13 as follows;

1. With increase in alloying content, initial grain size decreased as about 180 μm for the ZA31, 150 μm for the ZA61, 130 μm for the ZA61Ca1, 110 μm for the ZA19 and 100 μm for the ZA63 alloy.
2. After the first step PSC in the two-step PSC, SP texture with wide spread was developed with many twin boundaries inside the grains.
3. After the first step PSC and 90°-rotation on the CD in the two-step PSC (ROT), LD texture with no SP texture was prepared for the second step PSC in the two-step PSC (ROT).

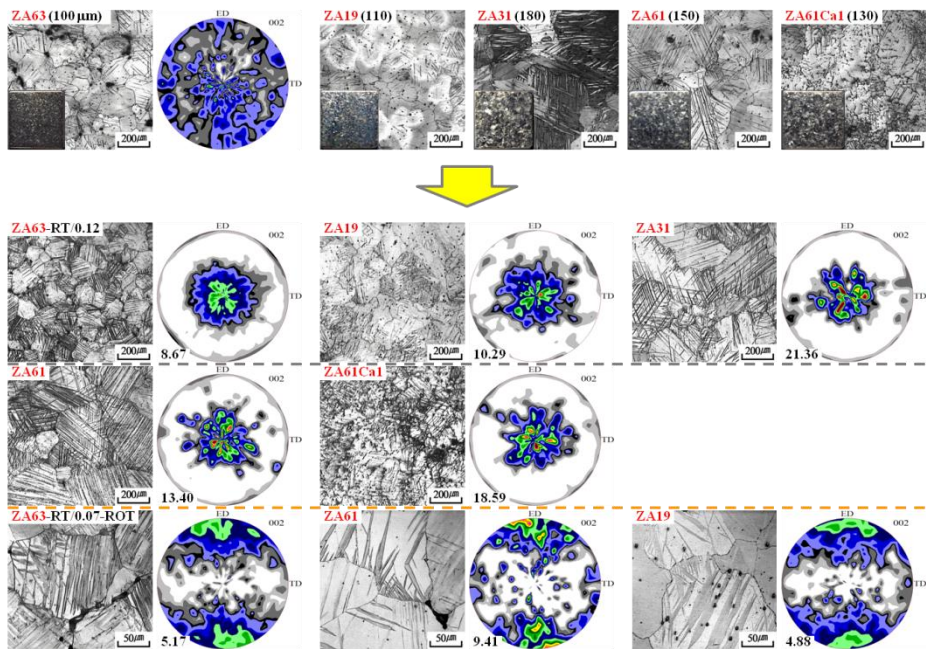


Figure 4.13 Microstructures and textures of cast ZA alloys before second step PSC in two-step PSC; (1) initial state and (2) after first step.

4.2.1 Two-step PSC

Microstructures and textures of the cast ZA alloys (ZA63, ZA19 and ZA31) after the second step PSC at different temperatures (300 ~ 500°C) in the two-step PSC are represented in Figure 4.14 as follows;

In the two-step PSC of the ZA63 and ZA19 alloys,

300°C - DP - ($T_{DP, low}$) - SP - (T_{CD}) - SP + CD - ($T_{DP, high}$) - DP + CD - 500°C

In the two-step PSC of the ZA31 alloy,

260°C - DP - (T_{CD}) - DP + CD - 400°C

1. At low temperature, DP texture was developed with the partially DRXed fine microstructure developed by NRX.
2. At mid temperature, SP texture was developed with the fully DRXed coarse microstructure developed by NRX and grain growth.
3. At high temperature, weak DP + strong CD texture (DP and $\{11-20\} <1-100>$ texture) was developed with large grains occurred by ordinary DRX.
4. DP texture was sustained until the partially DRXed fine microstructure was sustained. And the SP texture was developed with the fully DRXed coarse microstructure.
5. Initial grain size (110 μm) of the ZA19 alloys was larger than that (100 μm) of the ZA63 alloy.
6. Solidus temperature (455°C) of the ZA19 alloys was higher than that (363°C) of the ZA63 alloy.
7. $T_{DP, low}$ increased as 310°C for the ZA63 and 360°C for the ZA19 because of retarded DRX process originated from larger initial grain size and higher solidus temperature of the ZA19 alloy than those of the ZA63 alloy.
8. Tilt angle corresponding to the peak in DP texture developed at low tem-

perature decreased as 20° for the ZA63, 20° for the ZA19 and 15° for the ZA31 at 300°C.

9. T_{CD} increased as 390°C for the ZA63 and 500°C for the ZA19 alloy.

10. $T_{DP, high}$ increased as 400°C for the ZA63 and 500°C for the ZA19 alloy.

11. Tilt angle corresponding to the peak in DP texture developed at high temperature decreased as 25° for the ZA63 at 450°C, 20° for the ZA19 at 500°C and 15° for the ZA31 at 500°C.

12. In the two-step PSC of the ZA31 alloy, relatively slight changes in texture and microstructure occurred because of retarded DRX process originated from large initial grain size (180 μm) and high solidus temperature (520°C). DP texture was sustained and relatively weaker CD texture was developed at high temperature, which was relatively similar with one developed at low temperature.

13. It seems that $T_{DP, low}$ reflects the ability to retard the DRX process, which is ability to sustain the small grain size. And large initial grain size and high solidus temperature may be able to retard the DRX process. On the contrary, it seems that T_{CD} reflects the ability to promote grain growth, which is ability to grow the CD grains. And grain growth rate increases with decrease in solidus temperature. And it seems that $T_{DP, high}$ decreases with decrease in solidus temperature.

Microstructure and texture evolutions of the cast ZA63 alloys during the second step PSC at 300, 320 and 450°C in the two-step PSC are represented in Figure 4.15 and 4.16 as follows;

1. (At 300°C) at initial stage, SP split into DP with development of the partially DRXed fine microstructure by NRX.

2. (At 320°C) at initial stage, SP split into DP with development of the partially DRXed fine microstructure by NRX. Then the DP disappeared and the

DP texture was changed into the SP texture (similar LD spread with one of the DP texture) with the fully DRXed microstructure.

3. (At 450°C) at initial stage, SP split into DP. Then CD texture strengthened instead of weakening of the DP texture with grain growth.

4. (At 450°C with 0.4000/sec) throughout the whole process, SP texture strengthened and some LD texture ($\langle 0001 \rangle$ //LD texture) occurred.

5. (At 450°C) with decrease in strain rate, CD texture strengthened instead of weakening of the SP texture.

Microstructures and textures of the cast ZA63 alloys after the second step PSC at 320 or 400°C with different strain rates in the two-step PSC are represented in Figure 4.17 as follows;

1. Effect of increase in strain rate was similar to effect of decrease in temperature because flow stress increased and grain size decreased with increase in strain rate, similarly.

2. DP texture was sustained until the partially DRXed fine microstructure was sustained. And SP texture was developed with the fully DRXed coarse microstructure.

(Case 1) At 320°C, SP texture was developed at 0.0002/sec with the fully DRXed microstructure but DP texture was developed at 0.0400 and 0.0800/sec (similar flow stress with one at 230°C) with the partially DRXed fine microstructure.

(Case 2) At 400°C, weak DP + strong CD texture was developed at 0.0002/sec with the coarse microstructure but strong SP + weak LD texture was developed at 0.4000 and 0.8000/sec (similar flow stress with one at 260°C) with the coarse microstructure.

3. Besides large flow stress, it seems necessary to sustain the grain size small to develop the DP texture.

4. As shown in Figure 4.18 and 4.19, large remained parent grains showed the strong texture whose basal poles were aligned relatively close to the CA. However, small DRXed grains showed the broad LD spread with weak intensity.

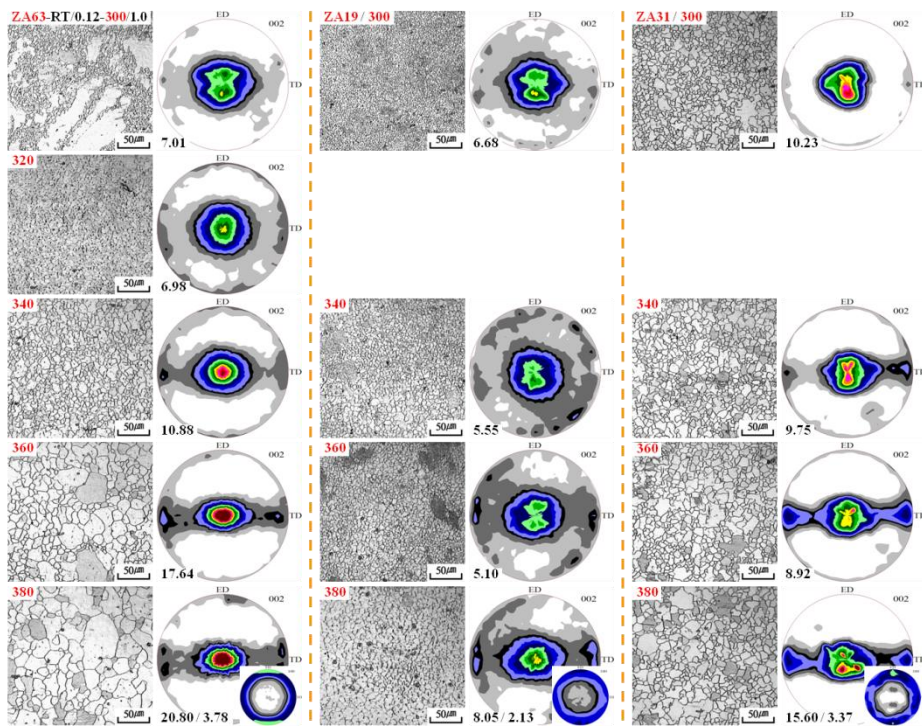


Figure 4.14 Microstructures and textures of cast ZA alloys after second step PSC at different temperatures (300 ~ 500°C) in two-step PSC; (1) ZA63, (2) ZA19 and (3) ZA31 alloys.

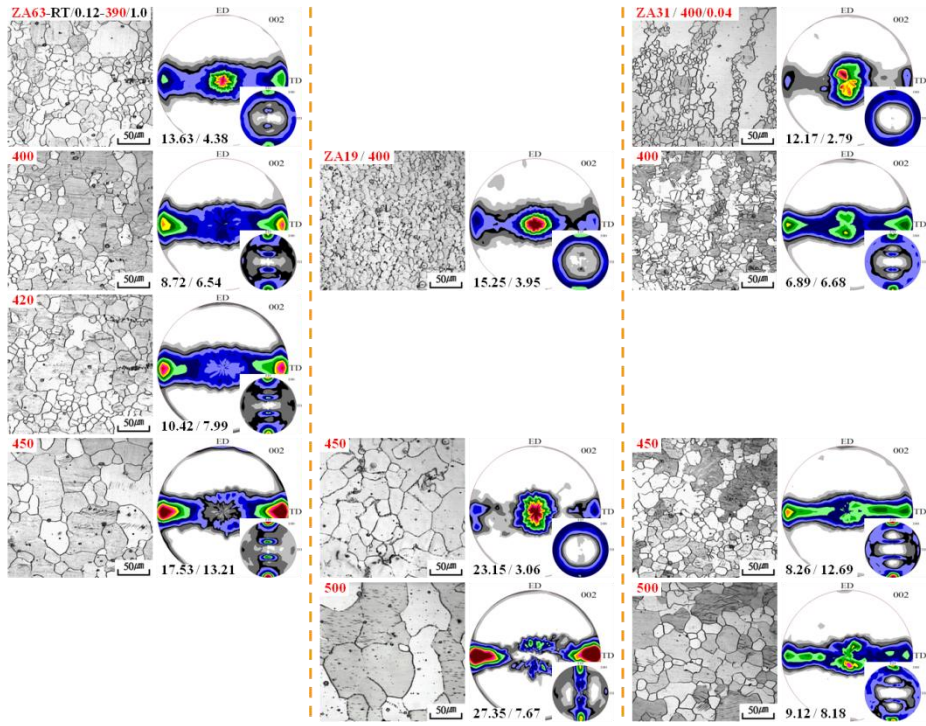


Figure 4.14 Continued.

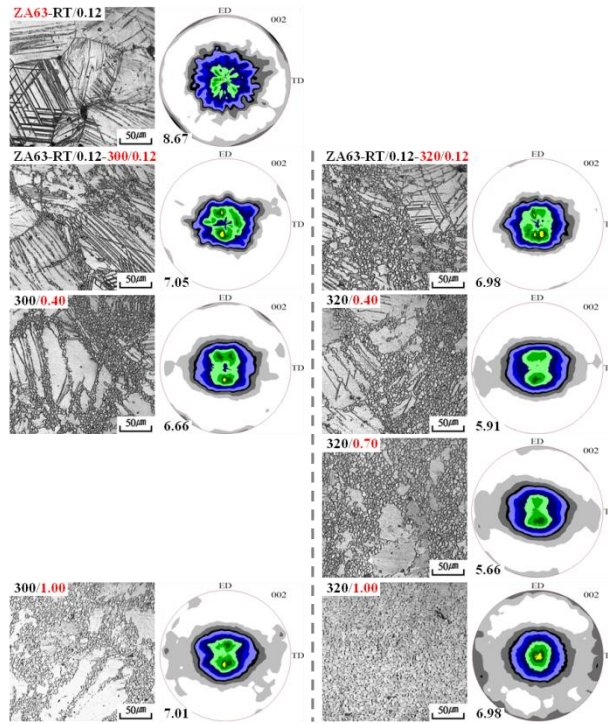


Figure 4.15 Microstructure and texture evolutions of cast ZA63 alloys during second step PSC at 300 or 320°C in two-step PSC.

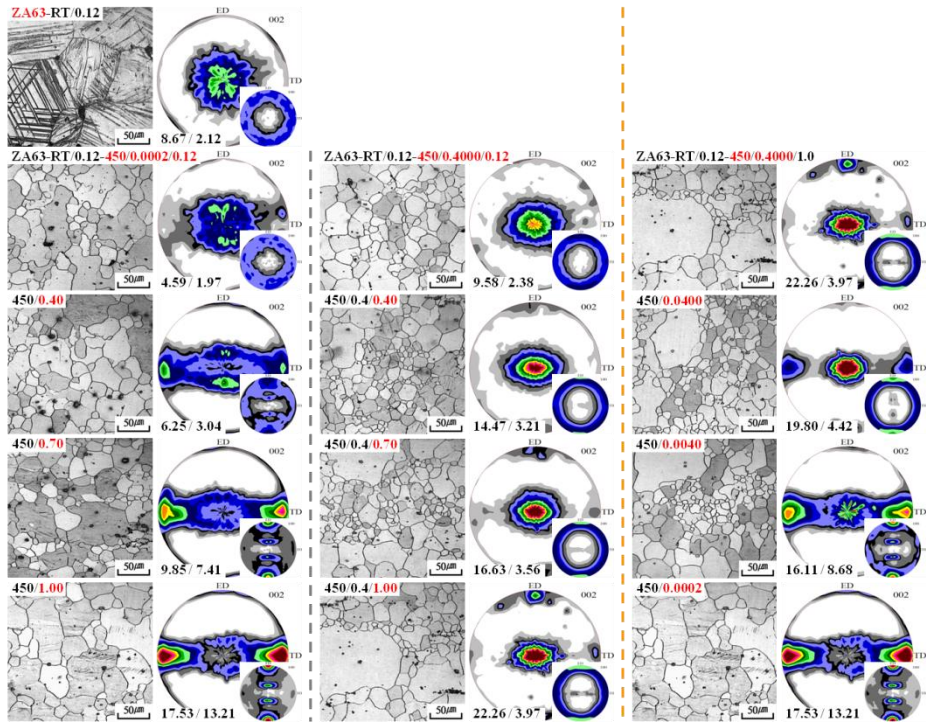


Figure 4.16 Microstructure and texture evolutions of cast ZA63 alloys during second step PSC at 450°C with different strain rates in two-step PSC; (1) 0.0002/sec, (2) 0.4000/sec and (3) different strain rates.

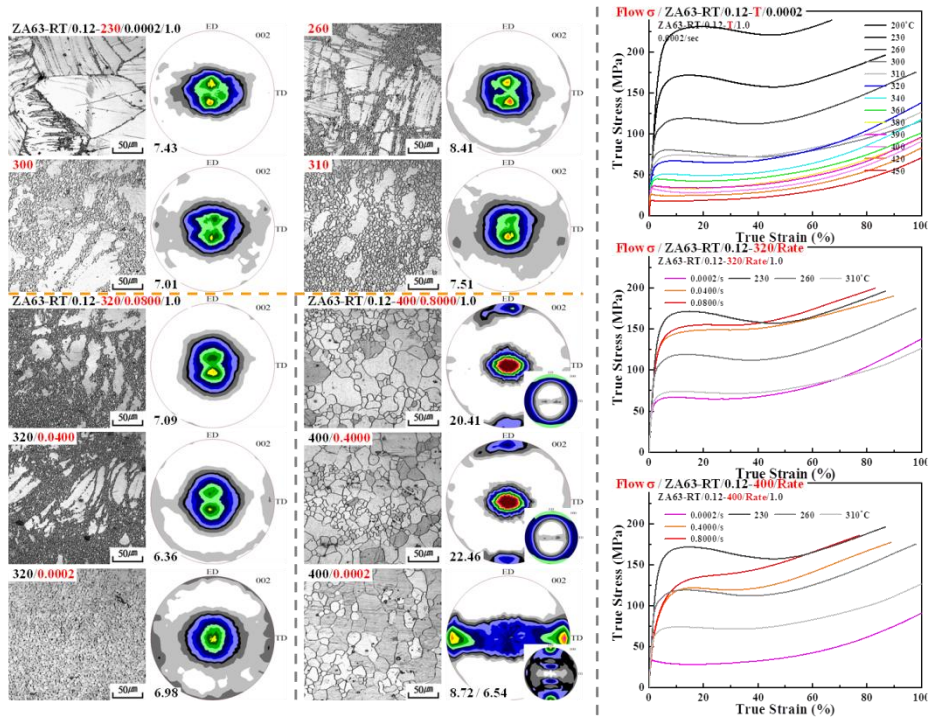


Figure 4.17 Microstructures and textures of cast ZA63 alloys after second step PSC at 320 or 400°C with different strain rates in two-step PSC; (1) two-step PSC at 230 ~ 310°C, (2) 320°C, (3) 400°C and (4) flow stress.

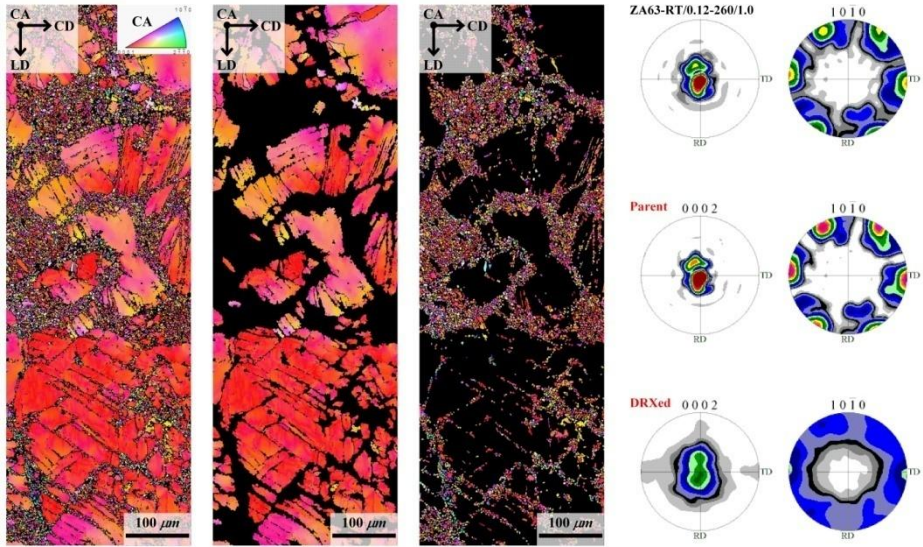


Figure 4.18 Texture of cast ZA63 alloy after second step PSC at 260°C with 0.0002/sec in two-step PSC.

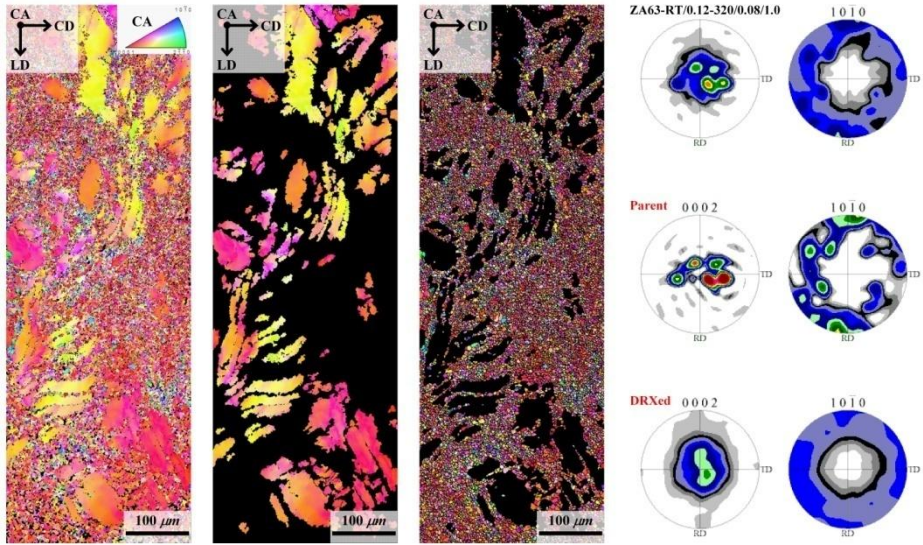


Figure 4.19 Texture of cast ZA63 alloy after second step PSC at 320°C with 0.0800/sec in two-step PSC.

4.2.2 Two-step PSC (ROT)

Microstructures and textures of the cast ZA63 alloys after the one-step PSC at different temperatures (300 ~ 450°C) with 0.0002 or 0.4000/sec and the two-step PSC (ROT) at different temperatures (300 ~ 400°C) are represented in Figure 4.20 as follows;

In the one-step PSC of the ZA63 alloy with 0.0002/sec,

300°C - DP - 340°C - SP - SP + CD - 380°C - DP + CD - 450°C

In the one-step PSC of the ZA63 alloy with 0.4000/sec,

340°C - DP - 360°C - SP + LD - SP + LD + CD - 450°C

In the two-step PSC (ROT) of the ZA63 alloy,

300°C - DP - 340°C - SP + LD - 370°C - DP + LD + CD - 390°C - DP + CD - 400°C

1. As shown in Figure 4.21, SP texture and LD texture strengthened throughout the whole one-step PSC (0.4000/sec) of the ZA63 alloys at 400°C. And both SP and LD grains grew during the whole process as shown in Figure 4.22. It seems that the strengthening of SP and LD texture results from the deformation and grain growth.

2. In the one-step PSC (0.4000/sec) of the ZA63 alloy, intensity of the LD texture increased with increase in temperature and it was maximized at 380°C and then it decreased with increase in temperature.

3. In the one-step PSC (0.4000/sec) of the ZA63 alloy at 400 and 450°C, LD texture strengthened instead of weakening of CD texture with increase in strain rate. However, intensity of the LD texture decreased instead of increase in intensity of the CD texture with increase in temperature.

4. In the two-step PSC (ROT) of the ZA63 alloy, intensity of the LD texture increased with increase temperature and it was maximized at 360°C and then

it decreased with increase in temperature.

5. In the two-step PSC (ROT) of the ZA63 alloy, intensity of the LD texture decreased instead of increase in intensity of the CD texture with increase temperature above 360°C.

In the two-step PSC (ROT) of the ZA alloys as shown in Figure 4.23,

300°C - DP - ($T_{LD, begin}$) - SP + LD - (T_{CD}) - DP + LD + CD - ($T_{LD, end}$) - DP
+ CD - 450°C

1. In the two-step PSC (ROT), intensity of the LD texture increased with decrease in solidus temperature (363°C for the ZA63, 400°C for the ZA61 and 455°C for the ZA19 alloy).

2. In the one-step PSC (0.4000/sec) at 400°C, intensity of the LD texture increased with decrease in solidus temperature (363°C for the ZA63, 400°C for the ZA61 and 455°C for the ZA19 alloy).

3. In the two-step PSC (ROT), $T_{LD, begin}$ increased as 320°C for the ZA61, 340°C for the ZA63 and 380°C for the ZA19 alloy.

4. In the two-step PSC (ROT), $T_{LD, end}$ increased as 370°C for the ZA61, 390°C for the ZA63 and 420°C for the ZA19 alloy.

5. In the two-step PSC (ROT), T_{CD} increased as 360°C for the ZA61, 370°C for the ZA63 and 380°C for the ZA19 alloy.

6. Grain size increased in the order of ZA19, ZA63 and ZA61.

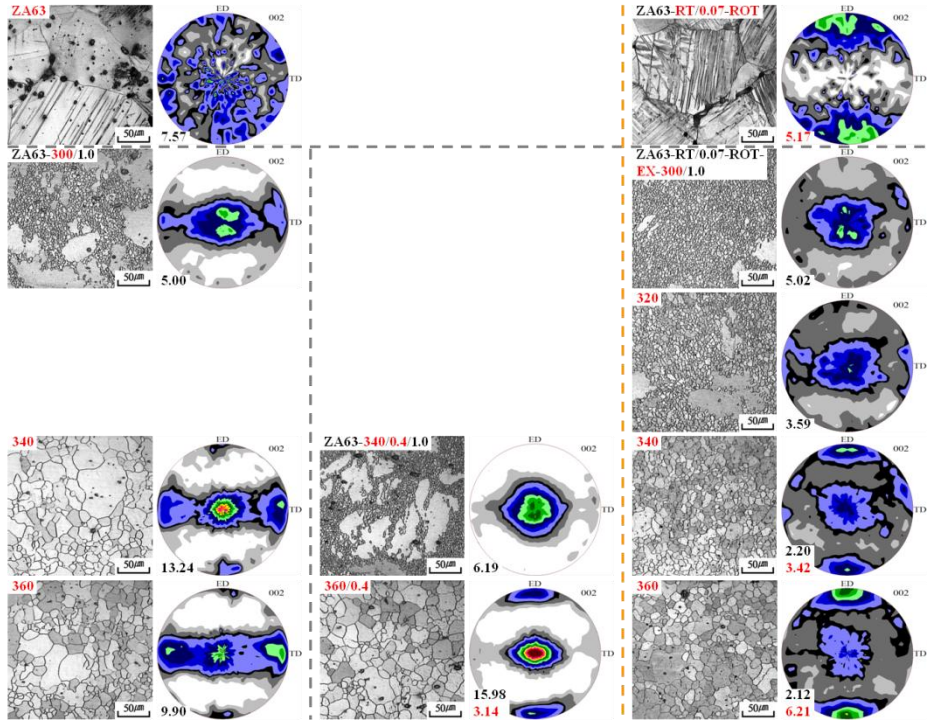


Figure 4.20 Microstructures and textures of cast ZA63 alloys after PSC at different temperatures (300 ~ 450°C); (1) one-step PSC with 0.0002/sec, (2) one-step PSC with 0.4000/sec and (3) two-step PSC (ROT).

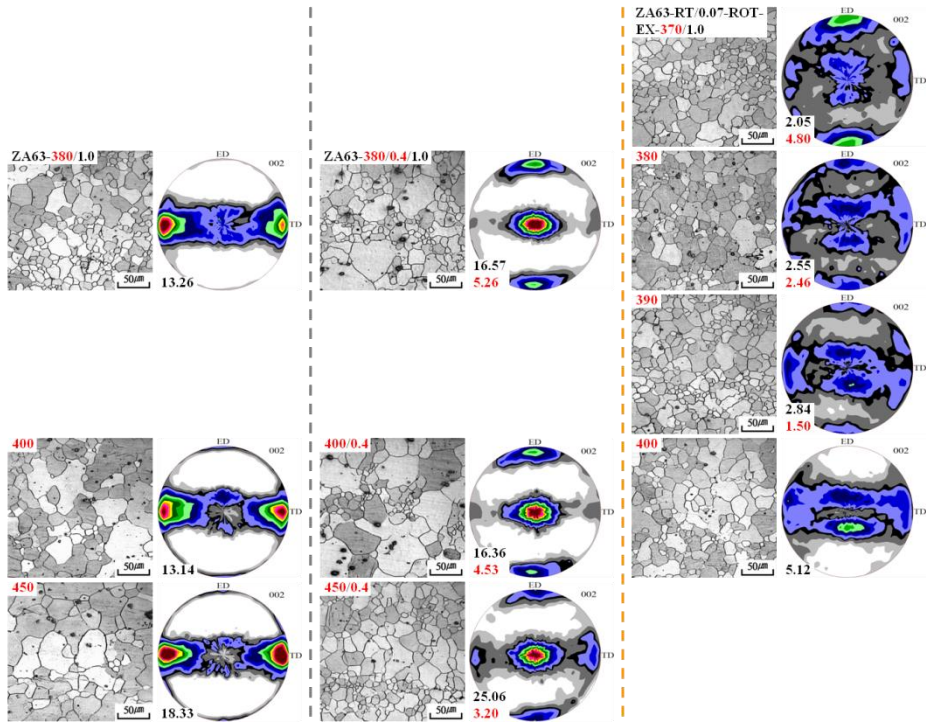


Figure 4.20 Continued.

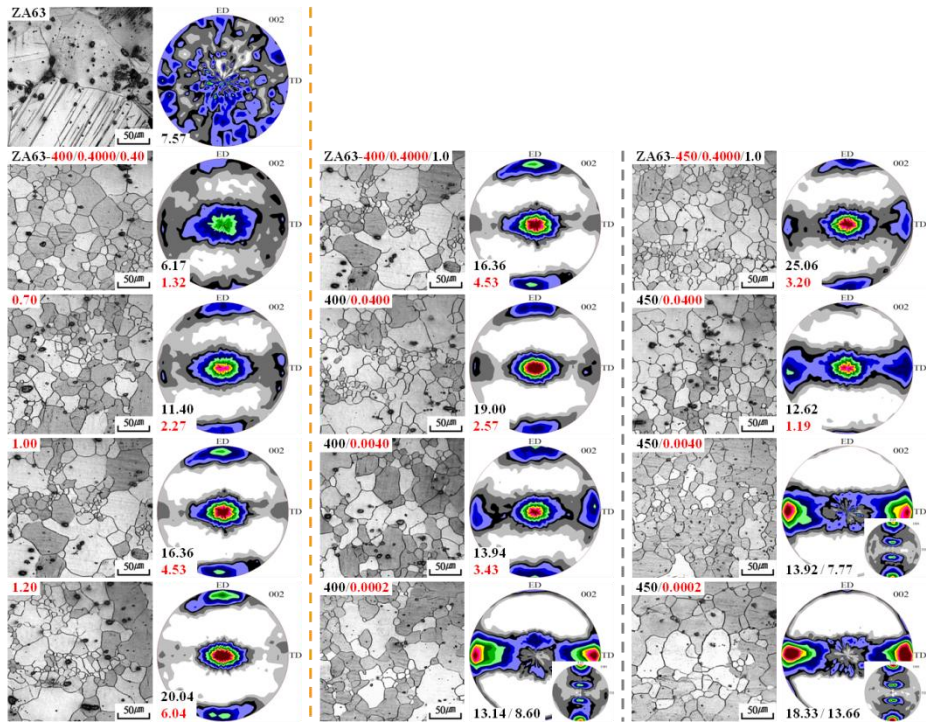


Figure 4.21 Microstructures and textures of cast ZA63 alloys after one-step PSC at 400 or 450°C with different strain rates (0.0002 ~ 0.4000/sec); (1) evolution at 400°C with 0.4000/sec, (2) 400°C and (3) 450°C.

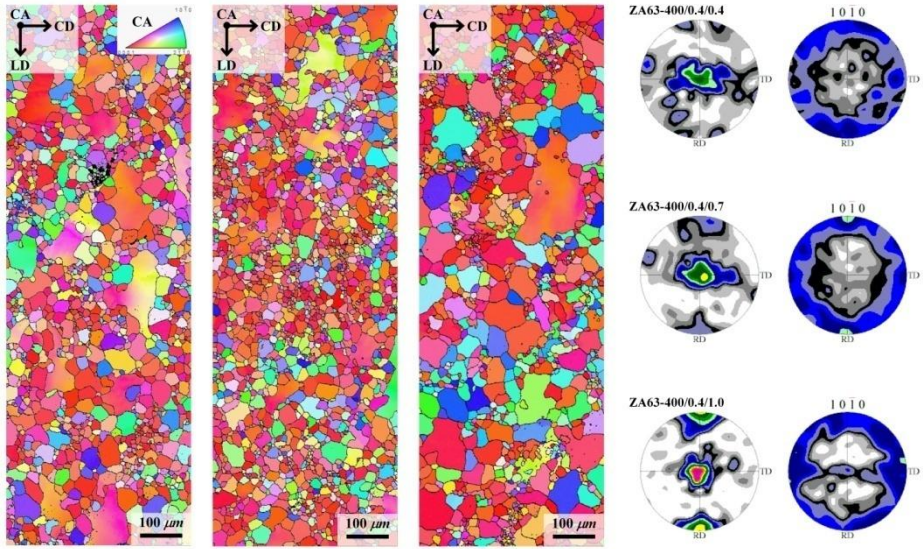


Figure 4.22 Texture evolution of cast ZA63 alloy during one-step PSC at 400°C with 0.4000/sec.

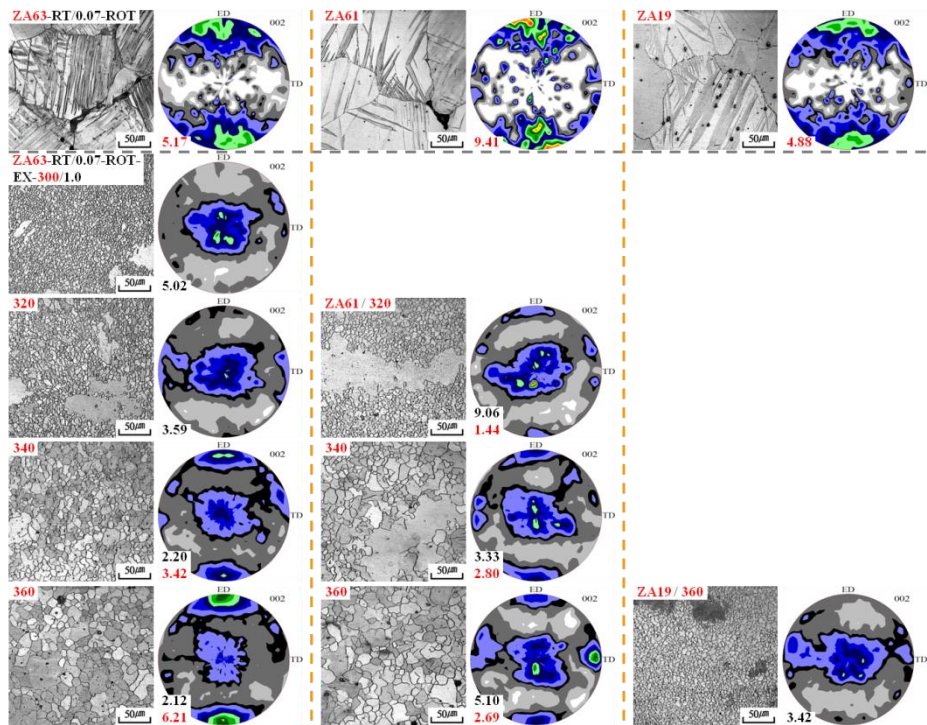


Figure 4.23 Microstructures and textures of cast ZA alloys after second step PSC at different temperatures (300 ~ 450°C) in two-step PSC (ROT); (1) ZA63, (2) ZA61 and (3) ZA19 alloys.

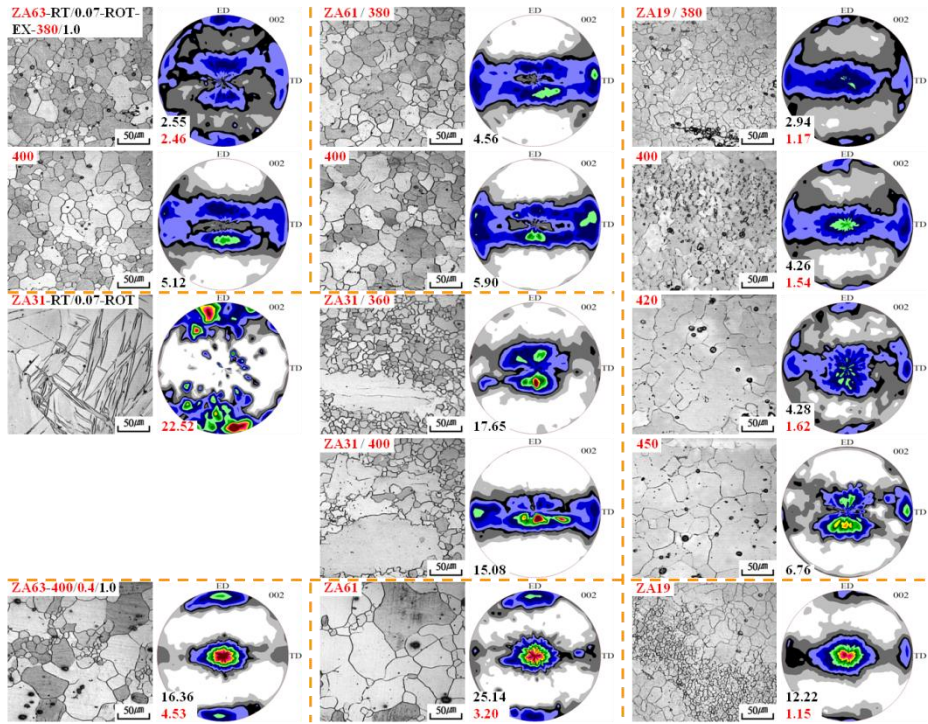


Figure 4.23 Continued; (4) ZA31 alloys and (5) one-step PSC at 400°C with 0.4000/sec.

4.2.3 Effect of Ca on texture

Figure 4.24 shows the microstructures and textures of the cast ZA61Ca1 alloys after the second step PSC at different temperatures (260 ~ 400°C) in the two-step PSC as follows;

In the two-step PSC of the ZA61 alloy,

300°C - DP - ($T_{DP, low}$) - SP - (T_{CD}) - SP + CD - ($T_{DP, high}$) - DP + CD - 450°C

In the two-step PSC of the ZA61Ca1 and ZA31 alloys,

260°C - DP - (T_{CD}) - DP + CD - 400°C

1. With addition of Ca, intensity of CD texture increased.
2. With addition of Ca, T_{CD} decreased as 380°C for the ZA61 and 340°C for the ZA61Ca1 alloy.
3. Addition of Ca retarded the grain growth and promoted the development of the DP and CD textures.

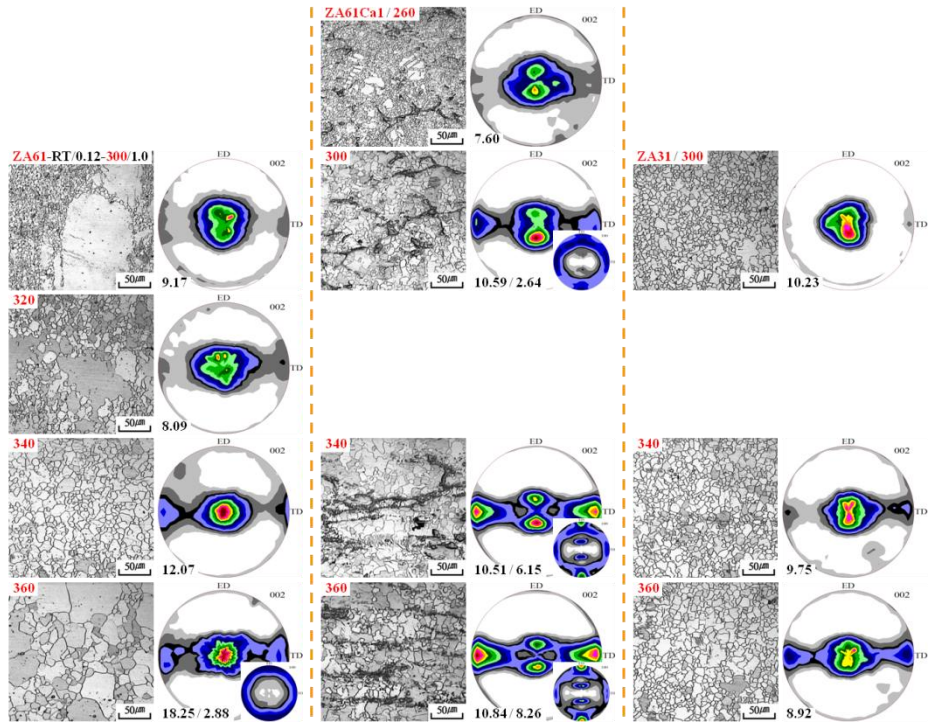


Figure 4.24 Microstructures and textures of cast ZA61Ca1 alloys after second step PSC at different temperatures (260 ~ 400°C) in two-step PSC; (1) ZA61, (2) ZA61Ca1 and (3) ZA31 alloys.

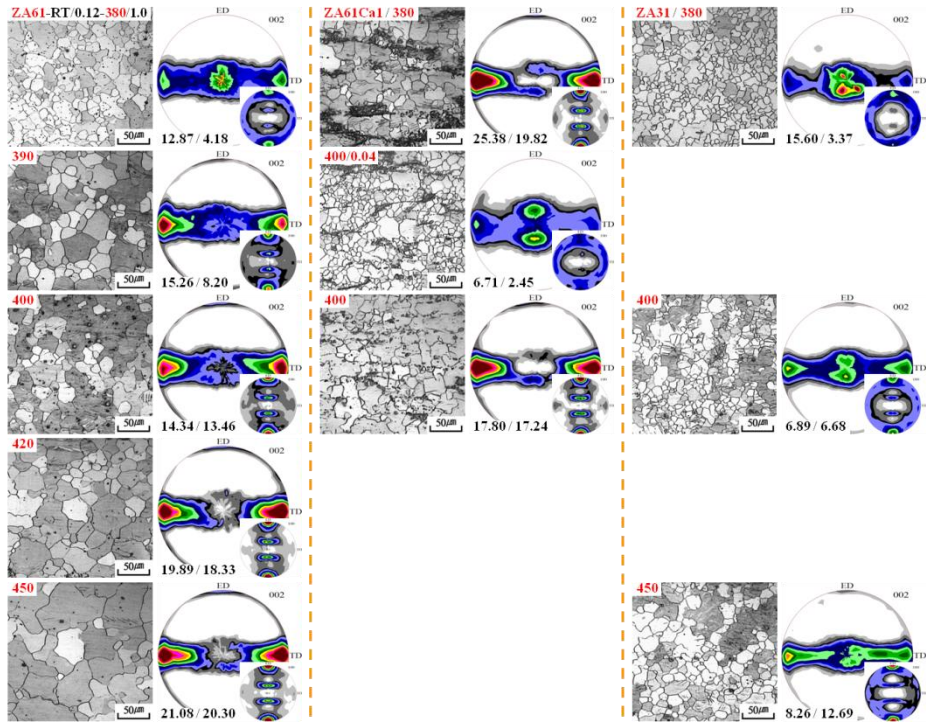


Figure 4.24 Continued.

4.3 Summary

PSC texture results were summarized in Figure 4.25 ~ 4.28. And the texture development mechanisms were summarized as a flow chart in Figure 4.29.

Effects of Zn content and initial grain size on DP texture developed at low temperature in the two-step PSC (CA // TD) were compared in Figure 4.25 as follows;

(Case 1) Initial grain size before second step PSC decreased as 25 μm for the ZA11, 8 μm for the ZA31 and 4 μm for the ZA61 alloy.

(Case 2) Initial grain size before second step PSC decreased as 23 μm for the 450°C-annealed ZA61 alloy, 14 μm for the 300°C-annealed one and 4 μm for the as-extruded one.

1. In both cases, with decrease in initial grain size, LD spread and tilt angle corresponding to the peak in DP texture increased.

2. At 300°C where SP texture was developed in the as-extruded ZA61 alloy, DP textures were developed in the 450°C-annealed ZA61 and ZA11 alloys.

These phenomena can be explained from the viewpoint of the grain-size dependant compatibility deformation. Because small grains are more favorable to deform by the pyramidal II $\langle c+a \rangle$ slip by aid of the compatibility stress, DP texture which can be developed by activation of the pyramidal II $\langle c+a \rangle$ slip is developed at low temperature where the grain size is small enough. Because initial grain boundary acts as nucleation site, fraction of the small DRXed grain region increases with decrease in initial grain size. Therefore, fraction of the DP texture region increases with decrease in initial grain size.

At 300°C, fully DRXed microstructure was developed in the as-extruded ZA61 alloy but still partially DRXed microstructures were developed in the 450°C-annealed ZA61 and ZA11 alloys. It seems that in the as-extruded ZA61 alloy, at 300°C, the NRX was completed at the early strain and NRXed grains began to grow during the continuing PSC with strengthening of the SP texture. However, at 340°C where grain growth occurred actively, grain size in the 450°C-annealed ZA61 alloy was larger than that in as-extruded one. Therefore, LD spread of SP texture in the 450°C-annealed one was narrower than that in as-extruded one by higher activity of the basal slip resulted from larger grain size.

Eventually, it seems important to retard the DRX process in order to develop the DP texture even at higher temperature. However, in order to increase the LD spread and tilt angle corresponding to the peak in DP texture at low temperature, it seems important to increase the fraction of small DRXed grain region and restrict their growth.

Effects of the Zn content on DP textures developed at high temperature in the two-step PSC (CA // TD) or (CA // ED) were summarized in Figure 4.26 as follows;

1. With increase in Zn content, LD spread and tilt angle corresponding to the peak in DP texture increased.
2. With increase in Zn content, $T_{DP, high}$ (temperature where DP texture began to be developed) decreased as shown in Figure 4.21.

These phenomena can be explained from the viewpoint of the thermal activation of the cross-slip. With increase in Zn content, solidus temperature decreases and inversely, homologous temperature increases. With increase in homologous temperature, activity of the pyramidal II $\langle c+a \rangle$ slip can be enhanced by aid of the increased thermal stress.

Effects of the alloying content on the intensities of CD and LD textures were summarized in Figure 4.28 as follows;

1. Solidus temperature decreases as 594°C for the ZA11, 520°C for the ZA31, 455°C for the ZA19, 400°C for the ZA61 and 363°C for the ZA63 alloy with increase in Zn or Al content.

2. With decrease in solidus temperature, intensities of the CD and LD textures increased.

3. With decrease in solidus temperature, T_{CD} and $T_{LD, \text{begin}}$ (temperature where CD or LD texture began to be developed) decreased as shown in Figure 4.27.

4. With addition of Ca in the ZA61 alloy, T_{CD} decreased at about 40°C but maximum intensity of the CD texture was similar with that of ZA61 alloy.

5. With decrease in solidus temperature, grain size developed at high temperature (above 340°C) increased.

6. Even though the solidus temperature of the ZA61 was higher than that of the ZA63 alloy, T_{CD} and $T_{LD, \text{begin}}$ of the ZA61 were lower than those of the ZA63 alloy and the grain size of the ZA61 was larger than that of the ZA63 alloy.

7. In the ZA11 or ZA31 alloy whose initial grain size was large and solidus temperature was high, changes in texture and microstructure were relatively insignificant than those of the ZA61 or ZA63 alloy which had small initial grain size and low solidus temperature.

These phenomena can be explained from the viewpoint of the thermal activation of the cross-slip. Theoretically, CD texture can be developed by the activation of the prismatic $\langle a \rangle$ slip and LD texture can be developed at the condition where the tensile twin is deactivated and the pyramidal II $\langle c+a \rangle$ slip is activated. With decrease in solidus temperature, homologous tempera-

ture increases. With increase in homologous temperature, activity of the non-basal slip can be enhanced by aid of the increased thermal stress.

Additionally, with increase in temperature, DRXed grains began to grow. Therefore, with increase in grain growth rate, DRXed texture can strengthen. Reversed tendency between ZA61 and ZA63 alloys might result from faster growth of the DRXed grains in the ZA61 alloy.

Based on these discussions, extrusion texture development process was summarized as a flow chart in Figure 4.29 as follows;

(Main factor) (1) Zn and Al content, (2) temperature, (3) Ca addition, (4) rate

(Key mechanism) (1) grain-size dependant compatibility deformation, (2) introduction of homologous temperature based on thermal activation of the cross-slip

1. With increase in Zn and Al content, solidus temperature decreases, inversely, homologous temperature increases. With increase in homologous temperature, activity of the non-basal slip can be enhanced by aid of the increased thermal stress and transition temperature (twin to $\langle c+a \rangle$ slip) can be lowered. These phenomena can result in increase in tilt angle corresponding to the peak in DP texture or occurrence of ED texture.

2. With increase in Zn and Al content, initial grain size decreases. With decrease in initial grain size, fraction of the small NRXed grains increases because initial grain boundary acts as a nucleation site. This phenomenon can result in increase in ED spread in DP texture.

3. Grain growth can be retarded by strong interaction between Ca and grain boundary originated from large atomic size of Ca. This phenomenon can result in development of DP texture even at relatively high temperature.

4. Strong interaction between Ca and basal dislocation (usually, occurred as

first mode during deformation) can reduce activity of the basal slip and enhance activity of the non-basal slip. This phenomenon can result in weakening of basal texture.

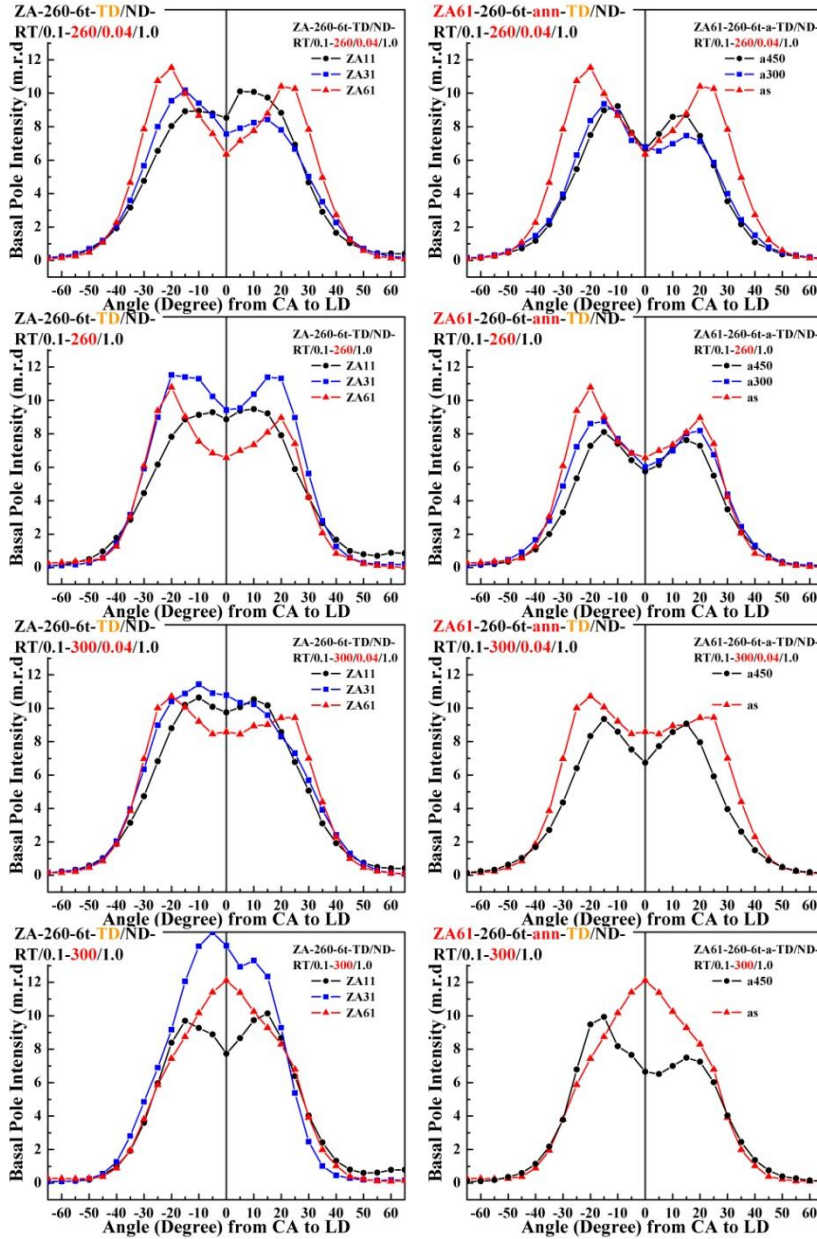


Figure 4.25 Summary; comparison between effects of (1) Zn content and (2) initial grain size on DP texture (two-step PSC (CA // TD)) developed at low temperature.

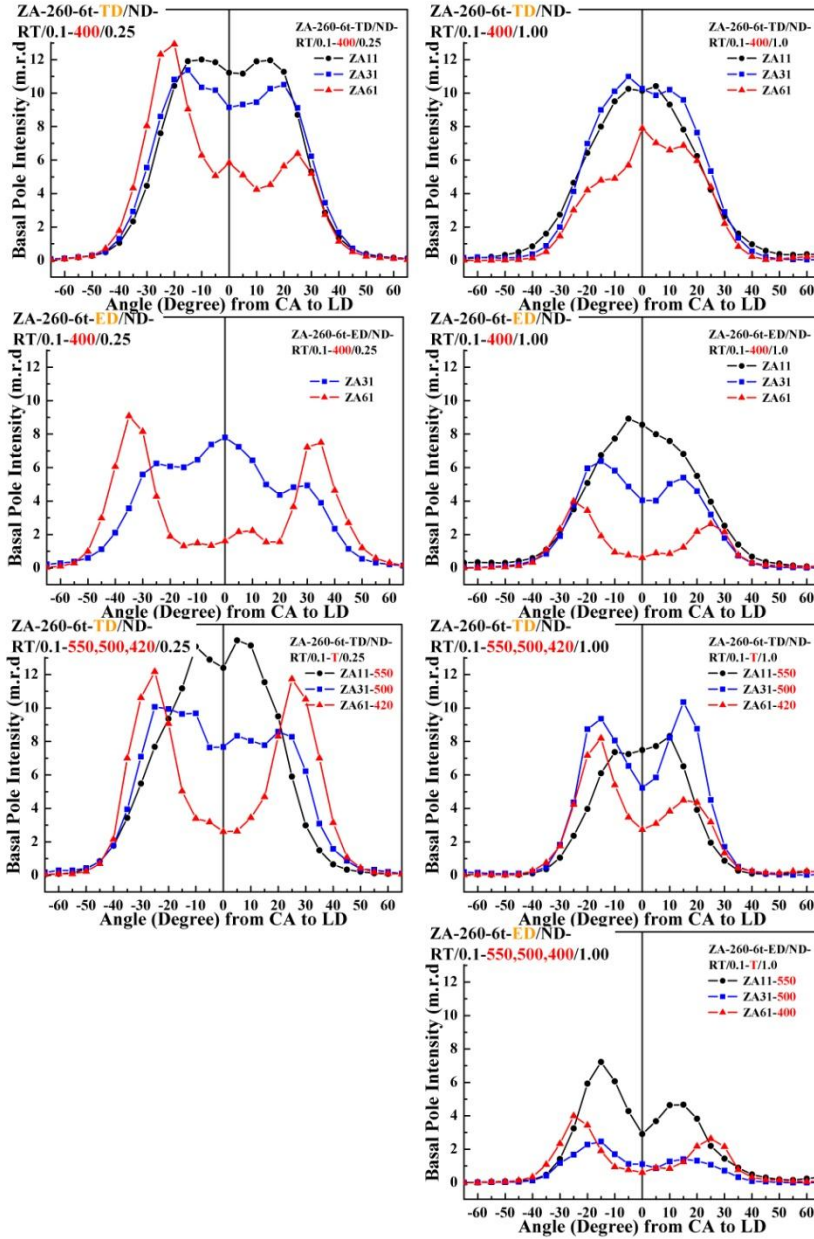


Figure 4.26 Summary; analysis on effects of Zn content on DP texture (two-step PSC (CA // TD) or (CA // ED)) developed at high temperature based on effects of Zn content on solidus temperature.

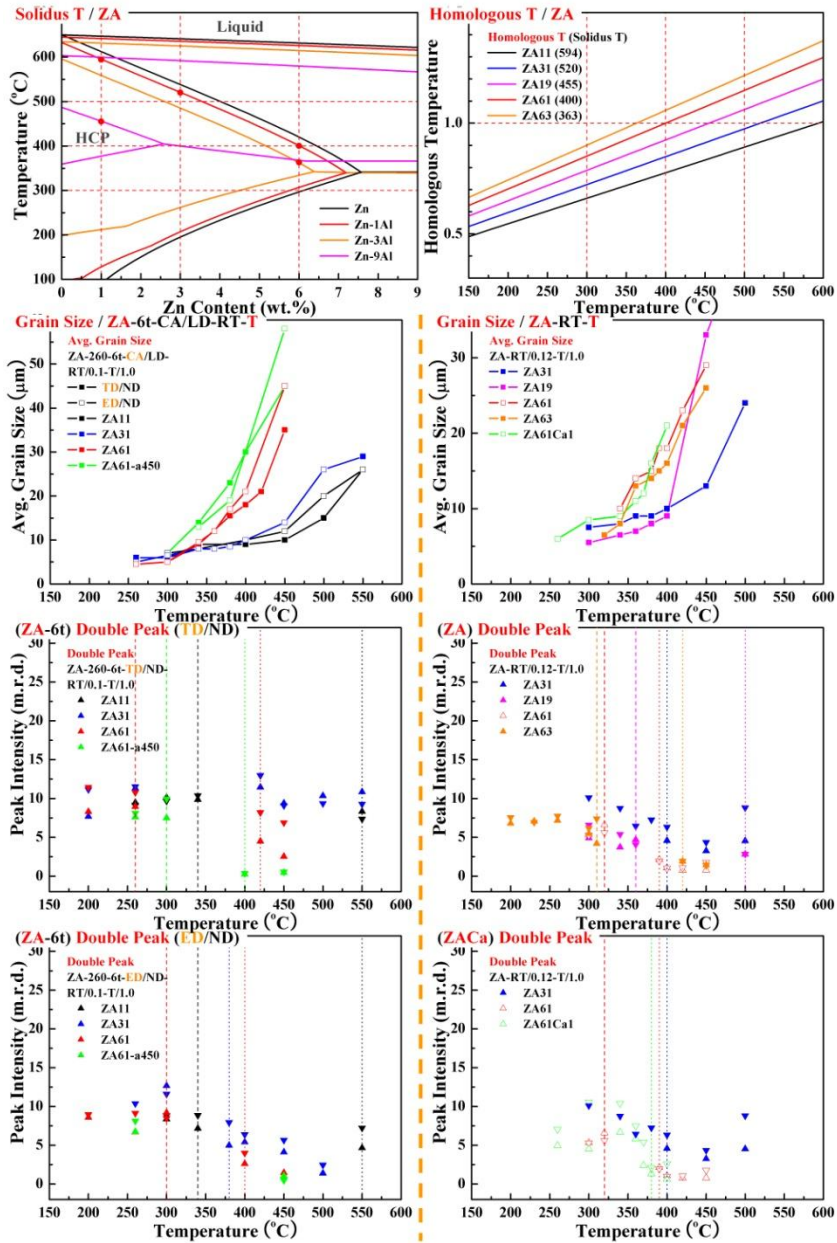


Figure 4.27 Summary; analysis on grain size and critical temperatures ($T_{DP, low}$ and $T_{DP, high}$) based on solidus temperature.

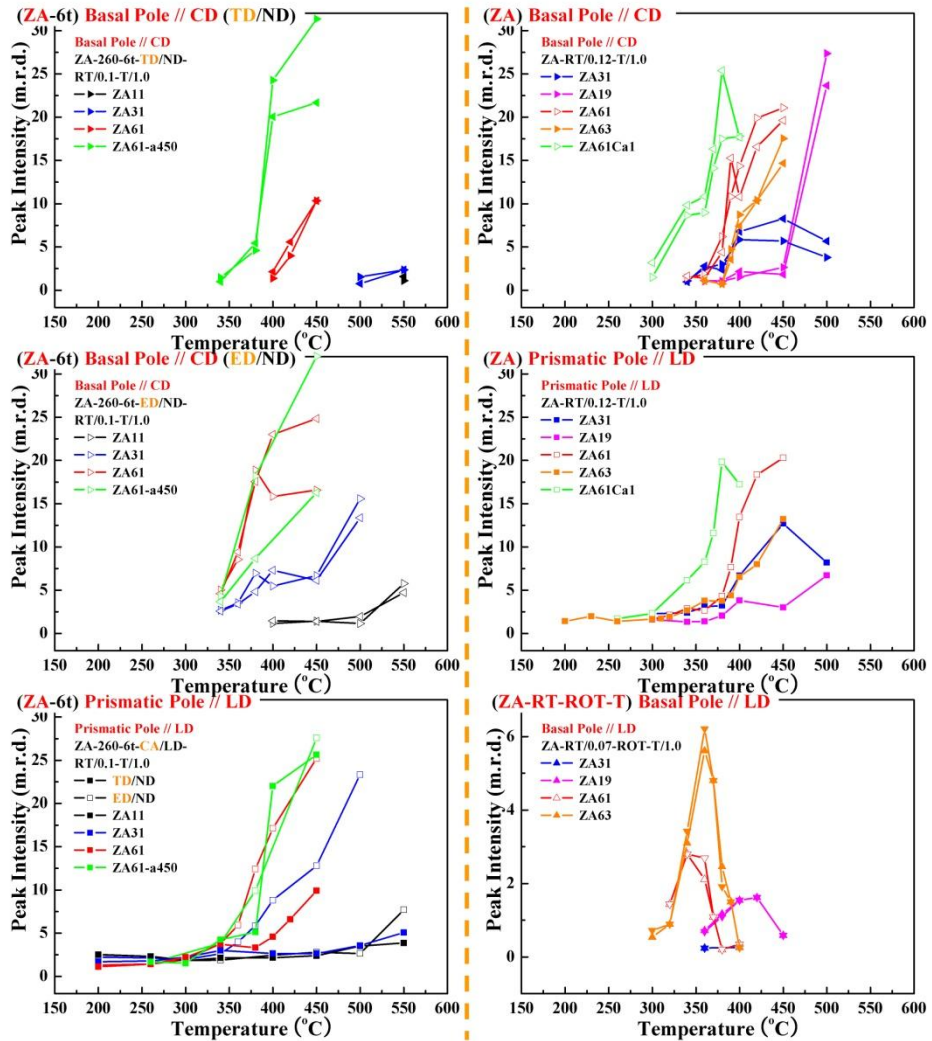


Figure 4.28 Summary; analysis on intensity of CD and LD Textures based on (1) solidus temperature and (2) grain size.

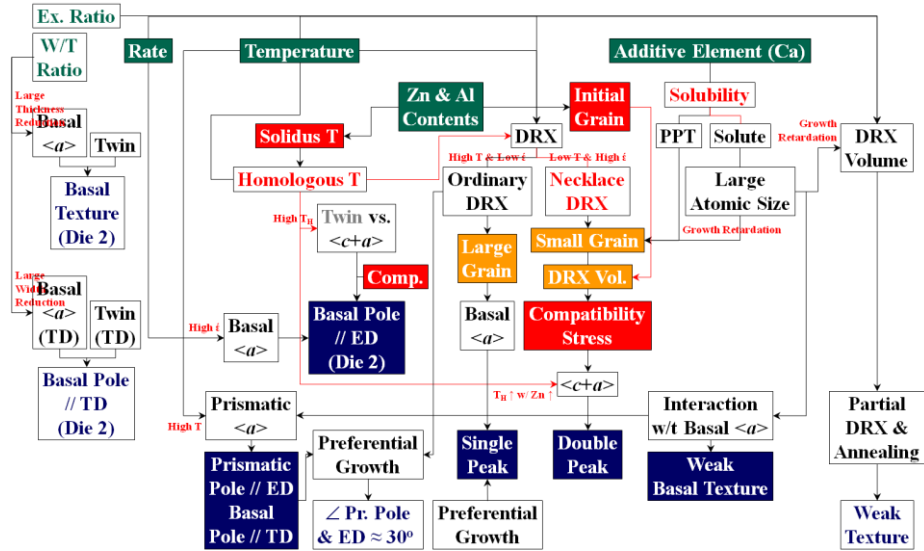


Figure 4.29 Summary; flow chart for texture development.

Chapter 5 Conclusions

In this study, effects of the extrusion temperature and alloying elements on the textures of the extruded Mg-Zn-Al alloys were investigated. And their mechanisms were systematically studied by the two-step PSC tests. Conclusions are represented as follows;

1. With increase in Zn and Al contents, spread of the basal poles toward the ED (ED spread) and tilt angle corresponding to the peak in the DP texture increased with decrease in grain size. And addition of Zn was more effective to increase the ED spread and decrease the grain size than addition of Al.

2. With increase in extrusion temperature, SP texture was developed and ED spread decreased. In the ZA11 alloys, $\{10\cdot10\}\langle 1\cdot210\rangle$ texture strengthened with increase in temperature. However, in the ZA61 and ZA63 alloys, $\langle 0001\rangle//ED$ texture was developed at high temperature and strengthened with increase in temperature. And the intensity of ED texture increased with increase in Al content.

3. With addition of Ca or Ce on pure Mg, intensity of the DP texture weakened and ED spread and tilt angle corresponding to the peak in the DP texture increased. And with addition of Ca on ZA alloys, DP texture with weak intensity was developed and $\{11\cdot20\}\langle 1\cdot100\rangle$ texture was developed. With increase in Ca content in Z6 or ZA61 alloys, intensity of the TD texture increased instead of decrease in intensity of the DP texture.

4. In the two-step PSC, DP texture was developed with the partially DRXed fine microstructure developed by the NRX at low temperature. DP texture was sustained until the partially DRXed fine microstructure was sustained. And SP texture was developed with the fully DRXed coarse microstructure by the NRX and grain growth at mid temperature. At high temperature, DP + CD texture (DP and $\{11-20\}\langle 1-100\rangle$ texture) was developed with large grains occurred by ordinary DRX.

5. In the two-step PSC, with increase in Zn content, LD spread and tilt angle corresponding to the peak in DP texture developed at low and high temperature increased. And with increase in Zn content, intensity of the CD texture increased.

6. In the two-step PSC, with decrease in initial grain size, LD spread and tilt angle corresponding to the peak in DP texture increased with increase in fraction of the small DRXed grain region.

7. Effect of increase in strain rate on the texture was similar to the effect of decrease in temperature because flow stress increased and grain size decreased with increase in strain rate, similarly. However, besides large flow stress, it was necessary to sustain the grain size small to develop DP texture.

8. In the one-step PSC (0.4000/sec) of the ZA63 alloy, LD texture occurred and intensity of the LD texture increased with increase in temperature and it was maximized at 380°C. In the one-step PSC (0.4000/sec) a of the ZA alloys at 400°C, intensity of the LD texture increased with decrease in solidus

temperature (363°C for the ZA63, 400°C for the ZA61 and 455°C for the ZA19 alloy).

9. In the two-step PSC (ROT) of the ZA63 alloy, intensity of the LD texture increased with increase temperature and it was maximized at 360°C. In the two-step PSC (ROT) of the ZA alloys, intensity of the LD texture increased with decrease in solidus temperature (363°C for the ZA63, 400°C for the ZA61 and 455°C for the ZA19 alloy).

10. In the two-step PSC, with addition of Ca in the ZA61 alloy, T_{CD} decreased at about 40°C but maximum intensity of the CD texture was similar with that of ZA61 alloy. Addition of Ca promoted the development of the CD textures by increasing activity of the prismatic $\langle a \rangle$ slip. It might be related to the strong interaction of the Ca element with the initially-generated basal $\langle a \rangle$ dislocations originated from its large atomic size.

11. Change in texture with temperature can be explained from the viewpoint of the grain-size dependant compatibility deformation. Because small grains are more favorable to deform by the pyramidal II $\langle c+a \rangle$ slip which has much higher CRSS value by aid of the compatibility stress, DP texture which can be developed by activation of the pyramidal II $\langle c+a \rangle$ slip can be developed at low temperature where the grain size is small enough. With increase in temperature, grain size increases. Therefore, SP texture is developed because only the basal slip which has low CRSS value can be activated inside the grain. And at higher temperature, CRSS of the pyramidal II $\langle c+a \rangle$ slip becomes close to the CRSS of the basal slip. Therefore, DP texture can be developed by activation of the pyramidal II $\langle c+a \rangle$ slip.

12. In order to increase the LD spread and tilt angle corresponding to the peak in DP texture at low temperature, it seems important to increase the fraction of small DRXed grain region and restrict their growth by decreasing the initial grain size, solidus temperature and PSC temperature.

13. Change in texture with Zn and Al contents can be explained from the viewpoint of the thermal activation of the cross-slip. With increase in Zn and Al content, solidus temperature decreases and inversely, homologous temperature increases. With increase in homologous temperature, activity of the non-basal slip like prismatic $\langle a \rangle$ and pyramidal II $\langle c+a \rangle$ slip can be enhanced by aid of the increased thermal stress. Therefore, stronger CD texture, ED (LD) texture and wider DP texture can be developed with increase in Zn and Al contents.

Bibliography

- [1] J. W. Choi and K. S. Shin, "Development of High Performance Magnesium Alloys via Microstructure and Texture Control", *Mater. Sci. Forum*, 618-619 (2009), pp. 249-252.
- [2] J. W. Choi, J. H. Hwang and K. S. Shin, "Effects of Alloying Element on Texture and Mechanical Properties of Extruded Mg-Zn-Al Alloys", *Magnesium Technology 2009* (2009), pp. 411-414.
- [3] S. R. Agnew, M. H. Yoo and C. N. Tome, "Application of Texture Simulation to Understanding Mechanical Behavior of Mg and Solis Solution Alloys Containing Li or Y", *Acta Mater.*, 49 (2001), pp. 4277-4289.
- [4] A. Styczynski, Ch. Hartig, J. Bohlen and D. Letzig, "Cold Rolling Textures in AZ31 Wrought Magnesium Alloy", *Scripta Mater.*, 50 (2004) pp. 943-947.
- [5] T. Walde and H. Riedel, "Modeling Texture Evolution during Hot Rolling of Magnesium Alloy AZ31", *Mater. Sci. Eng. A*, 443 (2007), pp. 277-284.
- [6] G. Gottstein and T. Al-Samman, "Texture Development in Pure Mg and Mg Alloy AZ31", *Mater. Sci. Forum*, 495-497 (2005), pp. 623-632.
- [7] T. Al-Samman and G. Gottstein, "Deformation Conditions and Stability of the Basal Texture in Magnesium", *Mater. Sci. Forum*, 539-543 (2007), pp. 3401-3406.
- [8] C. Bettles and M. Barnett, "Advances in Wrought Magnesium Alloys: Fundamentals of Processing, Properties and Applications", Woodhead Publishing, (2012), pp. 187-207.
- [9] A. Imandoust, C. D. Barrett, T. Al-Samman, K. A. Inal and H. El Kadiri, "A Review on the Effect of Rare-earth Elements on Texture Evolution

- during Processing of Magnesium Alloys”, *J. Mater. Sci.*, 52 (2017), pp. 1-29.
- [10] O. Sitdikov and R. Kaibyshev, “Dynamic Recrystallization in Pure Magnesium”, *Mater. T. JIM*, 42 (2001), pp. 1928-1937.
- [11] D. G. J. Griffiths, “Understanding Texture Weakening in Magnesium Rare Earth Alloys”, Ph. D Thesis (2014), pp. 42-67.
- [12] Y. B. Chun, J. Geng, N. Stanford, C. H. J. Davies, J. F. Nie and M. R. Barnett, “Processing and Properties of Mg-6Gd-1Zn-0.6Zr: Part 1 - Recrystallization and Texture Development”, *Mater. Sci. Eng. A*, 528 (2011), pp. 3653-3658.
- [13] R. Cottam, J. Robson, G. Lorimer and B. Davis, “Dynamic Recrystallization of Mg and Mg-Y Alloys: Crystallographic Texture Development”, *Mater. Sci. Eng. A*, 485 (2008), pp. 375-382.
- [14] N. Stanford, “ The Effect of Rare Earth Elements on the Behaviour of Magnesium-based Alloys: Part 2 -Recrystallisation and Texture Development”, *Mater. Sci. Eng. A*, 565 (2013), pp. 469-475.
- [15] N. Stanford, M. D. Callaghan and B. de Jong, “ The Effect of Rare Earth Elements on the Behaviour of Magnesium-based Alloys: Part 1 - Hot Deformation Behaviour”, *Mater. Sci. Eng. A*, 565 (2013), pp. 459-468.
- [16] L. W. F. Mackenzie and M. Pekguleryuz, “ The Influence of Alloying Additions and Processing Parameters on the Rolling Microstructures and Textures of Magnesium Alloys”, *Mater. Sci. Eng. A*, 480 (2008), pp. 189-197.
- [17] S. B. Yi, H. G. Brokmeier and D. Letzig, “Microstructural Evolution during the Annealing of an Extruded AZ31 Magnesium Alloy”, *J. Alloy. Compd.*, 506 (2010), pp. 364-371.

- [18] J. Bohlen, S. B. Yi, J. Swiostek, D. Letzig, H. G. Brokmeier and K. U. Kainer, "Microstructure and Texture Development during Hydrostatic Extrusion of Magnesium Alloy AZ31", *Scripta Mater.*, 53 (2005), pp. 259-264.
- [19] M. A. Steiner, J. J. Bhattacharyya and S. R. Agnew, "The Origin of Enhancement of $\{0001\}\langle 11\text{-}20\rangle$ Texture during Heat Treatment of Rolled AZ31B Magnesium Alloys", *Acta Mater.*, 95 (2015), pp. 443-455.
- [20] J. J. Bhattacharyya, S. R. Agnew and G. Muralidharan, "Texture Enhancement during Grain Growth of Magnesium Alloy AZ31B", *Acta Mater.*, 86 (2015), pp. 80-94.
- [21] K. Y. Zhu, D. Chaubet, B. Bacroix and F. Brisset, "A Study of Recovery and Primary Recrystallization Mechanisms in a Zr-2Hf Alloy", *Acta Mater.*, 53 (2005), pp. 5131-5140.
- [22] S. E. Ion, F. J. Humphreys and S. H. White, "Dynamic Recrystallisation and the Development of Microstructure during the High Temperature Deformation of Magnesium", *Acta Metall.*, 30 (1982), pp. 1909-1919 (1982).
- [23] I. Basu and T. Al-Samman, "Triggering Rare Earth Texture Modification in Magnesium Alloys by Addition of Zinc and Zirconium", *Acta Mater.*, 67 (2014), pp. 116-133.
- [24] I. Basu, T. Al-Samman and G. Gottstein, "Shear Band-related Recrystallization and Grain Growth in Two Rolled Magnesium-Rare Earth Alloys", *Mater. Sci. Eng. A*, 579 (2013), pp. 50-56.
- [25] L. W. F. Mackenzie and M. Pekguleryuz, "The Recrystallization and Texture of Magnesium-Zinc-Cerium Alloys", *Scripta Mater.*, 59 (2008), pp. 665-668.
- [26] J. Bohlen, J. Wendt, M. Nienaber, K. U. Kainer, L. Stutz and D. Letzig,

- “Calcium and Zirconium as Texture Modifiers during Rolling and Annealing of Magnesium-Zinc Alloys”, *Mater. Charact.*, 101 (2015), pp. 144-152.
- [27] X. Huang, K. Suzuki, Y. Chino and M. Mabuchi, “Texture and Stretch Formability of AZ61 and AM60 Magnesium Alloy Sheets Processed by High-temperature Rolling”, *J. Alloy. Compd.*, 632 (2015), pp. 94-102.
- [28] X. Huang, K. Suzuki, Y. Chino and M. Mabuchi, “Improvement of Stretch Formability of Mg-3Al-1Zn Alloy Sheet by High Temperature Rolling at Finishing Pass”, *J. Alloy. Compd.*, 509 (2011), pp. 7579-7584.
- [29] J. Su, A. S. H. Kabir, M. Sanjari and S. Yue, “Correlation of Static Recrystallization and Texture Weakening of AZ31 Magnesium Alloy Sheets Subjected to High Speed Rolling”, *Mater. Sci. Eng. A*, 674 (2016), pp. 343-360.
- [30] J. Su, M. Sanjari, A. S. H. Kabir, J. J. Jonas and S. Yue, “Static Recrystallization Behavior of Magnesium AZ31 Alloy Subjected to High Speed Rolling”, *Mater. Sci. Eng. A*, 662 (2016), pp. 412-425.
- [31] J. Su, M. Sanjari, A. S. H. Kabir, I. H. Jung, J. J. Jonas, S. Yue and H. Utsunomiya, “Characteristics of Magnesium AZ31 Alloys Subjected to High Speed Rolling”, *Mater. Sci. Eng. A*, 636 (2015), pp. 582-592.
- [32] C. Bettles and M. Barnett, “Advances in Wrought Magnesium Alloys: Fundamentals of Processing, Properties and Applications”, Woodhead Publishing, (2012), pp. 78-83.
- [33] J. Geng, M. F. Chisholm, R. K. Mishra and K. S. Kumar, “An Electron Microscopy Study of Dislocation Structures in Mg Single Crystals Compressed along [0001] at Room Temperature”, *Phil. Mag.*, 95 (2015), pp. 3910-3932.

- [34] J. Geng, M. F. Chisholm, R. K. Mishra and K. S. Kumar, “The Structure of $\langle c+a \rangle$ type Dislocation Loops in Magnesium”, *Phil. Mag. Lett.*, 94 (2014), pp. 377-386.
- [35] T. Obara, H. Yoshinga and S. Morozumi, “ $\{11\bar{2}3\}\langle 1\bar{1}23 \rangle$ Slip System in Magnesium”, *Acta Metall.*, 21 (1973), pp. 845-853.
- [36] S. Ando, N. Harada, M. Tsushida, H. Kitahara and H. Tonda, “Temperature Dependence of Deformation Behavior” *Key Eng. Mater.*, 345-346 (2007), pp. 101-104.
- [37] S. Ando and H. Tonda, “Non-basal Slip in Magnesium-Lithium Alloy Single Crystals”, *Mater. Trans. JIM*, 41 (2000), pp. 1188-1191.
- [38] S. R. Agnew and O. Duygulu, “Plastic Anisotropy and the Role of Non-basal Slip in Magnesium Alloy AZ31B”, *Int. J. Plast.*, 21 (2005), pp. 1161-1193.
- [39] S. R. Agnew and O. Duygulu, “TEM Investigation of Dislocation Mechanism in Mg Alloy AZ31B Sheet”, *Magnesium Technology 2004*, TMS 2004, pp. 61-65.
- [40] A. Y. Kochubey, V. N. Serebryany and V. N. Timofeev, “TEM Investigation of Dislocations in Hot Deformed Mg-Al-Zn Alloy”, *Mater. Sci. Forum*, 550 (2007), pp. 259-264.
- [41] V. N. Timofeev, V. N. Serebryany and Y. A. Zaliznyak, “Electron-Microscopic Study of the Slip Systems in an Mg-4.5%Al-1%Zn Alloy”, *Russian Metall.*, 2008 (2008), pp. 266-269.
- [42] F. Kang, J. Q. Liu, J. T. Wang and X. Zhao, “The Effect of Hydrostatic Pressure on the Activation of Non-basal Slip in a Magnesium Alloy”, *Scripta Mater.*, 61 (2009), pp. 844-847.
- [43] F. Kang, Z. Li, J. T. Wang, P. Cheng and H. Y. Wu, “The Activation of $\langle c+a \rangle$ Non-basal Slip in Magnesium Alloys”, *J. Mater. Sci.*, 47 (2012),

- pp. 7854-7859.
- [44] S. R. Agnew, J. A. Horton and M. H. Yoo, "Transmission Electron Microscopy Investigation of $\langle c+a \rangle$ Dislocations in Mg and α -Solid Solution Mg-Li Alloys", *Metall. Mater. Trans. A*, 33A (2002), pp. 851-858.
- [45] S. Sandlobes, M. Friak, J. Neugebauer and D. Raabe, "Basal and Non-basal Dislocation Slip in Mg-Y", *Mater. Sci. Eng. A*, 576 (2013), pp. 61-68.
- [46] S. Sandlobes, Z. Pei, M. Friak, L. F. Zhu, F. Wang, S. Zaefferer, D. Raabe and J. Neugebauer, "Ductility Improvement of Mg Alloys by Solid Solution: Ab Initio Modeling, Synthesis and Mechanical Properties", *Acta Mater.*, 70 (2014), pp. 92-104.
- [47] A. Moitra, S. G. Kim and M. F. Horstemeyer, "Solute Effect on the $\langle c+a \rangle$ Dislocation Nucleation Mechanism in Magnesium", *Acta Mater.*, 75 (2014), pp. 106-112.
- [48] R.E. Reed-Hill and R. Abbaschian, "Physical Metallurgy Principles", PWS (Boston), third edition (1994), pp. 849-851, 857-859.
- [49] M. H. Yoo, S. R. Agnew, J. R. Morris and K. M. Ho, "Non-basal Slip Systems in HCP Metals and Alloys: Source Mechanisms", *Mater. Sci. Eng. A*, 319-321 (2001), pp. 87-92.
- [50] M. Z. Byun, "Plastic Deformation Behavior of Magnesium Single Crystals", Ph. D Thesis (2013), pp. 64.
- [51] M. H. Yoo, J. R. Morris, K. M. Ho and S. R. Agnew, "Nonbasal Deformation Modes of HCP Metals and Alloys: Role of Dislocation Source and Mobility", *Metall. Mater. Trans. A*, 33A (2002), pp. 813-822.
- [52] J. A. Yasi, L. G. Hector Jr. and D. R. Trinkle, "First-principles Data for Solid-solution Strengthening of Magnesium: From Geometry and Chemistry to Properties", *Acta Mater.*, 58 (2010), pp. 5704-5713.

- [53] J. A. Yasi, L. G. Hector Jr. and D. R. Trinkle, "Prediction of Thermal Cross-slip Stress in Magnesium Alloys from a Geometric Interaction Model", *Acta Mater.*, 60 (2012), pp. 2350-2358.
- [54] K. H. Kim, J. B. Jeon, N. J. Kim and B. J. Lee, "Role of Yttrium in Activation of $\langle c+a \rangle$ Slip in Magnesium: An Atomistic Approach", *Scripta Mater.*, 108 (2015), pp. 104-408.
- [55] A. Akhtar and E. Teghtsoonian, "Substitutional Solution Hardening of Magnesium Single Crystals", *Phil. Mag.*, 25 (1972), pp. 897-916.
- [56] B. Raeisinia, S. R. Agnew and A. Aktar, "Incorporation of Solid Solution Alloying Effects into Polycrystal Modeling of Mg Alloys", *Metall. Mater. Trans. A*, 42A (2011), pp. 1418-1430.
- [57] N. Stanford and M. R. Barnett, "Solute Strengthening of Prismatic Slip, Basal Slip and $\{10\text{-}12\}$ twinning in Mg and Mg-Zn binary alloys", *Int. J. Plasticity*, 47 (2013), pp. 165-181.
- [58] J. Koike, T. Kobayashi, T. Mukai, H. Watanabe, M. Suzuki, K. Maruyama, and K. Higashi, "The Activity of Non-basal Slip Systems and Dynamic Recovery at Room Temperature in Fine-grained AZ31B Magnesium Alloys", *Acta Mater.*, 51 (2003), pp. 2055-2065.
- [59] M. F. Ashby, "The Deformation of Plastically Non-homogeneous Materials", *Phil. Mag.*, 21 (1970), pp. 399-424.
- [60] J. Koike, "Dislocation Plasticity and Complementary Deformation Mechanisms in Polycrystalline Mg Alloys", *Mater. Sci. Forum*, 449-452 (2004), pp. 665-668.
- [61] C. S. Lee and H. Margolin, "Deformation of a Burgers Oriented Bimetallic Bicrystal of Alpha-Beta (Ti-13Mn)", *Metall. Trans. A*, 17 (1986), pp. 451-460.
- [62] M. A. Meyers, "A Model for the Effect of Grain Size on the Yield Stress

- of Metals”, *Phil. Mag.*, 46 (1982), pp. 737-759.
- [63] M. Jafari and A. Najafizadeh, “Correlation between Zener–Hollomon Parameter and Necklace DRX during Hot Deformation of 316 Stainless Steel”, *Mater. Sci. Eng. A*, 501 (2009), pp. 16-25.
- [64] D. Ponge and G. Gottstein, “Necklace Formation during Dynamic Recrystallization: Mechanisms and Impact on Flow Behavior”, *Acta Mater.*, 46 (1998), pp. 69-80.
- [65] A. G. Beer and M. R. Barnett, “Microstructural Development during Hot Working of Mg-3Al-1Zn”, *Metall. & Mater. Trans. A*, 38A (2007), pp. 1856-1867.
- [66] J. W. Senn and S. R. Agnew, “Texture Randomization of Magnesium Alloys Containing Rare Earth Elements”, *Magnesium Technology 2008*, (2008), pp. 153-158.
- [67] S. Sandlobes, S. Zaefferer, I. Schestakow, S. Yi and R. Gonzalez-Martinez, “On the Role of Non-basal Deformation Mechanisms for the Ductility of Mg and Mg-Y alloys”, *Acta Mater.*, 59 (2011), pp. 429-439.
- [68] S. Sandlobes, I. Schestakow, S. Yi, S. Zaefferer, J. Chen, M. Friak, J. Neugebauer and D. Raabe, “The Relation between Shear Banding, Microstructure and Mechanical Properties in Mg and Mg-Y Alloys”, *Mater. Sci. Forum*, 690 (2011), pp. 202-205.
- [69] S. Sandlobes, M. Friak, S. Zaefferer, A. Dick, S. Yi, D. Letzig, Z. Pei, L. F. Zhu, J. Neugebauer and D. Raabe, “The relation between Ductility and Stacking Fault Energies in Mg and Mg-Y alloys”, *Acta Mater.*, 60 (2012), pp. 3011-3021.

초 록

전 세계적인 유가 상승 및 CO₂ 배출 규제로 인해 수송기기의 연비향상에 대한 요구가 증가함에 따라 수송기기의 무게를 줄이기 위한 연구가 활발히 진행되고 있다. 마그네슘의 높은 비강도와 좋은 주조성에 착안하여, 휠, 하우징, 커버와 같은 자동차 부품에 마그네슘 합금 주조재를 활발히 적용해 왔다. 이러한 주조재 부품 개발 연구뿐만 아니라 경량화 효과를 높이기 위하여 차체의 소재로 마그네슘 합금 가공재를 사용하고자 하는 연구가 활발히 진행되고 있다. 이러한 마그네슘 합금 가공재를 수송기기의 부품 및 차체의 소재로 사용하기 위해서는 현재까지 개발된 마그네슘합금의 부족한 성형성을 향상시킬 필요가 있다. 마그네슘 합금 가공재의 성형성이 부족한 이유는 가공재를 제조하는 압출 및 압연 과정에서 저면이 압연면 또는 압출면과 평행한 저면 집합조직이 강하게 발달하기 때문으로 이는 마그네슘 합금의 주요 변형기구가 저면 슬립과 인장쌍정으로 제한되어 있기 때문이다. 이러한 저면 집합조직을 약화시키기 위하여 합금원소 첨가를 통해 비저면 슬립계를 활성화시키기 위한 연구가 활발히 진행되고 있다. 특히, Ce, Gd, Nd, Y과 같은 희토류 원소를 순수 마그네슘에 미량 첨가할 경우 저면 집합조직이 약화되며, 이로 인해 성형성이 향상되는 것으로 보고되고 있다. 다만 이러한 희토류 원소만 순수 마그네슘에 첨가할 경우 수송기기 부품 소재로 사용하기 위한 강도 요구조건을 충족시키지 못하기 때문에 Zn와 Al을 첨가하여 강도를 높이면서도 저면 집합

조직을 약화시키고자 하는 연구가 진행되고 있다. 이러한 연구를 진행하기 위해서는 우선 Zn와 Al이 집합조직에 미치는 영향에 대한 체계적인 연구가 선행되어야 한다. 본 연구에서는 이러한 연구 일환으로써 Zn와 Al 함량, Ca 첨가, 온도가 Mg-Zn-Al 합금 압출판재의 집합조직에 미치는 영향을 조사하였다. 그리고 Mg-Zn-Al 합금의 2단계 평면변형압축시험을 통해서 집합조직 발달기구를 체계적으로 연구하였다.

Zn와 Al의 함량이 증가함에 따라 basal pole의 압출방향으로의 분포와 double peak basal 집합조직의 basal pole의 peak에 해당하는 기울기 각이 증가하였으며, 결정립 크기의 감소를 동반하였다. 압출 온도가 증가함에 따라 single peak basal 집합조직이 발달하였으며, basal pole의 압출방향(ED)으로의 분포가 감소하였다. ZA11 합금의 경우, 온도가 증가함에 따라 $\{10\cdot10\}\langle 1\cdot210\rangle$ 집합조직이 발달하였다. 반면에 ZA61과 ZA63 합금의 경우에는 고온에서 $\langle 0001\rangle//ED$ 집합조직이 발생하였으며, 온도가 증가함에 따라 강화되었다. 또한 Al의 함량이 증가함에 따라 $\langle 0001\rangle//ED$ 집합조직이 강화되었다. Ca을 순수 마그네슘에 첨가함에 따라 double peak basal 집합조직의 전반적인 세기가 약화되었으며, basal pole의 압출방향으로의 분포가 증가하였다. Ca을 ZA 합금에 첨가함에 따라 double peak basal 집합조직의 전반적인 세기가 약화되었으며, 대신에 $\{11\cdot20\}\langle 1\cdot100\rangle$ 집합조직이 발달하였다. Ca의 첨가량이 증가함에 따라 double peak basal 집합조직은 약화되고, $\{11\cdot20\}\langle 1\cdot100\rangle$ 집합조직은 강화되었다.

보다 체계적으로 ZA합금 집합조직의 변화를 관찰하기 2단계 평면변형압축시험(상온에서의 평면변형압축 후 고온에서의 평면변형압

축)을 수행하였다. 상대적으로 저온에서는 부분적으로 동적 재결정(DRX)이 진행된 미세한 미세조직과 함께 double peak basal 집합조직이 발달하였다. 온도가 증가함에 따라 동적 재결정이 완전히 진행된 조대한 미세조직과 함께 single peak basal 집합조직이 발달하였다. 보다 높은 고온에서는 다시 double peak basal 집합조직이 발달하였으며, {11-20}<1-100> 집합조직이 함께 발달하였다. Zn의 함량이 증가함에 따라 basal pole의 길이방향(LD)으로의 분포와 double peak basal 집합조직의 basal pole의 peak에 해당하는 기울기 각이 증가하였다. ZA63 합금 주조재의 상대적으로 빠른 속도 (0.4000/초)에서의 1단계 평면변형압축에서는 <0001>//LD 집합조직이 발생하였으며, 온도가 증가함에 따라 강화되다가 일정 온도 이상에서는 다시 약화되었다. Zn나 Al의 함량이 증가하여 고용 온도가 감소함에 따라 <0001>//LD 집합조직의 세기가 증가하였다. <0001>//LD 집합조직의 변화를 체계적으로 관찰하기 위하여 수행한 2단계 평면변형압축시험(상온에서의 평면변형압축 후 시편을 너비방향을 축으로 90° 회전시켜서 장축 후 고온에서의 평면변형압축)에서도 고용 온도가 감소함에 따라 <0001>//LD 집합조직의 세기가 증가하였다.

이러한 현상들을 온도와 Zn 및 Al 첨가량에 따른 결정립 크기와 고용 온도의 변화의 측면에서 결정립 크기에 따른 적합성 변형 및 교차 슬립의 열적 활성화 이론에 기반하여 설명하였다.

주요어: 마그네슘 합금, 집합조직, 압출재, 평면변형압축, 온도, 아연, 알루미늄, 칼슘

학번: 2005-23420